3-2005

Performance of a Spectrally Encoded Multi-carrier Phase Shift Keying Communications System in a Frequency-Selective, Slowly-Fading Multipath Channel

Charles M. Gaona

Performance of a Spectrally Encoded Multi-Carrier Phase Shift Keying Communication System in a Frequency-Selective, Slowly-Fading Multipath Channel

THESIS

Charles M. Gaona, Major, USAF

AFIT/GE/ENG/05-03

DEPARTMENT OF THE AIR FORCE
AIR UNIVERSITY

AIR FORCE INSTITUTE OF TECHNOLOGY

Wright-Patterson Air Force Base, Ohio

The views expressed in this thesis are those of the author and do not reflect the official policy or position of the United States Air Force, Department of Defense, or the United States Government.

AFIT/GE/ENG/05-03

Performance of a Spectrally Encoded Multi-Carrier Phase Shift Keying Communication System in a Frequency-Selective, Slowly-Fading Multipath Channel

THESIS

Presented to the Faculty

Department of Electrical and Computer Engineering

Graduate School of Engineering and Management

Air Force Institute of Technology

Air University

Air Education and Training Command

In Partial Fulfillment of the Requirements for the

Degree of Master of Science in Electrical Engineering

Charles M. Gaona, BS

Major, USAF

March 2005

AFIT/GE/ENG/05-03

Performance of a Spectrally Encoded Multi-Carrier Phase Shift Keying Communication System in a Frequency-Selective, Slowly-Fading Multipath Channel

Charles M. Gaona, BS
Major, USAF

Approved:

/signed/	21 Mar 2005
Robert F. Mills (Chairman)	date
/signed/	21 Mar 2005
Michael A. Temple (Member)	date
/signed/	21 Mar 2005
Todd B. Hale, Major, USAF (Member)	date

AFIT/GE/ENG/05-03

Abstract

This research examines the performance of a spectrally encoded, multi-carrier, phase shift keying communications system in a frequency-selective, slowly-fading multipath channel. The specific communications system modeled is the transform domain communication system (TDCS) originally researched as an interference avoidance technique. Previous TDCS research assumed an additive white Gaussian noise channel, which is not representative of a realistic environment.

This thesis presents overviews of previous TDCS research, the multipath fading channel, and the RAKE receiver. Analysis and `Matlab`® simulations compare the performance of spectrally encoded and un-encoded signals through a multipath fading channel using an L-diversity TDCS RAKE receiver. Encoded signals take on the spectral shape of the multipath fading channel transfer function. Un-encoded signals have a flat magnitude spectrum. The research also evaluates the interference rejection capability of spectrally encoded signals in a multipath channel.

Research results indicate for diversities (L) ranging between 2 and 50, spectrally encoded signals need 1.0 to 2.75dB less transmitted normalized bit energy to noise power spectral density ratios (E_b/N_o) to achieve the same probability of bit error (P_b) as un-encoded signals. Results also demonstrate that spectrally encoded TDCS signals retain the original interference rejection capability.

Acknowledgements

All thanks, praise, honor and glory to the LORD God Almighty, the giver of every good and perfect gift, clothed in majesty and righteousness. In His steadfast love and compassion, God has called and reconciled His people through the sacrifice of His only Son, Jesus Christ. To Him and Him alone I owe an eternal debt of gratitude for His powerful saving grace and the fullness of joy He brings in this life and Eternity. In Christ "are hidden all the treasures of wisdom and knowledge," therefore if God has been pleased to open my eyes to whatever good that may have been discovered in this research, I give thanks to Him.

To my wife, I thank you for your love, encouragement and support. You are my crown and in you I rejoice. I am grateful that the LORD has provided such a wonderful woman as my completer. To my children, your smiles and laughter at the end of the day bring me great joy. Thank you for your patience as your daddy completed this work. To my brothers in the zoo and in the LORD, thank you for your encouragement and exhortation to seek first the Kingdom of God.

Finally, thank you to my advisor Dr Robert Mills for your patient guidance and direction. To my committee Dr Mike Temple and Major Todd Hale, thank you for asking the hard questions and opening my eyes to my blind spots. To my AFRL/SNRW sponsor, Mr Jim Stephens, thank you for supporting this research.

Charles M. Gaona

Table of Contents

Page

Page

Page

List of Figures

List of Tables

List of Symbols

Symbol		Page
f_c	Center frequency	18
T_{samp}	Sampling interval	19
f_{samp}	Sampling frequency	19
τ_n	The n^{th} delay in the multipath channel	19
h_l	Channel impulse response	20
H_l	Channel transfer function	20
H_m	Magnitude of m^{th} component of channel transfer function	20
E_b/N_o	normalized bit energy to noise power spectral density ratio referenced to transmitted E_b	23
γ_b	energy per bit to noise power spectral density ratio in the demodulator	24
$r_{l,k}(t)$	Received signal, complex low-pass equivalent, k^{th} symbol	26
Z_m	Demodulator test statistic for i^{th} symbol	26
$s_{l,k}(t)$	Transmitted signal, complex low-pass equivalent, k^{th} symbol	28
J/S	Interferer power to signal power ratio	60
z_t	The t^{th}-quantile of the standard normal distribution	80
R^2	Coefficient of determination	127

List of Abbreviations

Abbreviation		Page
GIG	Global Information Grid	1
TDCS	transform domain communication system	3
PR	pseudo-random	3
CSK	cyclic shift keying	3
MPSK	M-ary phase shift keying	3
FSSF	frequency-selective, slowly-fading	3
BPSK	binary phase shift keying	4
RF	radio frequency	4
SNR	signal-to-noise ratio	4
AWGN	additive white Gaussian noise	5
PSD	power spectral density	5
FSW	fundamental signaling waveforms	6
IDFT	Inverse Discrete Fourier Transform	7
LOS	Line-of-Sight	14
RMS	root mean square	17
DFT	Discrete Fourier Transform	20
SNR	signal-to-noise ratio	23
DOF	degrees-of-freedom	24
pdf	probability density function	24
i.i.d.	independent, identically distributed	29
dB	Decibel	66
DSSS	Direct sequence spread spectrum	105
FHSS	Frequency hopped spread spectrum	105
CDF	cumulative distribution function	126

Performance of a Spectrally Encoded Multi-Carrier Phase Shift Keying Communication System in a Frequency-Selective, Slowly-Fading Multipath Channel

I. Introduction

1.1 Background

As early as the 5^{th} century B.C., Sun Tzu extolled the principle of knowing the enemy in combat in the following proverb:

> If you know the enemy and know yourself, you need not fear the result of a hundred battles. If you know yourself but not the enemy, for every victory gained you will also suffer a defeat. If you know neither the enemy nor yourself, you will succumb in every battle [2].

While the application has changed after 2,500 years of history, this principle still holds true. Today's warrior desires an integrated picture of the battlespace to 1) reveal the enemy's every move and intention, and 2) understand the status and capabilities of friendly forces. The fundamental assumption behind the existence of this integrated picture is the ubiquitous network. A global network that connects air, space, land and sea assets around the world is the foundation required to deliver actionable information to the commander on the battlefield.

The need for a pervasive network is expressed clearly in the vision documents for all of the United States armed services. In the US Army, it is known as LandWarNet. It is the Navy and Marine Corps FORCEnet. It is encompassed in the Air Force's core competency of Information Superiority. The worldwide defense network is evolving toward the vision of the Global Information Grid (GIG) which consists primarily of fiber, wire, and satellite communications. However, near the forward edge of the battle area, at the edge of the network, the electronic lifeline from the troops to the GIG travels over wireless communications systems. This lifeline brings situational

awareness, command and control and intelligence information to commanders at the very tip of the spear.

The wireless communications system is often called upon to provide connections in the harshest of environments. In addition to the natural communications barriers of weather, atmospheric effects and terrain blockages, the combat environment brings its own unique difficulties. The adversary brings electronic warfare efforts to bear on the already crowded electromagnetic spectrum and friendly interference sources. As if these were not enough, consider that the battlefield of today's soldiers, sailors, airmen and marines is the city block. In Bosnia, Somalia, and now in Iraq, urban warfare has become the adversary's answer to the asymmetrical size and power of the US military. The urban environment brings its own adverse effects on wireless communications. The US Army Field Manual 3-06.11, "COMBINED ARMS OPERATIONS IN URBAN TERRAIN" in addition to other topics, dedicates an appendix to advising soldiers on how to provide communications capability in the "complexities" of the urban environment [1].

The urban environment is not a new challenge to the communications world. In the civilian sector, the desire for convenience has birthed numerous wireless connectivity technologies. Cellular phones have provided voice and data connectivity to customers on the move for decades. Wireless networks are now beginning to cover the urban landscape, providing personal digital assistants and laptop computers internet connectivity at home, work, restaurants and coffee shops. Connectivity and convenience are not without challenge. Obstructions, reflections and interference have been the bane of reliable service, as seen in a family of cellular phone service advertisements. In the commercials, a well-dressed man roams the nation with a cell phone to his ear and asks "Can you hear me now?"

Whether in the military or the civilian sector, overcoming the reality of the harsh communications environment is topic of a diverse body of research. Part of that body is the application of spectral encoding techniques. The transform domain

communication system (TDCS) has historically applied spectral encoding techniques to the problem of interference avoidance.

The history of TDCS research by that name reaches at least back to the mid-1990s when Radcliffe published his thesis entitled, "Design and Simulation of a Transform Domain Communications System" [9]. His research spurred a body of work at AFIT exploring the application of spectral encoding to interference suppression. Swackhammer researched and simulated a multiple access scheme using pseudo-random (PR) phase encoding and cyclic shift keying (CSK) for modulation [13]. Roberts researched synchronization issues with TDCS, and most recently Nunez applied M-ary phase shift keying (MPSK) to multiple access TDCS systems [11] [6].

This thesis continues the research on the application of spectral encoding using the TDCS. The specific application of spectral encoding in this research is to overcome another reality of the communications environment: the reflections that cause multipath fading.

1.2 Problem Statement

The multipath fading channel adversely impacts wireless communications. The receipt of out-of-phase reflections at the receiver degrades performance in the communications system. This research applies spectral encoding techniques to improve performance over a multipath fading channel.

1.3 Goals

The specific overarching research goals are:

1. To compare the bit error rate performance of spectrally encoded "shaped spectrum" TDCS signals to un-encoded "flat spectrum" TDCS signals in a frequency-selective, slowly-fading (FSSF) multipath channel using an L-diversity TDCS RAKE receiver.

2. To evaluate the interference rejection capability of an L-diversity TDCS RAKE receiver using spectrally encoded, shaped spectrum TDCS signals in a FSSF, multipath channel.

1.4 Scope

This research is restricted to examining the spectrally encoded TDCS and the FSSF multipath channel with and without a narrow band interference source. The research does not delve into channel estimation, spectral estimation, different types of interference sources, different modulation techniques or multiple access techniques.

1.5 Assumptions

This research is based on the following assumptions:

1. The TDCS transmitter/receiver pair use equal energy, antipodal, binary phase shift keying. (BPSK) signaling.
2. The TDCS transmitter is continuously transmitting.
3. The real-world effects of radio frequency (RF) hardware in the TDCS transmitter/receiver pair are ignored. All amplifiers, filter, and antennas are assume to have unity gain.
4. The effects of transmission loss are accounted for in signal-to-noise ratio (SNR).
5. The TDCS transmitter/receiver pair achieve perfect spectral estimates.
6. The TDCS transmitter/receiver pair perfectly estimate the channel transfer function/impulse response.
7. The TDCS transmitter and receiver are perfectly synchronized with respect to timing and spectral coding characteristics.
8. The multipath fading channel is modeled as a Rayleigh fading channel.
9. The multipath fading channel model returns on average 100% of the energy transmitted through the channel.

10. All doppler effects are ignored.

11. Since all modelling occurs at baseband, with low-pass equivalent channel models, the additive white Gaussian noise (AWGN) is generated with a one-sided power spectral density (PSD) of N_o.

1.6 Methodology

To achieve the research goals, both analysis and simulation are used. Mathematical analysis, including closed-form and numerical solutions are used to predict the performance of the spectrally encoded TDCS in various situations. The analysis is verified using Monte Carlo simulation techniques.

1.7 Materials and Equipment

All simulations are run using `Matlab`® Version 7.0.0.19920 (R14). Simulations are run on stand alone PCs running Windows XP as well as the AFIT Unix Clusters.

1.8 Overview

This research is organized as follows. Chapter II contains the literature search. It provides the mathematical background on TDCS performance prediction, multipath fading channel effects on communications system performance prediction and the L-diversity RAKE receiver. Chapter III contains the analysis and analytical results of this research. The background information presented in the Literature Search is used in the analysis to predict the performance of spectrally encoded TDCS signals over multipath fading channels. The methodology in Chapter IV describes the system under test and the design of experiments for the simulation portion of the research. Chapter V presents the results of both the analysis and simulation. A comparison of the analytical predictions to the simulated results is discussed for each type of simulation. Finally, Chapter VI contains the conclusions of this research and potential directions for future studies.

II. Literature Review

This chapter provides the analytical background required for this research. Introductions to the TDCS, the fading channel and L-diversity are presented.

2.1 The Function of a TDCS

The basic premise of using a TDCS to combat interference is that the communications waveform can be designed to have spectral characteristics that completely avoid the spectrum occupied by the interference source. It is this spectral flexibility that is used to enhance the performance of the communication system in a multipath environment. The basic function of a TDCS described below shows how an MPSK TDCS generates communications waveforms that have desirable spectral characteristics.

Diagrams of a typical TDCS transmitter/receiver pair are shown in Figures 2.1 and 2.2. The basic operation of a TDCS begins as a Discrete Fourier Transform (DFT) or other spectral estimation technique is applied to determine the current spectral environment. The measured magnitude spectrum is processed to identify frequencies with potential interference sources using one of many algorithms (e.g. thresholding). Frequency components A_p identified as potentially containing interference sources are notched in the construction of the communications waveform, effectively filtering out the interferer's power over the notched frequencies. Out of the original P frequencies, those which remain after processing are phase encoded to generate the $M = 2^k$ fundamental signaling waveforms (FSW).

Since each of the frequency components that are used to construct the FSWs can be assigned an independent phase, the information content in the waveform is encoded in the phase spectrum. There are multiple methods cited in the literature to encode both data symbol and multiple access information within the phase [6, 9, 13]. Both cyclic shift keying and phase shift keying have been used to encode symbol data. For multi-access encoding, pseudo-random and linear phase codes have been used.

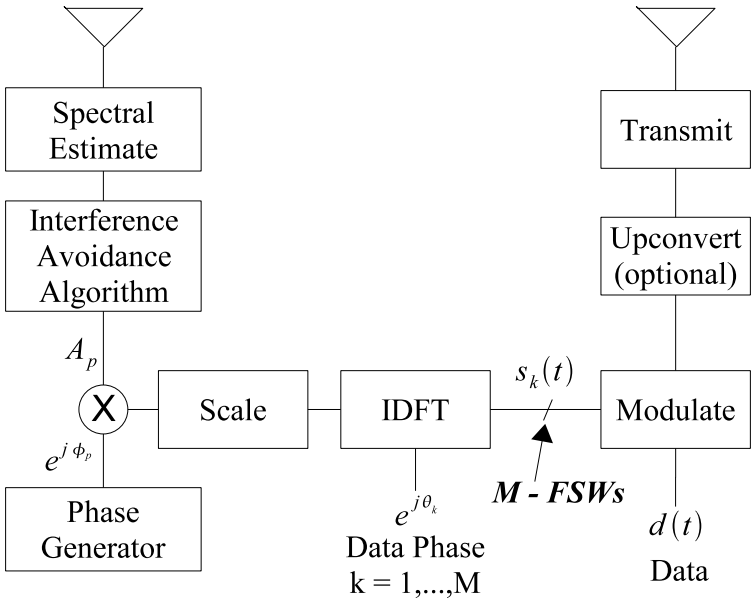

Figure 2.1: Conceptual TDCS Transmitter

Once the magnitude and phase spectrum for the FSWs are established, the spectrum magnitudes are scaled to maintain a constant signal energy. Then, an Inverse Discrete Fourier Transform (IDFT) is performed on the notched, phase-encoded and scaled spectra to construct time-domain representations of the M FSWs.

To modulate data, the TDCS transmitter converts k data bits d_i to one of M symbols. The FSW for each symbol is then converted from digital to analog to modulate each symbol. There is also the potential to carrier modulate each symbol before amplification and transmission through the channel.

A scenario in which a TDCS constructs communications signals to avoid an interference source can be easily illustrated. If a typical interfering source has the spectral characteristics shown in Figure 2.3 [6, 4-3,4], then after utilizing a simple thresholding algorithm, the magnitudes of the TDCS frequency components A_p are shown in Figure 2.4. The notched TDCS magnitude spectrum has no energy in frequency bands where the interferer's energy is highest. Note that the example spectra are two-sided.

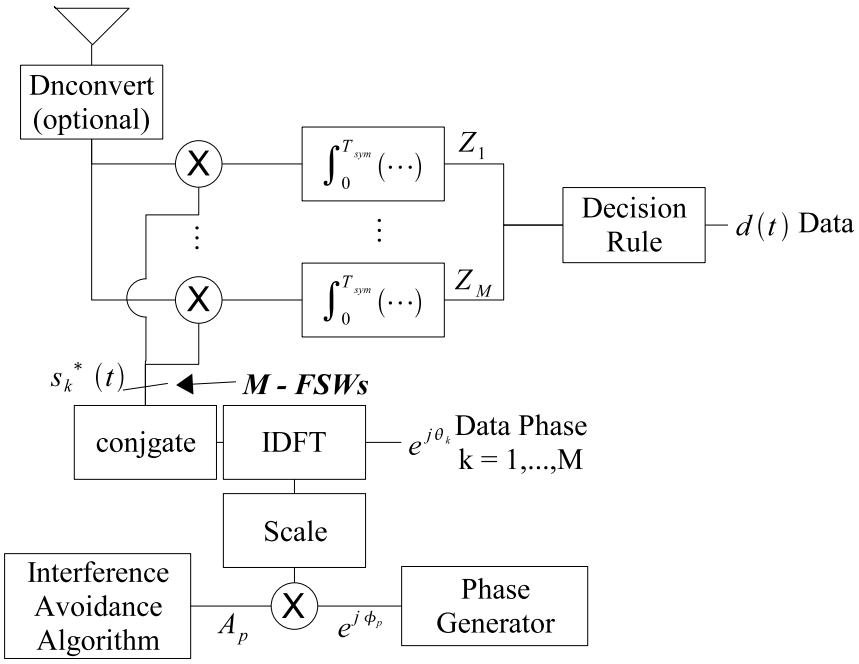

Figure 2.2: Conceptual TDCS Receiver

To detect and estimate transmitted TDCS signals, the receiver is designed to perform coherent demodulation. From the diagram in Figure 2.2, it can be seen that the receiver uses the same process as the transmitter to generate the fundamental signaling waveforms. While the receiver may or may not "see" the same spectral environment as the transmitter, it is assumed that the transmitter and receiver, after initial synchronization, can communicate the required spectral characteristics of the FSWs to each other. The receiver generates the M FSWs using the same magnitudes and phase-encoding scheme as the transmitter, which then allows the receiver to construct the complex conjugate of the FSWs and use a matched filter demodulator to coherently detect and estimate symbols. Nunez' research showed that using the TDCS transmitter/reciever architecture described above allows accurate probability of bit error prediction using standard MPSK analytical models [6, 4-6]. This research uses strictly BPSK, for which the standard probability of bit error (P_b) relationship to the normalized bit energy to noise power spectral density (E_b/N_o) is given by (2.1) [8, 268].

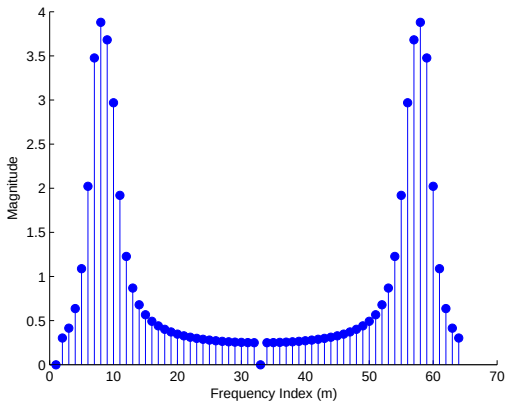

Figure 2.3: Conceptual Interference Source

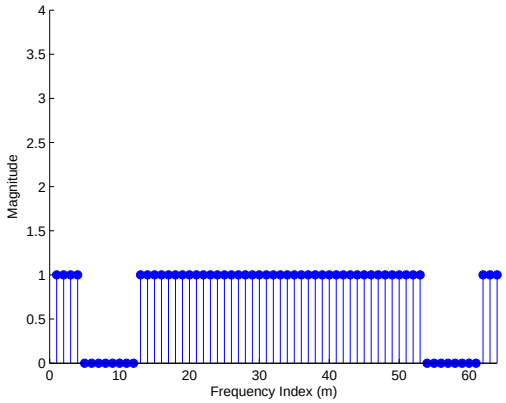

Figure 2.4: Conceptual TDCS Notched Signaling Spectra

$$P_b = Q\left(\sqrt{\frac{2E_b}{N_o}}\right) \tag{2.1}$$

where $Q(x)$ is defined as [8, 40]:

$$Q(x) = \frac{1}{\sqrt{2\pi}} \int_x^\infty e^{-x^2/2} dx, \qquad x \geq 0 \tag{2.2}$$

The analytical, continuous-time model for a baseband MPSK TDCS symbol $s_k(t)$ is given by (2.3).

$$s_k(t) = 2 \sum_{p=0}^{P-1} A_p \, cos\left(2\pi f_{sb} p t + \phi_p + \theta_k\right) \quad t_o \leq t \leq t_o + T_{sb} \tag{2.3}$$

where the following parameters are defined:

P is the number of frequency components available to construct the TDCS waveform.

f_{sb} is the fundamental frequency of the waveform. All other components are integer multiples of the fundamental frequency to ensure orthogonality. Note also that the period T_{sb} is equal to the symbol duration T_{sym} and therefore, $T_{sb} = 1/f_{sb} = T_{sym}$.

A_p is the magnitude of the p^{th} frequency component in waveform.

ϕ_p is the random phase for each frequency component of the waveform. It is used to make the time-domain representation of the signal more featureless and has been used in previous work to encode the multi-access phase assignment. [6, 3-5].

θ_k is the data modulation phase for the k^{th} symbol and is independent of p. The data phase is consistent across all frequency components of the symbol for PSK.

Assuming the system sampling frequency is an integer multiple of f_{sb}, and equal to $2f_{sb}P$ to avoid aliasing, the discrete-time model for $s_k(t)$ in (2.3) is shown in (2.4) [6, 3-2].

$$s_k[n] = \frac{2}{N}\sum_{p=0}^{P-1} A_p \, cos\left(2\pi p\frac{n}{N} + \phi_p + \theta_k\right) \quad 0 \le n \le N-1 \quad \text{where } N = 2P \tag{2.4}$$

From Equations 2.3 and 2.4, we can determine the frequency domain representations of the symbols. Noting that the continuous-time representation of the symbol is a sum of cosines windowed by a `rect` function, the continuous frequency representation is found in (2.5).

$$S_k(f) = \sum_{p=0}^{P-1} A_p \left\{ \text{sinc}\Big[T_{sb}(f - pf_{sb})\Big] e^{+j(\phi_p+\theta_k)} + \text{sinc}\Big[T_{sb}(f + pf_{sb})\Big] e^{-j(\phi_p+\theta_k)} \right\} \tag{2.5}$$

where:

$$\text{sinc}(x) = \frac{\sin(\pi x)}{\pi x} \tag{2.6}$$

Making the same sampling assumption as above, the discrete-frequency representation of (2.3) is found in (2.7) [6, 3-2].

$$S_k[m] = \begin{cases} A_p e^{+j(\phi_p+\theta_k)} & \text{if } m = p \quad \forall p \in (0, P-1) \\ A_p e^{-j(\phi_p+\theta_k)} & \text{if } m = N-1-p \quad \forall p \in (0, P-1) \\ 0 & \text{otherwise} \end{cases} \tag{2.7}$$

2.1.1 TDCS Performance Against Interference. Now that the basic function and analytical models for the TDCS have been presented, the performance of a such a system against an interference source is examined. There are a number of different interferer models that have been simulated against a TDCS. The ability of a TDCS to suppress narrow-band and partial-band interference sources has been demonstrated in both [6, 9]. The basic model for an interferer and its effect on TDCS performance is demonstrated as follows.

Using the information presented earlier on the function of a TDCS, assume a generic interference source is received by a TDCS receiver. The discrete-frequency representation of the interference source is shown in (2.8).

$$J[m] = J_m e^{j\Theta_m} \quad \forall m \in [0, N-1] \tag{2.8}$$

In the discrete representation above, J_m represents spectral magnitude and Θ_m is the spectral phase. It can also be shown that the amount of energy from the interference source that is received by the TDCS receiver in a single symbol duration J_i' is given by (2.9).

$$J_i' = \frac{1}{N} \sum_{p=0}^{N-1} J_p^2 \tag{2.9}$$

However, as discussed earlier, the TDCS is designed to mitigate the effects of interference sources in the frequency domain. Several methods for excising interference using a TDCS are reviewed in [9, 6-7]. For simplicity, this research assumes a simple thresholding algorithm is used to avoid interference. The algorithm creates a notch in

the TDCS spectrum by setting $A_p = 0$ for all components where the spectral estimate exceeds a given threshold. If the system creates a notch in the FSWs over spectral indices $m \in (j_l, j_h)$ and $m \in (N-1-j_h, N-1-j_l)$, then the amount of energy from the interference source present in the test statistic, J_i is given by (2.10).

$$J_i = \frac{1}{N}\left[\sum_{p=0}^{j_l-1} J_p^2 + \sum_{p=j_h+1}^{N-1-(j_h+1)} J_p^2 + \sum_{p=N-1-(j_l-1)}^{N-1} J_p^2\right] \tag{2.10}$$

If the phases of the interfering signal are assumed to be uniformly random, then the energy in the test statistic J_i can now be treated as AWGN. Therefore (2.11) is the theoretical prediction for the probability of bit error P_b in the presence of an interferer [12, 760].

$$P_b = Q\left(\sqrt{\frac{2E_b}{N_o + N_i}}\right) \tag{2.11}$$

where $N_i/2$ is the average power of the interferer P_i divided by the bandwidth of the TDCS signal and given by:

$$\frac{N_i}{2} = \frac{P_i}{2W_{BB}} = \frac{J_i}{T_{sym}} \cdot \frac{1}{2W_{BB}} = \frac{J_i f_{sb}}{2Pf_{sb}} = \frac{J_i}{2P} \tag{2.12}$$

The review of the TDCS and the associated interference avoidance capability using spectral encoding techniques is now complete. Now the literature survey turns to the central focus of this research, the fading channel.

2.2 Introduction to the Fading Channel

One of the basic assumptions behind all of the previous TDCS research at AFIT has been that the channel is strictly AWGN. While this assumption is a valid starting point for academic research, it is not reflective of more realistic communication environments. Ionospheric and tropospheric scattering occur due to constant physical motion of ions in the atmosphere [8, 800]. Additionally, built-up structures and terrain features (e.g. mountains), can cause reflections or obstructions in the channel. The overall result of scattering, reflection and obstruction is that a number of replicas

of the transmitted signal, called multipath waves, arrive at the receiver instead of the single received signal modeled by the AWGN channel [10, 139]. Each of these multipath waves have distinct and randomly distributed amplitude and phases, which when combined at the receiver cause constructive or destructive interference [10, 140].

An added complication of multipath environments is that they vary in time. Ionospheric scatter varies by the nature of the motion of the particles suspended in the atmosphere [8, 800]. Mobility in urban communications environments, either by the transmitter/receiver pair or the obstructions and reflectors, causes changes in the channel over time [10, 139]. Overall, the time variation leads to the characteristics of the channel appearing random to the user [8, 800]. Next an analytical model of a multipath fading channel is introduced.

To characterize the multipath channels, we look first to the time-varying impulse response. Since the source analysis applies to bandpass systems, the low-pass equivalent channel is analyzed. The low-pass channel equivalent can be represented by a sum of complex-valued, time-varying, delayed impulse responses [8, 802]. As in the impulse response in (2.13) and for the remainder of this document, the subscript l indicates that the complex low-pass equivalent is represented.

$$h_l(\tau, t) = \sum_{n=1}^{L} c_n(t)\delta(\tau - \tau_n(t)) = \sum_{n=1}^{L} \alpha_n(t)e^{j\Theta_n(t)}\delta(t - \tau_n(t)) \tag{2.13}$$

where, $\delta(t)$ denotes the Dirac delta function described by [15]:

$$\int_{-\infty}^{\infty} f(t)\delta(t-a)\,dt = f(a) \tag{2.14}$$

$$\delta(t-a) = 0 \qquad t \neq a \tag{2.15}$$

In (2.13), $c_n(t)$, $\alpha_n(t)$, $\Theta_n(t)$ and $\tau_n(t)$ are the time-varying complex coefficient, magnitude, phase, and delay of the n^{th} multipath wave respectively. In (2.13), the variable t denotes absolute time and τ is the delay beyond the absolute time. L is the number of multipath waves received. The statistics for the coefficients c_n of the channel

impulse response in (2.13) can be modeled using different distributions [8, 803]. To limit the scope of this research, the following model is adopted for this research. The $c_n(t)$ are assumed to be zero-mean, complex-valued Gaussian random processes. Since the magnitude of a such a random process is Rayleigh distributed, this model represents a Rayleigh Fading Channel [8, 803]. Equations (2.16) and (2.17) show the corresponding distributions for $\alpha_n(t)$ and $\Theta_n(t)$.

$$\alpha_n(t) \sim \text{Rayleigh}(\sigma) \tag{2.16}$$

$$\Theta_n(t) \sim \text{Uniform}(-\pi, \pi) \tag{2.17}$$

A Rayleigh fading model is typically used to model situations where there is no dominant stationary signal component (i.e. line-of-sight (LOS) propagation path). For example, in an urban environment, the LOS path may arrive with a signal strength on the same order of magnitude as the multipath waves. This effect results in a Rayleigh type fading channel [10, 174].

There are a number of channel characteristics that can help the reader understand the effects of a multipath fading channel on a communication system. These characteristics can be derived from the autocorrelation of the channel impulse response $h_l(\tau, t)$ and time-variant transfer function $H_l(f, t)$ defined as:

$$H_l(f,t) = \int_{-\infty}^{\infty} h_l(\tau, t) e^{-j2\pi f\tau} d\tau \tag{2.18}$$

An extensive treatment of the autocorrelation functions can be found in Proakis' text [8, 804]. The most notable characteristics that describe the channel are listed and described here along with the manner in which they effect communications signals traversing the channel. The first characteristic of interest is the *multipath spread* of the channel, given the label T_m. The multipath spread of the channel defines the maximum length of the delay observed in the channel. In a communications system, it is a measure of the amount of intersymbol interference induced by the channel and

is also related to the amount of diversity in the channel. The second characteristic is the *coherence bandwidth* of the channel, labelled $(\Delta f)_c$. The coherence bandwidth indicates the bandwidth over which the channel treats signals approximately the same. If the baseband bandwidth of a signal W_{BB} is greater than $(\Delta f)_c$, then the channel must be considered *frequency-selective*. If the channel is frequency-selective, then the analysis must consider how the channel affects the communications system differently in distinct parts of the frequency domain. If the opposite is true ($W_{BB} < (\Delta f)_c$), then the channel is considered *frequency non-selective*, and the analysis can consider all parts of the communications signal affected equally. The third characteristic is the *Doppler spread*, labelled B_d. The Doppler spread of the channel is a measure of the amount of frequency spreading due to time variation in the channel. The fourth characteristic is the reciprocal of the Doppler spread, named the *coherence time* of the channel, and labelled $(\Delta t)_c$. The coherence time is a measure of the amount of time over which the channel can be considered to have time-invariant behavior. Equations (2.19) and (2.20) show the relationships between the four characteristics mentioned above [8, 804-807]:

$$(\Delta f)_c \approx \frac{1}{T_m} \tag{2.19}$$

$$(\Delta t)_c \approx \frac{1}{B_d} \tag{2.20}$$

2.2.1 How Multipath Parameters Impact the Channel Model. The relationship of the four channel characteristics to the communications system parameters define the ways in which the analytical model for the fading multipath channel may be simplified. Consider a communication system with symbol duration, T_{sym} and baseband bandwidth, W_{BB}, where bandwidth is defined as positive frequencies occupied. If $T_{sym} >> T_m$, then in the analysis, intersymbol interference can be considered negligible. The selection of the symbol duration also affects the consideration of time variations in the channel. If $T_{sym} << (\Delta t)_c$, then the channel is considered slowly-fading, i.e. the channel impulse response and transfer function are considered to be

fixed over the entire communications symbol duration. If this is true, the time dependency can be removed from the channel impulse response and transfer function expressions, as shown in (2.21) and (2.22).

$$h_l(\tau) = \sum_{n=1}^{L} c_n \delta(\tau - \tau_n) = \sum_{n=1}^{L} \alpha_n e^{j\Theta_n} \delta(t - \tau_n) \qquad 0 \leq \tau \leq T_{sym} \tag{2.21}$$

$$H_l(f) = \int_{-\infty}^{\infty} h(\tau) e^{-j2\pi f \tau} d\tau \tag{2.22}$$

As mentioned above, the selection of the communication system bandwidth determines whether the channel is considered frequency-selective or nonselective. If $W_{BB} << (\Delta f)_c$, then the channel is frequency non-selective. A consequence of a frequency-nonselective channel is that the multipath components (reflections) arriving at the receiver are not resolvable [8, 815]. Therefore the channel can be modeled as a single amplitude and phase term with a random distribution. In contrast, if $W_{BB} >> (\Delta f)_c$, then the channel is frequency-selective and the individual reflections from the channel are resolvable. In this case the channel may be modeled as a tapped delay line with independent random amplitudes and phases at each tap. There is one last simplification of the channel model that can be made depending on the bandwidth of the signal. Provided $W_{BB} >> B_d$, the effects of doppler shift in the received signal are negligible in the receiver [10, 165].

2.2.2 Typical Cellular Channel Models. Multipath fading is a fact of life in cellular phone channels and manifests itself in many ways. However, the goal in this section is not to perform an exhaustive study of channel characteristics, but to refer to some typical measured values for systems operating in the 900MHz band. The purpose of this quick overview is to show that a combination of channel characteristics and TDCS parameters can be conceived such that the multipath fading channel can be modeled as a frequency-selective, slowly-fading multipath channel. The characteristics of multipath channels have been studied, measured and characterized by many authors [8] [10]. Rappaport cites several characteristics for urban and suburban environments

measured in the 900MHz frequency band [10, 162]. Specifically, he presents measured values for the root mean square (RMS) delay spread T_m as shown in Table 2.1. These statistics are shown with the corresponding coherence bandwidths $(\Delta f)_c$ using (2.19).

Table 2.1: Typical Measured RMS Delay Spread and Corresponding Coherence Bandwidths

Environment	T_m in μs [10, 162]	$(\Delta f)_c$ in kHz
Suburban: Typical	0.2-0.3	3,300-5,000
Suburban: Worst	1.9-2.1	475-525
Urban: Typical	1.3-3.5	286-769
Urban: Worst	10-25	40-100

Using these statistics, the TDCS parameters can now be determined so that the channel can be modeled as both a frequency-selective and slowly-fading channel.

First, the criteria for frequency selectivity is determined. Since the bandwidth of the system, W_{BB} must be much larger than the coherence bandwidth, $(\Delta f)_c$. Using (2.5), it can be shown that the zero to null baseband bandwidth, W_{BB} of a TDCS signal is Pf_{sb} Hz. The IS-95 cellular phone system data rate is 9.6kHz, therefore as a means of comparison, it is assumed that the TDCS f_{sb} is 10kHz [4]. Based on this assumption, P in the TDCS symbols must be chosen such that W_{BB} is greater than $(\Delta f)_c$. Using the information in Table 2.1, the W_{BB} for the TDCS signals must exceed 0.7-5MHz for the channel to be considered frequency-selective. Therefore, if $f_{sb} = 10$kHz, P must greater than 500 to meet this criteria in suburban environments, and greater than 76.9 for urban environments.

Next, the criteria for a slowly-fading channel is addressed. Recall that this criteria is related to the coherence time $(\Delta t)_c$, which is inversely related to the doppler spread B_d. In most cases, the significant amount of doppler spread in the channel is due to the relative motion between the transmitter, the receiver and the entities causing the delayed reflections in the environment. In this case, B_d can be derived from the relative velocity v between moving entities and the wavelength λ of the communications signal using $B_d = v/\lambda$. In Section 2.2, it was shown that $(\Delta t)_c$ is the simple reciprocal of B_d; however, in practice this relationship yields the maxi-

mum $(\Delta t)_c$. Equations (2.23) through (2.25) show two other approximations used in practice, which provide a range of values for $(\Delta t)_c$ [10, 165].

$$(\Delta t)_c \approx \frac{1}{B_d} \quad \text{Maximum} \tag{2.23}$$

$$(\Delta t)_c \approx \frac{9}{16\pi B_d} \quad \text{Minimum} \tag{2.24}$$

$$(\Delta t)_c \approx \sqrt{\frac{9}{16\pi B_d^2}} \quad \text{geometric mean of max and min above} \tag{2.25}$$

To meet the requirements for a slowly-fading channel, $(\Delta t)_c$ must be many times longer than the symbol duration, $T_{sym} = T_{sb}$. Establishment of this criteria also dictates the fundamental frequency f_{sb} of the waveform, as defined earlier in (2.3). To show that the slowly fading assumption is reasonable for a typical cellular channel frequency and mobility, Table 2.2 shows the number of symbol durations contained in $(\Delta t)_c$ given f_{sb} is 10kHz, center frequency f_c is 900MHz, and relative velocity is 100km/h for the three different approximations given in Equations (2.23), (2.24) and (2.25). These numbers indicate that a range of 21-120 symbols can be transmitted at typical cell phone symbol rates while the channel characteristics remain stable.

Table 2.2: Number of Symbols in Coherence Time at $f_{sb} = 10$kHz, $f_c = 900$MHz and $v = 100$kmph

$(\Delta t)_c$ **Approximation**	**Number of Symbols**
Maximum	120
Mean	50
Minimum	21

Using the assumptions above, the doppler spread for the typical cellular phone channel at 900MHz is computed to be approximately 83Hz. Given the TDCS bandwidths considered above (0.7-5MHz) for the frequency selectivity discussion, Rappaport's assumption that doppler spread effects can be ignored when the baseband bandwidth is much greater than the coherence bandwidth is reasonable; therefore, the effects of doppler spread are ignored in the channel model.

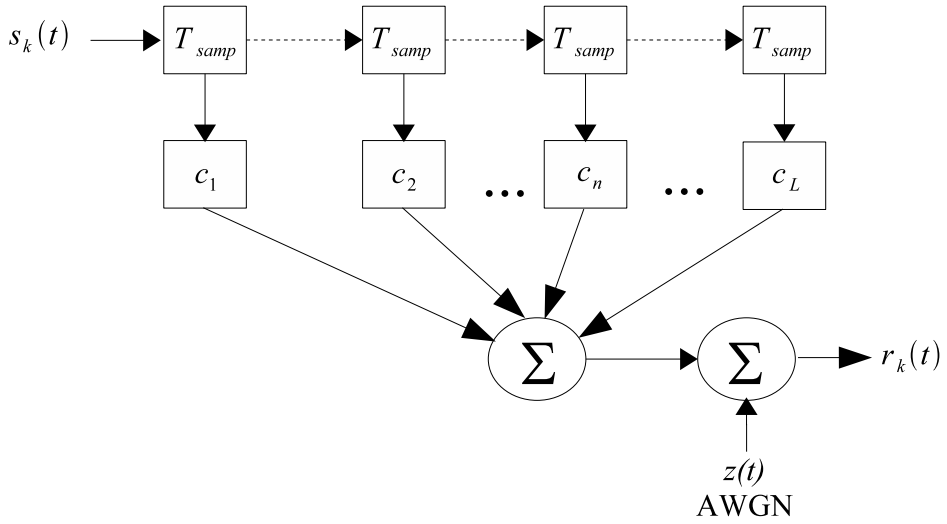

Figure 2.5: Tapped Delay Line Model of a Frequency-Selective, Slowly-Fading (FSSF) Multipath Channel

Based on the information presented above, for the remainder of this research, it is assumed that the channel behaves as a FSSF multipath channel. Now the model for the channel can be introduced.

2.2.3 Frequency-Selective, Slowly-Fading (FSSF) Channel Model. The analytical model for a FSSF multipath channel is a tapped delay line [8, 842]. The model of the channel is graphically depicted in Figure 2.5, and the time and frequency domain analytical models in (2.26) and (2.27) are used.

$$h_l(\tau) = \sum_{n=1}^{L} c_n \delta(\tau - \tau_n) = \sum_{n=1}^{L} \alpha_n e^{j\Theta_n} \delta(t - \tau_n) \qquad 0 \leq \tau \leq T_{sym} \tag{2.26}$$

$$H_l(f) = \int_{-\infty}^{\infty} h_l(\tau) e^{-j2\pi f\tau} d\tau \tag{2.27}$$

If it is assumed that the system is operating in the digital domain in accordance with the sampling assumption stated in Section 2.1, then the resolution of the multipath profile in the time domain is as fine as the sampling interval, $T_{samp} = 1/f_{samp}$. Therefore, the τ_n terms in (2.26) can be replaced with the expression nT_{samp}. Here, L is

related to T_m and T_{samp} as stated in (2.28) [8, 841].

$$L = \lfloor T_m / T_{samp} \rfloor + 1 \tag{2.28}$$

where $\lfloor x \rfloor$ denotes the largest integer not to exceed x.

Now the discrete representation of the impulse response $h_l[n]$ can be expressed as shown in (2.29).

$$h_l[n] = \sum_{i=1}^{L} c_i \delta[n-i] = \sum_{i=1}^{L} \alpha_i e^{j\Theta_i} \delta[n-i] \qquad n \in (0, N-1) \tag{2.29}$$

which is given in the following abbreviated notation for the remainder of the thesis:

$$h_l[n] = \begin{cases} c_n = \alpha_n e^{j\Theta_n} & n \in (1, L), \\ 0 & \text{otherwise.} \end{cases} \tag{2.30}$$

To express the channel transfer function in the discrete frequency domain $H_l[m]$, the definition of the discrete Fourier transform (DFT) is applied in (2.31). Assume that the sequence c_n is zero-padded to length N and that an N-point DFT is calculated.

$$H_l[m] = \sum_{n=1}^{L} c_n e^{j2\pi nm/N} \quad m \in (0, N-1) \tag{2.31}$$

$$= C_m \equiv H_m e^{j\theta_m} \tag{2.32}$$

where:

$$H_m = |C_m| \quad \text{and} \quad \theta_m = \arg C_m \tag{2.33}$$

For the remainder of the research, the abbreviated notation for the discrete channel transfer function is C_m along with the magnitude and phase terms H_m and θ_m as defined in Equations 2.33. The stochastic characterization of the channel transfer function is located in Section A.1 of Appendix A. Here the result of this derivation,

the distribution of H_m^2 is given in (2.34).

$$f_{H_m^2}(H_m^2) = \frac{e^{-H_m^2/2L\sigma^2}}{2L\sigma^2} \tag{2.34}$$

The distribution in (2.34) is characterized as a scaled Chi-squared random variable with 2 degrees of freedom. The derivation of this distribution lends insight that is valuable in the analysis of bit error rate prediction over the FSSF multipath channel; however, even more valuable at this point is a graphical representation of the channel impulse response and transfer function. A representative discrete-time impulse response for a Rayleigh distributed channel with $L = 16$ taps is shown in Figure 2.6. The associated channel transfer function computed by a zero-padded 128-point DFT is shown in Figure 2.7. The notable aspect of the channel transfer function plot is the presence of "valleys" in the transfer function. These features cause a frequency specific filtering of signals that traverse the channel. While the plots included in Figures 2.6 and 2.7 are only one instantiation of a random channel, the filtering behavior is a typical feature of fading channels, as we can infer from the distribution of the channel transfer function derived in (2.34). It is this filtering behavior that causes degradation of performance in typical communication systems and that the application of spectral encoding in the TDCS can mitigate.

This completes the discussion of the channel model. The graphical representation, time and frequency domain analytical models, associated statistical distributions and anecdotal illustration of behavior have been shown.

2.2.4 Channel Estimation. One of the key assumptions for this research is that the channel is perfectly estimated, therefore the model tap weights are known exactly. As before, the purpose of this section is not to provide a survey of all channel estimation research; however, enough is presented to provide a foundation for the assumptions made in the research. The literature suggests it may be assumed that the channel coefficients can be accurately estimated, provided the coherence time of the channel exceeds 100 symbol durations, i.e. $(\Delta t)_c \geq 100T_{sym}$ [8, 847]. The

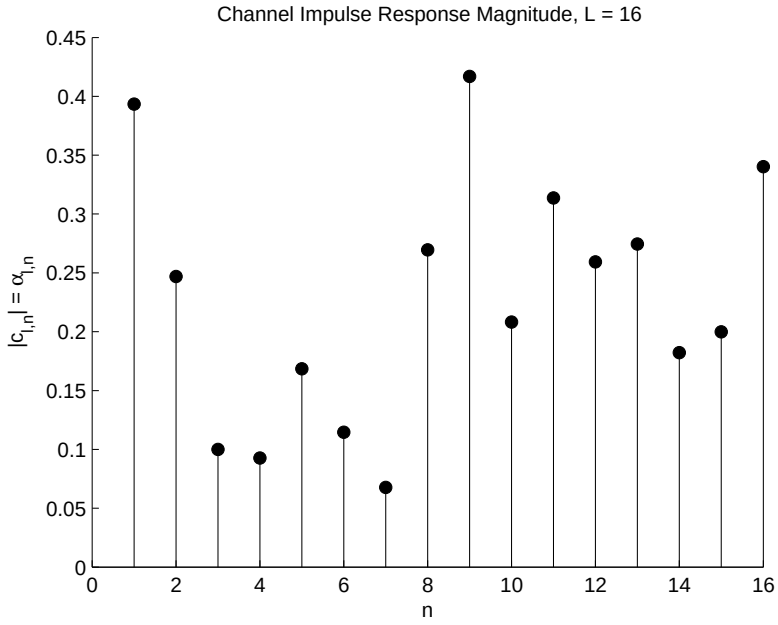

Figure 2.6: **Typical Multipath Channel Impulse Response.** The impulse response above is one instantiation of a fading channel. The magnitudes α_n are independently and identically Rayleigh distributed.

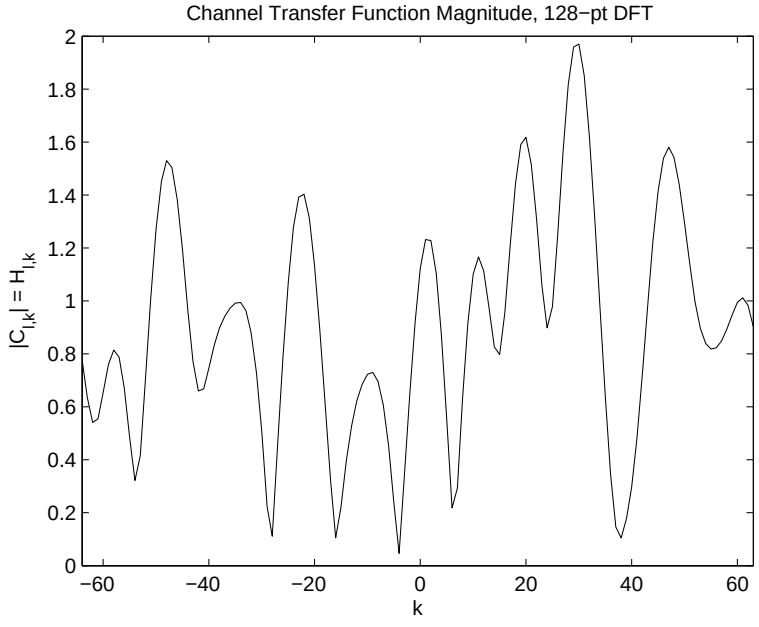

Figure 2.7: **Typical Multipath Channel Transfer Function.** The transfer function, computed using a zero-padded, 128-point DFT shows the "filtering" effects of the fading channel.

literature also provides methods for estimating the channel coefficients when using orthogonal and antipodal signaling [8, 847].

In addition to the methods given in the literature, it is postulated that a training signal could be transmitted periodically that would approximate an impulse. A transmitted TDCS symbol with equal-amplitude frequency components and flat phase response would approximate the channel impulse response c_n at the receiver.

Now that the multipath fading channel model and the applicable channel assumptions for this research have been supported, a method for predicting communication system performance through the channel is analyzed.

2.2.5 Predicting Performance over Multipath Fading Channels. To understand how probability of bit error over a multipath fading channel is predicted, the most simple case is analyzed. As an initial step, the channel is assumed to be frequency *non*-selective and slowly-fading, therefore the multipath components are not resolvable. In a frequency non-selective channel, the received signal appears as a single component with Rayleigh distributed amplitude α and uniformly distributed phase Θ in addition to AWGN $z(t)$ [8, 817]. The analytical model for this received signal is provided in (2.35).

$$r_l(t) = \alpha e^{-j\Theta} s_l(t) + z(t) \tag{2.35}$$

While the complete derivation can be found in [8], an abbreviated version is discussed here as a foundation for further analysis. For a matched filter demodulator operating in an AWGN channel, performance is dictated by the signal-to-noise ratio (SNR) in the demodulator [8, 255]. Because of the multipath channel effects, a distinction between the SNR referenced to the transmitted bit energy and the SNR in the demodulator is made. For the remainder of this research, the normalized bit energy to noise power spectral density ratio E_b/N_o represents the SNR referenced to the transmitted bit energy. Equation (2.36) is the expression for the SNR in the demodulator, abbreviated

γ_b.

$$\gamma_b = \alpha^2 \frac{E_b}{N_o} \tag{2.36}$$

where α is Rayleigh distributed, and α^2 has a Chi-squared distribution with two degrees-of-freedom (DOF). As a random variable, γ_b also has a probability density function (pdf) given by (2.37) [8, 817]. In (2.38), and throughout this thesis, $\mathbf{E}[\cdot]$ is the statistical expected value operator.

$$p(\gamma_b) = \frac{1}{\overline{\gamma_b}} e^{-\gamma_b/\overline{\gamma_b}} \quad \text{where} \tag{2.37}$$

$$\overline{\gamma_b} = \frac{E_b}{N_o} \mathbf{E}[\alpha^2] \tag{2.38}$$

Equation (2.1) establishes P_b for BPSK demodulation. Since γ_b is a random variable, the expected value of (2.1) must be taken over the pdf of γ_b in (2.37) to determine the probability of bit error in a multipath channel $P_{b,mp}$ as shown in (2.39).

$$P_{b,mp} = \mathbf{E}\left[Q(\sqrt{2\gamma_b})\right] = \int_0^\infty Q\left(\sqrt{2\gamma_b}\right) p(\gamma_b) d\gamma_b \tag{2.39}$$

The results of this integration are in (2.40) [8, 818].

$$P_{b,mp} = \frac{1}{2}\left(1 - \sqrt{\frac{\overline{\gamma_b}}{1+\overline{\gamma_b}}}\right) \tag{2.40}$$

While it is not immediately apparent from the analytical result of (2.40), it can be seen from Figure 2.8 that P_b through a multipath channel with just 2 delay taps is much worse than P_b for an equivalent BPSK system at the same E_b/N_o through an AWGN channel.

Now that the method for finding the probability of bit error for a frequency *non*-selective fading channel has been shown, the focus of the research returns to the frequency-*selective*, slowly-fading multipath channel introduced earlier and one method for improving performance in multipath fading channels. Analysis of the FSSF multipath channel requires an adjustment to (2.35) to account for the multiple

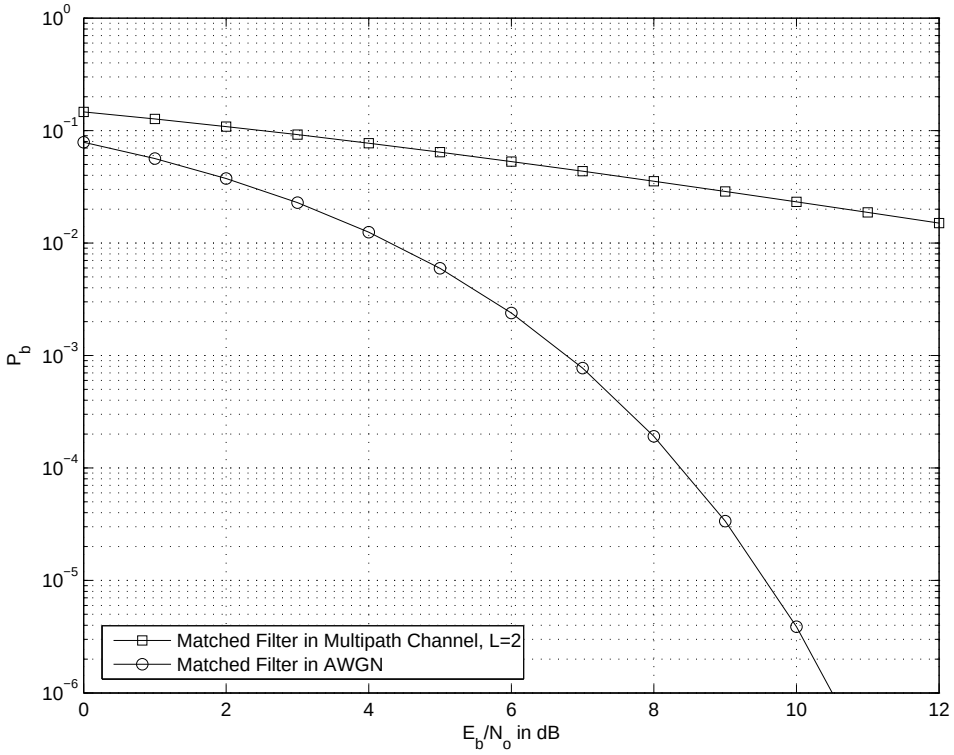

Figure 2.8: **Comparison of P_b for BPSK Demodulators.** This figure demonstrates degradation in the bit error rate of a BPSK matched filter demodulator in a $L = 2$ multipath fading channel when compared to an AWGN channel

delay taps in the model. This adjustment changes the distribution for γ_b; however, the method for computing P_b remains the same.

2.3 Diversity and the RAKE Receiver Model

One way to improve performance over hostile channels without increasing E_b/N_o is to employ diversity. Simply stated, diversity is transmitting information more than one time. Diversity can be introduced into the system in many ways, including repeating the information on different frequencies, at different times or within the digital data stream using block and/or convolutional codes [8, 821]. As alluded to earlier, the FSSF channel can also be a source of diversity.

The RAKE receiver is designed to leverage the replicas of the transmitted signal that are received as reflections through the multipath channel to achieve diversity in

the system. The full derivation of RAKE receiver performance is presented in [8, 842-847]. For clarity, an abbreviated version of the literature is presented here. To determine the performance of the RAKE demodulator in the context of a BPSK system, the derivation begins with the low-pass equivalent of the transmitted signal $s_{l,k}(t)$, which has been transmitted through the FSSF and received as $r_{l,k}(t)$ in (2.41). Recall that the subscripts l and k indicate the complex low-pass equivalent of the k^{th} data symbol respectively.

$$r_{l,k}(t) = \sum_{n=1}^{L} \Big[c_n s_{l,k}(t - nT_{samp}) \Big] + z_l(t) \tag{2.41}$$

If the signal contribution within $r_{l,k}(t)$ is designated $v_{l,k}(t)$, the received signal can be simplified and rewritten as (2.42).

$$r_{l,k}(t) = v_{l,k}(t) + z_l(t) \tag{2.42}$$

From Figure 2.5, recall that $z_l(t)$ is a complex AWGN process. If the c_n are perfectly estimated, as assumed in Section 2.2.4, then it is apparent that the optimum demodulator is a matched filter using $v^*_{l,k}(t)$ as the reference waveform instead of $s^*_{l,k}(t)$ [8, 843]. Upon closer examination, $v_{l,k}(t)$ is a sum of L delayed and scaled versions of the transmitted signal as seen in (2.43).

$$v_{l,k}(t) = \sum_{n=1}^{L} c_n s_{l,k}(t - nT_{samp}) \tag{2.43}$$

A diagram of a typical RAKE receiver is shown in Figure 2.9. In the figure, the test statistics of the RAKE receiver demodulator Z_m are formed by multiplying the received signal $r_{l,k}(t)$ by $v^*_{l,k}(t)$, integrating over a symbol duration, then examining the real part of the result as shown in (2.44) [8, 843]. Symbol estimation in the BPSK system is accomplished by taking the maximum of the two test statistics and mapping them to bits. Although the graphical and analytical representations appear complex, the function of the RAKE receiver is identical to the simple BPSK matched filter

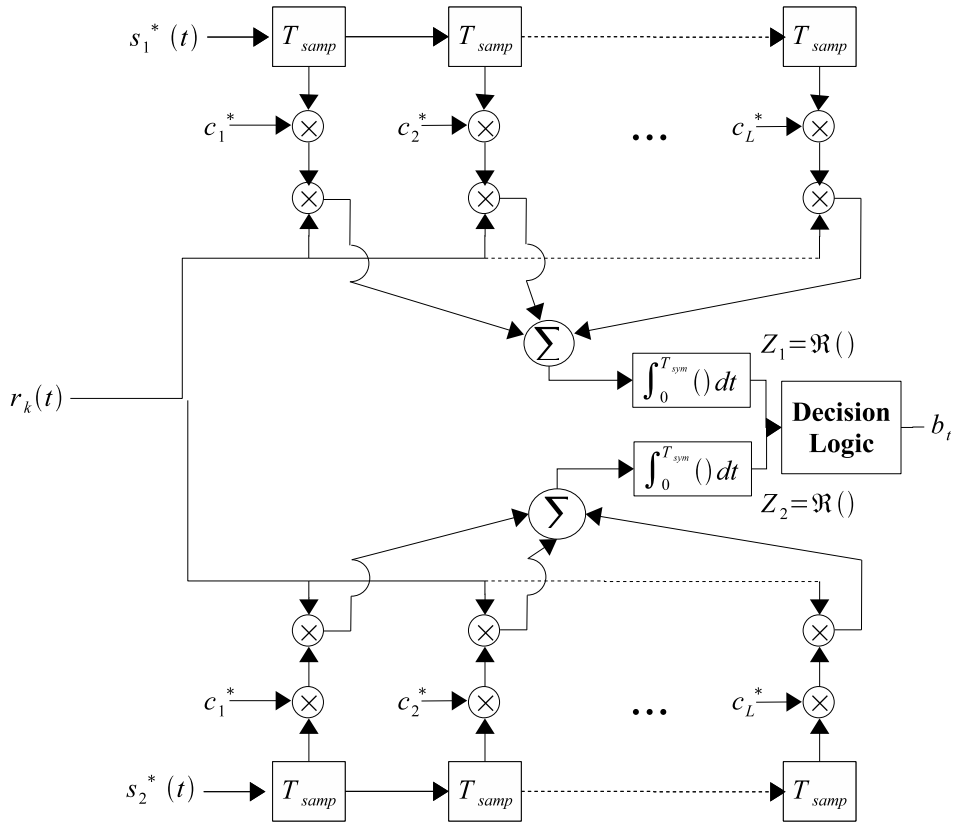

Figure 2.9: Diagram of a RAKE Receiver

demodulator with the exception of the reference waveforms.

$$\begin{aligned} Z_m &= \mathrm{Re}\left[\int_0^{T_{sym}} r_{l,k}(t) v_{l,m}^*(t)dt\right] \quad m = 1, 2 \\ &= \mathrm{Re}\left[\int_0^{T_{sym}} \sum_{n=1}^{L} r_{l,k}(t) c_n^* s_{l,m}^*(t - nT_{samp})dt\right] \end{aligned} \tag{2.44}$$

RAKE demodulator performance is determined by analyzing the statistics of Z_m. Two assumptions simplify the analysis. First, it is assumed that $T_m \ll T_{sym}$, therefore intersymbol interference is ignored in the analysis. Second, the autocorrelation of the transmitted signals or "self-interference" is assumed to be zero outside of $i = j$ as in (2.45) [8, 846]. These assumptions help simplify the analysis here, but are not

applied to TDCS signals in the next chapter.

$$\int_0^{T_{sym}} s_{l,m}(t - iT_{samp}) s_{l,m}^*(t - jT_{samp}) dt \approx 0, \quad i \neq j, \quad m = 1, 2 \tag{2.45}$$

After applying the definition of $r_{l,k}(t)$ to (2.44), expanding the result into nested summations, applying the "self-interference" assumption from (2.45), and substituting $\alpha_n e^{j\Theta_n}$ for c_n, it can be shown that (2.46) follows.

$$\begin{aligned} Z_m &= \text{Re}\left[\sum_{n=1}^{L} \alpha_n^2 \int_0^{T_{sym}} s_{l,k}(t - nT_{samp}) s_{l,m}^*(t - nT_{samp})\, dt\right] + \\ &\quad \text{Re}\left[\sum_{n=1}^{L} \alpha_n e^{-j\Theta_n} \int_0^{T_{sym}} z_l(t) s_{l,m}^*(t - nT_{samp}) dt\right] \end{aligned} \tag{2.46}$$

Intuitively, by examining (2.46), it can be seen that the signal energy contribution in Z_m is a sum of L scaled replicas of the transmitted waveform $s_{l,k}(t)$, and therefore the FSSF multipath channel becomes the source of diversity in the receiver. Note that the scaling factors, while known on a symbol by symbol basis, are random variables. It is from this result that the derivation of performance for the RAKE receiver can be determined.

2.3.1 Probability of Bit Error for an L-Diversity RAKE receiver. The result of the previous section is that the RAKE receiver matched filter has a test statistic dependent on a sum of L scaled versions of the transmitted signal. Therefore, the received SNR γ_b for the RAKE receiver is a sum of L scaled versions of the transmitted SNR E_b/N_o [8, 846]. The outcome of this development is the expression in (2.47) for the performance of an L-diversity RAKE receiver $P_{b,RAKE}$.

$$\begin{aligned} P_{b,RAKE} &= Q(\sqrt{2\gamma_b}), \quad \text{where:} \\ \gamma_b &= \frac{E_b}{N_o} \sum_{n=1}^{L} \alpha_n^2 \end{aligned} \tag{2.47}$$

However, as illustrated in Section 2.2.5, it must be noted that γ_b is not deterministic, but a sum of random variables. To determine the bit error rate for an L-diversity RAKE receiver, the expected value of $P_{b,RAKE}$ must be taken over the pdf of γ_b (a sum of L independent, identically distributed (i.i.d.), Chi-squared random variables with two DOF). After a random variable transformation, and complex integration, [8, 825] has shown the pdf of γ_b and expression for $P_{b,RAKE}$ are as shown in (2.48) and (2.50).

$$p(\gamma_b) = \frac{1}{(L-1)!\bar{\gamma}_c^L}\gamma_b^{L-1}e^{-\gamma_b/\bar{\gamma}_c}, \tag{2.48}$$

where:

$$\bar{\gamma}_c = \frac{E_b}{N_o}\mathbf{E}\left[\alpha_n^2\right] \tag{2.49}$$

$$P_{b,RAKE} = \left[\frac{1}{2}(1-\mu)\right]^L \sum_{k=0}^{L-1}\begin{pmatrix} L-1+k \\ k \end{pmatrix}\left[\frac{1}{2}(1+\mu)\right]^k \tag{2.50}$$

where:

$$\mu = \sqrt{\frac{\bar{\gamma}_c}{1+\bar{\gamma}_c}}$$

The theoretical improvement in bit error rate performance using a RAKE receiver is shown graphically in Figure 2.10 for $L = 2$. Clearly, the performance improvement using an L-diversity BPSK RAKE demodulator is better than that of a BPSK matched filter demodulator without diversity through a multipath fading channel. The performance of a BPSK matched filter demodulator in strictly AWGN is also shown for reference.

In this section a technique for improving probability of bit error performance in a multipath fading channel has been presented. Specifically, in the case of a FSSF multipath fading channel, it has been shown that an L-diversity RAKE demodulator produces a significant improvement over a simple BPSK matched filter demodulator.

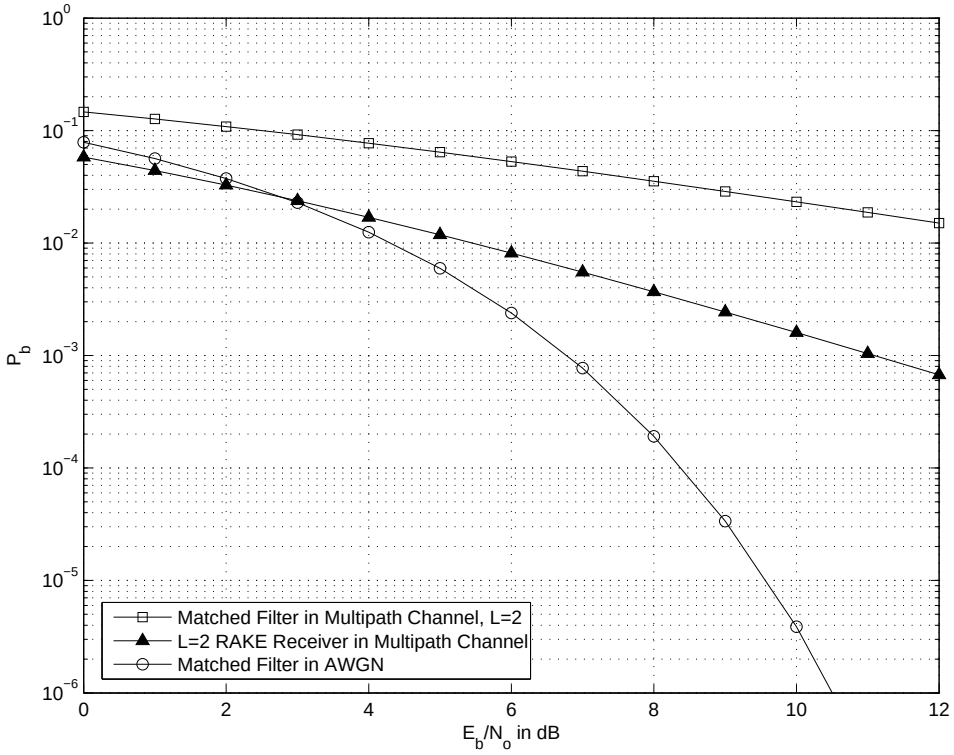

Figure 2.10: **Comparison II of P_b for BPSK Demodulators.** This figure demonstrates the improvement in probability of bit error when an L-diversity RAKE receiver is used in a FSSF multipath channel for $L = 2$.

2.4 Hypothesis

The fundamentals of this research have now been presented. To recap, the function of a TDCS, the interference avoidance capabilities, the multipath fading channel and the L-diversity RAKE receiver have been reviewed. At this point, the hypotheses corresponding to the two overall goals stated in Chapter I of this research are now presented. First, the spectrally encoded, "shaped spectrum" TDCS signals have a lower (better) P_b than that of the un-encoded, "flat spectrum" TDCS signals. The second hypothesis is that the shaped spectrum TDCS signals demonstrate an interference avoidance capability both with and without the notching algorithm applied.

2.4.1 Hypothesis 1: Spectral Encoding. This hypothesis is based on a comparison of the energy that traverses the fading channel for spectrally encoded and

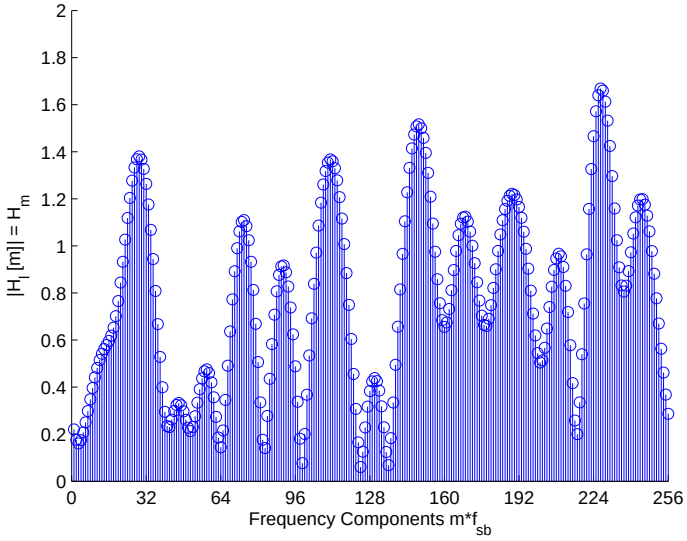

Figure 2.11: Typical Multipath Fading Channel Transfer Function

un-encoded TDCS signals. The evaluation of the energy takes place in the frequency domain and is proved using the Chebyshev Sum Inequality. The full proof is contained in Appendix A.2, with the end result (A.47) demonstrating the energy received from the spectrally encoded, shaped spectrum TDCS signals is greater by an unquantified amount than the energy received from the un-encoded, flat spectrum TDCS signals.

$$\mathcal{E}_{shaped} \geq \mathcal{E}_{flat} \tag{2.51}$$

For illustrative purposes, consider a graphical example. Figure 2.11 represents the magnitude spectrum of a typical FSSF multipath channel transfer function. If an un-encoded, flat spectrum TDCS signal with the magnitude spectrum plotted in Figure 2.12 is transmitted through the channel represented in Figure 2.11, the received signal has the magnitude spectrum shown in Figure 2.14. In contrast, the spectrally encoded, shaped spectrum TDCS magnitude spectrum is encoded using the shape of the channel transfer function. The spectral magnitudes are scaled to maintain equal energy signaling as shown in Figure 2.13. It is apparent from the graphical representations, that the spectrally encoded signals avoid putting energy in frequencies that

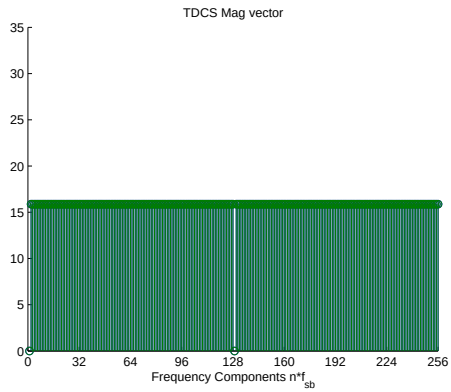

Figure 2.12: Transmitted Un-encoded, Flat Spectrum TDCS Signal

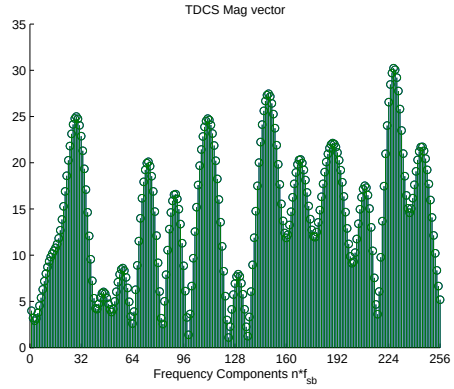

Figure 2.13: Transmitted Spectrally Encoded, Shaped Spectrum TDCS Signal

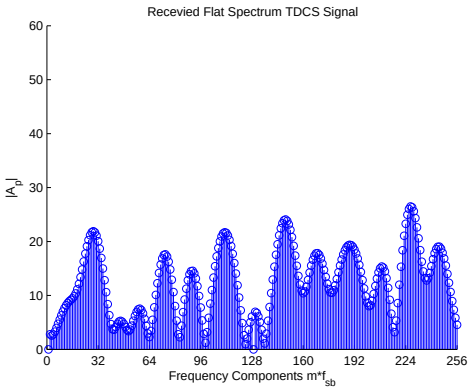

Figure 2.14: Received Un-encoded, Flat Spectrum TDCS Signal

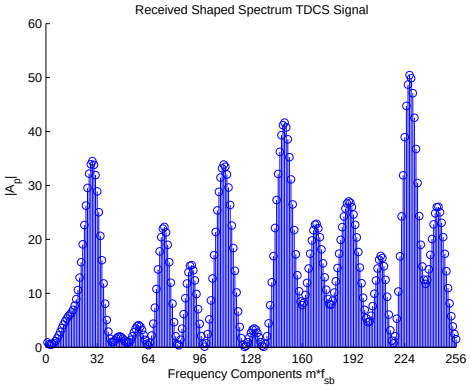

Figure 2.15: Received Spectrally Encoded, Shaped Spectrum TDCS Signal

are "filtered" by the channel, and instead concentrate signal energy in frequencies that are "amplified" by the channel. The result is seen in the received version of the spectrally encoded, shaped spectrum TDCS signal in Figure 2.15. This sequence of figures illustrates that the energy in the spectrally encoded, shaped spectrum TDCS signals is expected to be greater than that of the un-encoded, flat spectrum TDCS signals by an unspecified amount. The quantification of this relationship is deferred to the following chapter.

2.4.2 Hypothesis 2: Interference Avoidance. Intuitively, it would be expected that the multipath fading channel would create "valleys" in the interferer's

spectrum just as it does with the communication system. Therefore, the spectrally encoded, shaped spectrum TDCS signals are expected to exhibit some interference rejection. Additionally, if the same notching algorithm used in [6] is applied to the spectrally encoded TDCS signals to avoid a narrow band interferer through the fading channel, it is expected that the notched signals have better performance compared to the un-notched signals. However, since "valleys" may already exist in the spectrum, the improvement may not be as great as seen over the AWGN channel.

III. Analysis

In Chapter II the foundational principles and concepts for this research were presented. In this section, the TDCS concepts and principles of multipath fading channel analysis are combined to analyze the performance of a TDCS system in a FSSF multipath fading channel.

3.1 TDCS Complex Low-Pass Equivalent Model

The time domain representation of a baseband MPSK TDCS signal shown in (2.3) provides the basis for the TDCS analysis. However, recall that the analysis of the multipath fading channel uses the complex low-pass equivalent analytical model. The continuous-time, complex low-pass equivalent, analytical model of a transmitted TDCS symbol $s_{l,k}(t)$ in (3.1) is derived in Section A.3. In (3.1), l indicates the complex low-pass representation and k is in reference to the k^{th} of M data symbols. All parameters are identical to those described in Section 2.1.

$$s_{l,k}(t) = \sum_{p=-P}^{P-1} A_p e^{j(2\pi f_{sb} p t + \phi_p + \theta_k)} \quad t_o \le t \le t_o + T_{sb} \tag{3.1}$$

Assuming as before that the continuous-time signal is sampled at $2Pf_{sb}$ so that no aliasing occurs, then $N = 2P$. For the remainder of the analysis, it is also assumed that $f_{samp} = 2Pf_{sb}$. Using the same derivation as in Section A.3, (3.2) shows the discrete-time, complex low-pass representation of a TDCS symbol.

$$s_{l,k}[n] = \frac{1}{N} \sum_{p=-P}^{P-1} A_p e^{j\left(2\pi p \frac{n}{N} + \phi_p + \theta_k\right)} \quad 0 \le n \le N-1 \quad \text{where } N = 2P \tag{3.2}$$

Similar transformations are used to show the complex low-pass equivalent of the continuous- and discrete-frequency representations of the TDCS symbols are given in Equations (3.3) and (3.5) respectively.

$$S_{l,k}(f) = \sum_{p=-P}^{P-1} A_p \Big\{ \operatorname{sinc}\big[T_{sb}(f - p f_{sb})\big] e^{j\operatorname{sgn}(p)(\phi_p + \theta_k)} \Big\} \tag{3.3}$$

where:

$$\text{sgn}(p) = \begin{cases} 1 & \forall p > 0 \\ 0 & p = 0 \\ -1 & \forall p < 0 \end{cases} \tag{3.4}$$

$$S_{l,k}[m] = \begin{cases} A_m e^{+j(\phi_m + \theta_k)} & \forall m \in (0, P-1) \\ A_{m-N} e^{+j(\phi_{m-N} + \theta_k)} & \forall m \in (P, N-1) \end{cases} \tag{3.5}$$

Note one difference between equations in Chapter II and those presented above: the complex low-pass equivalent expressions allow for asymmetric spectra and therefore imaginary components in the symbols.

Next, the energy in the transmitted TDCS signal is reviewed. For a complex valued signal, it is commonly known that (3.6) and (3.7) give the energy over a single symbol duration, E_{sym}. Since this research uses BPSK signaling exclusively, $E_{sym} = E_b$.

$$E_{sym} = E_b \;=\; \int_0^{T_{sym}} |s(t)|^2 dt = \int_0^{T_{sym}} s(t)s^*(t)dt \tag{3.6}$$

and by Parseval's Relation [5, 141]:

$$E_b \;=\; \int_{-\infty}^{\infty} |S(f)|^2 dt = \int_{-\infty}^{\infty} S(f)S^*(f)dt \tag{3.7}$$

Using these relationships, the energy in the transmitted, complex low-pass, continuous-time TDCS signal is derived in Section A.4 with the following result:

$$E_b \;=\; T_{sym} \sum_{p=-P}^{P-1} A_p^2 \tag{3.8}$$

In the discrete-time and frequency domain, the energy relationships are:

$$E_b \;=\; \sum_{n=0}^{N-1} |s[n]|^2 = \sum_{n=0}^{N-1} s[n]s^*[n] \tag{3.9}$$

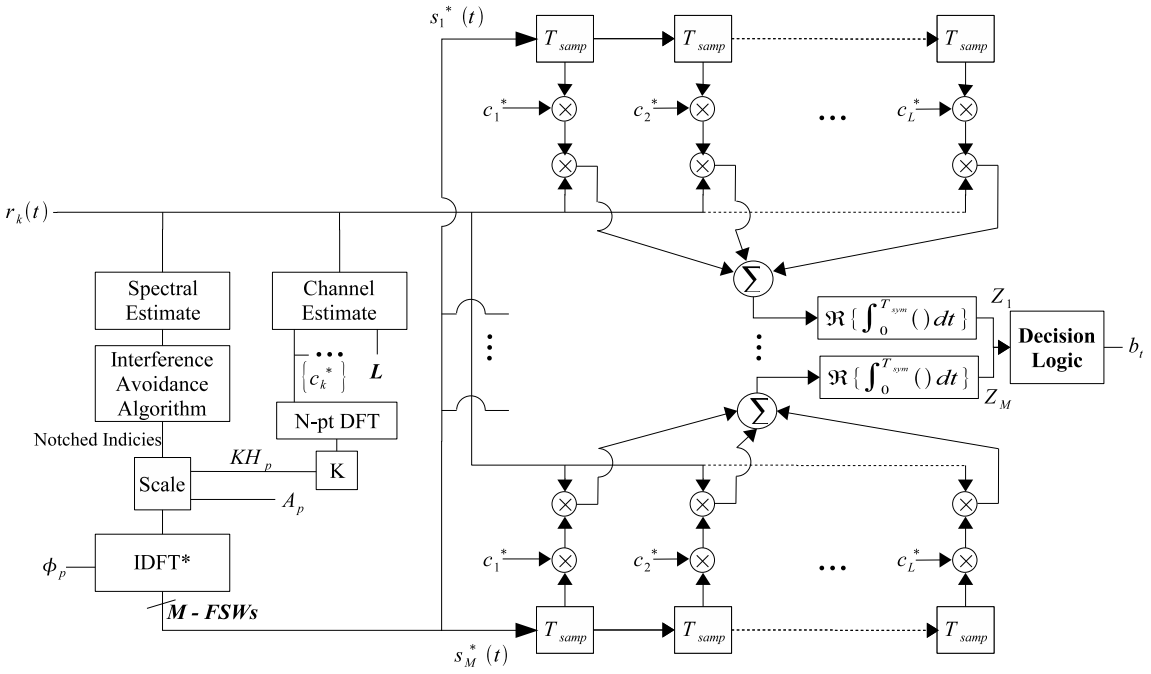

Figure 3.1: Notional TDCS RAKE Receiver

and again by Parseval's Relation:

$$E_b = \frac{1}{N}\sum_{k=0}^{N-1}|S[k]|^2 = \frac{1}{N}\sum_{k=0}^{N-1}S[k]S^*[k] \tag{3.10}$$

Using the frequency domain relationships in (3.10) and (3.5), the transmitted energy for a discrete-time, complex low-pass representation of a TDCS symbol is shown in (3.11).

$$E_b = \frac{1}{N}\sum_{k=-P}^{P-1}A_p^2 \tag{3.11}$$

3.2 RAKE Receiver Design Applied to the TDCS

As seen in Chapter II, to improve performance through a multipath fading channel, the communication system must incorporate diversity. Here, the RAKE receiver design is applied to a notional TDCS system as seen in Figure 3.1.

The function of the TDCS RAKE receiver is very similar to the original TDCS receiver shown in Figure 2.2. The RAKE receiver structure uses the L channel impulse response coefficients c_n to scale the delayed replicas of the FSWs. The sum of the delayed and scaled FSWs form the reference waveforms in the matched filters.

The components that allow spectral encoding are also added to the design shown in Figure 3.1. If spectral encoding is applied, the scaled channel transfer function magnitudes KH_p shape the spectrum of the FSWs. Otherwise, un-encoded, flat spectrum signals use equal amplitude frequency components A_p to construct the FSWs.

In this version of the TDCS receiver, the spectral estimation components simply serve to identify spectral components to be notched for interference avoidance if it is activated. As before, the notched spectral components are scaled to maintain equal energy signaling.

3.3 TDCS Signals in a Frequency-Selective Slowly-Fading (FSSF) Multipath Channel

To explain the power the TDCS system provides in mitigating multipath fading, the derivation of the received signal is presented next with the overall goal of determining the relationship between the spectral magnitudes of the TDCS signals A_p and KH_p and the energy contribution to the test statistic. Recall the transmitted, complex, low-pass representation of the k^{th} symbol, $s_{l,k}(t)$ from (3.1) and the multipath fading channel impulse response $h_l(t)$ from (2.26). To determine the complex low-pass representation of the received signal at the input of the TDCS RAKE receiver $r_{l,k}(t)$, the transmitted signal is convolved with the channel impulse response and combined with AWGN as in (3.12). In the derivation below, $\otimes$ is the convolution operator and $\tau_n = nT_{samp}$. Recall also that the convolution of any signal with a time-delayed Dirac

delta function is a delayed version of the original signal.

$$r_{l,k}(t) = s_{l,k}(t) \otimes \left[\sum_{n=1}^{L} c_n \delta(t - nT_{samp}) \right] + z_l(t) \tag{3.12}$$

$$= \sum_{n=1}^{L} c_n s_{l,k}(t - nT_{samp}) + z_l(t) \tag{3.13}$$

$$= \sum_{n=1}^{L} \sum_{p=-P}^{P-1} c_n A_p e^{j[2\pi f_{sb} p(t - nT_{samp}) + \phi_p + \theta_k]} + z_l(t) \tag{3.14}$$

substituting $c_n = \alpha_n e^{j\Theta_n}$:

$$r_{l,k}(t) = \sum_{n=1}^{L} \sum_{p=-P}^{P-1} \alpha_n A_p e^{j[2\pi f_{sb} p(t - nT_{samp}) + \phi_p + \theta_k + \Theta_n]} + z_l(t) \tag{3.15}$$

$$= v_{l,k}(t) + z_l(t) \tag{3.16}$$

where:

$$v_{l,k}(t) = \sum_{n=1}^{L} \sum_{p=-P}^{P-1} \alpha_n A_p e^{j[2\pi f_{sb} p(t - nT_{samp}) + \phi_p + \theta_k + \Theta_n]} \tag{3.17}$$

The signal component is distinguished from the noise component in $r_{l,k}(t)$ and is denoted $v_{l,k}(t)$. Recall that $v^*_{l,k}(t)$ is the reference waveform in the matched filters of the RAKE receiver. The expressions $r_{l,k}(t)$ and $v_{l,k}(t)$ from (3.16) and (3.17) are now substituted into the results of the previous development of the L-diversity RAKE receiver test statistic referenced from (2.44), yielding

$$Z_i = \mathrm{Re}\left\{ \int_0^{T_{sym}} r_{l,k}(t) v^*_{l,i}(t)\, dt \right\} \quad i = 1, 2 \tag{3.18}$$

$$= \mathrm{Re}\left\{ \int_0^{T_{sym}} v_{l,k}(t) v^*_{l,i}(t)\, dt + \int_0^{T_{sym}} z_l(t) v^*_{l,i}(t)\, dt \right\} \quad i = 1, 2 \tag{3.19}$$

The first term in (3.19) matches the form of (3.6) and is therefore the energy in the received signal. Therefore, the energy contribution in the test statistic is renamed V

and the test statistic equation is rewritten as

$$Z_i = \mathrm{Re}\left\{V + \int_0^{T_{sym}} z_l(t) v_{l,i}^*(t)\, dt\right\} \quad i = 1, 2 \tag{3.20}$$

Recalling that the performance of a matched filter demodulator is directly related to the SNR in the test statistic, it is clear that (3.20) forms the basis for the performance analysis of the TDCS RAKE receiver. At this point, the analysis diverges to evaluate the spectrally encoded, shaped spectrum TDCS signals and the un-encoded, flat spectrum TDCS signals separately.

3.4 Un-encoded, Flat Spectrum TDCS Signals

Consider the first of two cases for TDCS signals transmitted through the multipath fading channel. In this case, the TDCS spectrum is flat, i.e. all non-zero A_p are equal. Assuming also that the system uses equal energy signaling and that there are no DC or Nyquist frequency components in the TDCS FSWs, the relationship between the spectral magnitude components and the continuous-time representation of the transmitted bit energy E_b is shown in (3.21) starting from the relationship given in (3.8).

$$E_b = T_{sym} \sum_{p=-P}^{P-1} A_p^2 \tag{3.21}$$

If $N = 2P$ and $A_0 = A_{-P} = 0$, then the summation reduces and yields:

$$E_b = T_{sym} A_p^2 (N-2) \tag{3.22}$$

$$A_p = \begin{cases} \sqrt{\frac{E_b}{T_{sym}(N-2)}} & \forall p \in (-P, P-1), \quad p \neq 0, -P \\ 0 & p = 0, -P \end{cases} \tag{3.23}$$

Since all of the non-zero A_p are equal, the derivation of V takes place in the time domain.

Beginning with the definition of the reference waveform in the matched filter from (3.17), the derivation of V for flat spectrum TDCS signals follows.

$$V = \mathrm{Re}\left[\int_0^{T_{sym}} v_{l,k}(t)v_{l,i}^*(t)\,dt\right] \tag{3.24}$$

$$= \mathrm{Re}\left[\int_0^{T_{sym}} \left\{\sum_{n=1}^{L}\sum_{p=-P}^{P-1} \alpha_n A_p e^{j[2\pi f_{sb}p(t-nT_{samp})+\phi_p+\theta_k+\Theta_n]}\right\}\cdot \left\{\sum_{m=1}^{L}\sum_{q=-P}^{P-1} \alpha_m A_q e^{-j[2\pi f_{sb}q(t-mT_{samp})+\phi_q+\theta_i+\Theta_m]}\right\}\,dt\right] \tag{3.25}$$

$$= \mathrm{Re}\left[\int_0^{T_{sym}} \left(\sum_{n=1}^{L}\sum_{m=1}^{L}\sum_{p=-P}^{P}\sum_{q=-P}^{P} \{\alpha_n\alpha_m A_p A_q\}\cdot \left\{e^{j[2\pi f_{sb}p(t-nT_{samp})+\phi_p+\theta_k+\Theta_n]}e^{-j[2\pi f_{sb}q(t-mT_{samp})+\phi_q+\theta_i+\Theta_m]}\right\}\right)dt\right] \tag{3.26}$$

$$V = \mathrm{Re}\left[\int_0^{T_{sym}} \left(\sum_{n=1}^{L}\sum_{m=1}^{L}\sum_{p=-P}^{P}\sum_{q=-P}^{P} \{\alpha_n\alpha_m A_p A_q\}\cdot \left\{e^{j[2\pi f_{sb}(pt-qt+qmT_{samp}-pnT_{samp})+\phi_p-\phi_q+\theta_k-\theta_i+\Theta_n-\Theta_m]}\right\}\right)dt\right] \tag{3.27}$$

Continuing the analysis of the quadruple sum, assume that the test statistic of interest is being examined (i.e. $i = k$) and consider the following four cases of the quadruple sum in (3.27):

1. V_1: $p = q$, $m = n$
2. V_2: $p = q$, $m \neq n$
3. V_3: $p \neq q$, $m = n$
4. V_4: $p \neq q$, $m \neq n$

3.4.0.1 Case I, V_1: $p = q$, $m = n$. In this case, it is easily seen that for the test statistic of interest (i.e. $k = i$) all of the terms in the exponential cancel. The quadruple sum quickly simplifies to (3.28).

$$V_1 = \mathrm{Re}\left[\int_0^{T_{sym}} \sum_{n=1}^{L} \sum_{p=-P}^{P-1} \alpha_n^2 A_p^2 \, dt\right] \tag{3.28}$$

Since the expression in the integral is independent of time, the integration simplifies to T_{sym}. Recalling that all A_p are equal except when $p = 0, -P$ the summation over p can be replaced with $(N-2)A_p^2$.

$$V_1 = \mathrm{Re}\left[T_{sym} \sum_{p=-P}^{P-1} A_p^2 \sum_{n=1}^{L} \alpha_n^2\right] \tag{3.29}$$

$$= \mathrm{Re}\left[T_{sym}(N-2)A_p^2 \sum_{n=1}^{L} \alpha_n^2\right] \tag{3.30}$$

Now, the expression for A_p from (3.23) is substituted into the expression for V_1. Note that all terms in (3.31) are real, therefore (3.32) is the final result of the derivation of V_1.

$$V_1 = \mathrm{Re}\left[T_{sym}(N-2)\left(\sqrt{\frac{E_{sym}}{T_{sym}(N-2)}}\right)^2 \sum_{n=1}^{L} \alpha_n^2\right] \tag{3.31}$$

$$= E_{sym} \sum_{n=1}^{L} \alpha_n^2 \tag{3.32}$$

The expression for V_1 above is very similar to that of the signal to noise ratio developed for the RAKE demodulator from (2.47). By similarity, the statistics of V_1 can be described as a sum of L Chi-squared random variables with 2 DOF, having a mean energy of E_{sym}.

3.4.0.2 Case II, V_2: $p = q$, $m \neq n$. In this case, the quadruple sum is converted to a triple sum and the time dependence is removed. The second case of (3.27) is continued next.

$$V_2 = \mathrm{Re}\left[\int_0^{T_{sym}} \sum_{p=-P}^{P-1} A_p^2 \sum_{n=1}^{L} \sum_{\substack{m=1 \\ m\neq n}}^{L} \alpha_n \alpha_m e^{j[2\pi f_{sb} T_{samp}(m-n)+\Theta_n-\Theta_m]}\, dt\right] \quad (3.33)$$

Since there is no time dependence, the integral simplifies to T_{sym}. Recalling the relationship between $T_{samp} = 1/f_{samp} = 1/(2Pf_{sb})$, and separating the channel impulse response terms, V_2 is expressed as:

$$V_2 = \mathrm{Re}\left[T_{sym} \sum_{p=-P}^{P-1} A_p^2 \sum_{n=1}^{L} \sum_{\substack{m=1 \\ m\neq n}}^{L} \alpha_n \alpha_m e^{j(\Theta_n-\Theta_m)} e^{\frac{jp\pi}{P}(m-n)}\right] \quad (3.34)$$

The expression for A_p using (3.23) is now substituted into (3.34).

$$V_2 = \mathrm{Re}\left\{\left[T_{sym}\left(\sqrt{\frac{E_{sym}}{T_{sym}(N-2)}}\right)^2\right] \cdot \left[\sum_{\substack{p=-P+1 \\ P\neq 0}}^{P-1} \sum_{n=1}^{L} \sum_{\substack{m=1 \\ m\neq n}}^{L} \alpha_n \alpha_m e^{j(\Theta_n-\Theta_m)} e^{\frac{jp\pi}{P}(m-n)}\right]\right\} \quad (3.35)$$

Reverting to the previous notation: $c_n = \alpha_n e^{j\Theta_n}$

$$V_2 = \mathrm{Re}\left\{\left[\frac{E_{sym}}{(N-2)}\right] \sum_{\substack{p=-P+1 \\ p\neq 0}}^{P-1} \sum_{n=1}^{L} \sum_{\substack{m=1 \\ m\neq n}}^{L} e^{\frac{jp\pi}{P}(m-n)} \quad \underbrace{c_n c_m^*}_{\text{iid RVs}}\right\} \quad (3.36)$$

Noting that within (3.36), the random variables c_n and c_m^* are identically and independently distributed, it is assumed that the product $c_n c_m^*$ can be treated as a constant within the summation. The product is renamed $c_n c_m^* = \mathcal{C}$ and removed from

the summation as shown in (3.37).

$$V_2 \approx \mathrm{Re}\left\{ \left(\frac{E_{sym}}{(N-2)} \right) \boldsymbol{\mathcal{C}} \sum_{\substack{p=-P+1 \\ p\neq 0}}^{P-1} \sum_{n=1}^{L} \sum_{\substack{m=1 \\ m\neq n}}^{L} e^{\frac{jp\pi}{P}(m-n)} \right\} \tag{3.37}$$

The triple sum over the exponential term is considered for simplification next. Section A.5 derives the simplification of the triple summation over p, m, and n that results in (3.38).

$$\sum_{\substack{p=-P+1 \\ p\neq 0}}^{P-1} \sum_{n=1}^{L} \sum_{\substack{m=1 \\ m\neq n}}^{L} e^{\frac{jp\pi}{P}(m-n)} \approx -L(L-2) \tag{3.38}$$

The result from (3.38), is substituted into (3.37) yielding

$$V_2 \approx \mathrm{Re}\left\{ E_{sym} \left[\frac{-L(L-2)}{N-2} \right] \boldsymbol{\mathcal{C}} \right\} \tag{3.39}$$

$$\approx E_{sym} \left[\frac{-L(L-2)}{N-2} \right] \mathrm{Re}\left\{ \boldsymbol{\mathcal{C}} \right\} \tag{3.40}$$

To obtain the pdf of V_2, the distribution of $\mathrm{Re}\{\mathcal{C}\}$ must be determined. To simplify the analysis, it is assumed that the real part of the product $\mathrm{Re}\{\mathcal{C}\}$ =$\mathrm{Re}\{c_n c_m^*\}$ in (3.40) is approximately equal to the product of the magnitudes of the two independent, complex Gaussian random variables ($\alpha_n \alpha_m$). Then it can be shown that the distribution of V_2 is given by (3.41) (See Appendix A.6).

$$f_{V_2}(V_2) = \int_{-\infty}^{\infty} \frac{1}{|A||w|\sigma^4} \exp\left\{ w^2 + \left(\frac{V_2}{Aw} \right)^2 \right\} dw \tag{3.41}$$

where:

$$A = -E_{sym}\left(\frac{L(L-2)}{N-2} \right) \tag{3.42}$$

3.4.0.3 Case III and IV: $p \neq q$. This section demonstrates that regardless of the other factors, when $p \neq q$, the terms of the quadruple sum in (3.27) are zero. For the analysis, the case in which $m \neq n$ is considered since it is the most complicated case. After this derivation, it is easily inferred that the case in which $m = n$ also goes to zero. The next steps in the derivation are to simplify using $i = k$ and separate the terms with time dependence for the integration.

$$V_3 = \mathrm{Re}\left(\sum_{n=1}^{L} \sum_{\substack{m=1 \\ m\neq n}}^{L} \sum_{p=-P}^{P-1} \sum_{\substack{q=-P \\ q\neq p}}^{P-1} \left\{ \alpha_n \alpha_m A_p A_q e^{j[2\pi f_{sb} T_{samp}(mq-np)+\phi_p-\phi_q+\Theta_n-\Theta_m]} \right\} \cdot \left\{ \int_0^{T_{sym}} e^{j[2\pi f_{sb} t(p-q)]}\, dt \right\} \right) \tag{3.43}$$

Now consider the evaluation of the time integral alone and recall that $T_{sym} = 1/f_{sb}$.

$$\int_0^{T_{sym}} e^{j[2\pi f_{sb} t(p-q)]}\, dt = \frac{1}{j2\pi f_{sb}(p-q)} e^{j[2\pi f_{sb} t(p-q)]} \Big|_0^{T_{sym}} \tag{3.44}$$

$$= \frac{1}{j2\pi f_{sb}(p-q)} \left\{ e^{j[2\pi \frac{f_{sb}}{f_{sb}}(p-q)]} - e^{j0} \right\} \tag{3.45}$$

$$= \frac{1}{j2\pi f_{sb}(p-q)} (1-1) = 0 \qquad \forall p, q \quad \in \quad \mathcal{I} \tag{3.46}$$

Since p and q are integers, all terms in Cases III and IV are zero.

3.4.1 Un-encoded, Flat Spectrum TDCS Signal Analysis Summary. The primary result of this section is that the quadruple sum from (3.27) is simplified to two terms V_1 and V_2. These terms are simplified to the extent that the test statistic

output is restated in a much simpler form:

$$Z_i = V_1 + V_2 + \mathrm{Re}\left\{\int_0^{T_{sym}} v_{l,i}^*(t) z_l(t)\, dt\right\} \tag{3.47}$$

$$= E_{sym}\sum_{n=1}^{L}\alpha_n^2 + E_{sym}\left[\frac{-L(L-2)}{N-2}\right]\mathrm{Re}\{\boldsymbol{\mathcal{C}}\} + \mathrm{Re}\left\{\int_0^{T_{sym}} v_{l,i}^*(t) z_l(t)\, dt\right\} \tag{3.48}$$

Given the expression for the test statistic in (3.48), the received SNR for un-encoded, flat spectrum TDCS signals γ_f is given by (3.50).

$$\gamma_f = \frac{V_1 + V_2}{N_o} \tag{3.49}$$

$$\gamma_f = \frac{E_{sym}}{N_o}\left[\sum_{n=1}^{L}\alpha_n^2 - \left(\frac{L(L-2)}{N-2}\right)\mathrm{Re}\{\boldsymbol{\mathcal{C}}\}\right] \tag{3.50}$$

Recalling the technique for predicting performance through a multipath fading channel from Chapter II, the goal of this section is to determine the pdf of γ_f. The following equations illustrate the process for deriving pdf of γ_f using placeholders for the densities of V_1 and V_2. Since γ_f is simply the sum of V_1 and V_2, scaled by $1/N_o$, the distribution for γ_f is found using the relationships found in [7, 184]. As before, $\otimes$ is the convolution operator.

$$z = V_1 + V_2 \tag{3.51}$$

$$f_z(z) = f_{V_1}(V_1) \otimes f_{V_2}(V_2) \tag{3.52}$$

$$= \int_{-\infty}^{\infty} f_{V_1}(x) f_{V_2}(z-x)\, dx \tag{3.53}$$

The transformation to scale the sum in (3.53) is simply applied as [7, 131]:

$$\gamma_f = \frac{z}{N_o} \tag{3.54}$$

$$f_{\gamma_f}(\gamma_f) = N_o f_z\left(N_o \gamma_f\right) \tag{3.55}$$

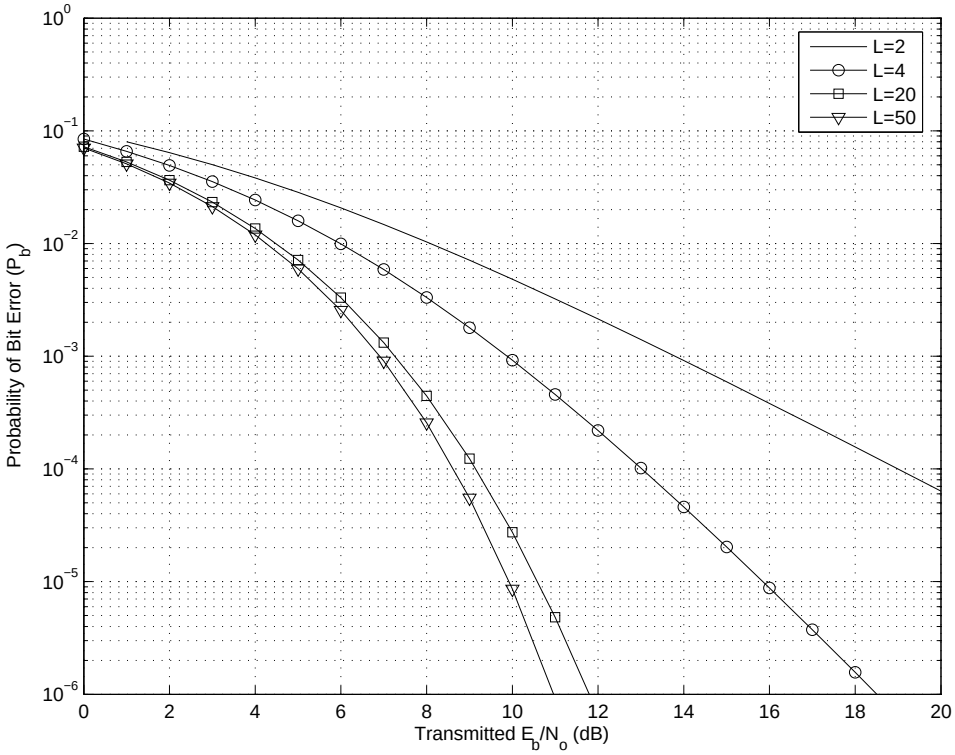

Figure 3.2: **Un-encoded, Flat Spectrum TDCS Signal Analytical Results.** This figure depicts the analytical predictions of P_b for un-encoded TDCS signals demodulated with an L-diversity TDCS RAKE receiver. A clear improvement in P_b is evident as the amount diversity in the receiver increases from $L = 2$ through $L = 50$.

No closed form solution for the distribution of γ_f was achieved. Therefore the analytical prediction of P_b is determined by numerically solving for $f_{\gamma_f}(\gamma_f)$, then computing the expected value of $Q(\sqrt{2\gamma_f})$ over the density function.

3.4.2 Un-encoded, Flat Spectrum TDCS Signal Analysis Results. The results of the numerical computation of P_b are shown in Figure 3.2. The computations assume $P = 1024$ and a range of L including 2, 4, 20 and 50. The analytical results in Figure 3.2 are computed using numerical integrations to transform the random variable pdfs and compute the expected value of the P_b equation. Recall also, that these predictions are not expected to be exact since they are based on the approximations

for V_1 and V_2 explained in the sections above. Therefore, these results should closely match the simulation results, but may not be exact.

3.5 Spectrally Encoded, Shaped Spectrum TDCS Signals

Chapter II introduced the concept of spectrally encoding TDCS signals using the magnitude of the channel transfer function as basis for the spectral shape of the TDCS FSWs. In this section, the strategy is explicitly described and analyzed. The hypothesis development in Section 2.4.1, demonstrated graphically the "filtering" effect of the FSSF channel. The power of a TDCS to improve performance in a FSSF is similar to the interference avoidance strategy. The TDCS is capable of constructing FSWs that avoid placing energy in the frequency spectrum where the channel "filters" out energy.

The P_b improvement strategy used in this research to overcome the "filtering" effects of the FSSF is to use the magnitude spectrum of the channel transfer function to spectrally encode the magnitude spectrum of the TDCS FSWs. Since it is assumed that the channel impulse response $h_l(\tau)$ can be perfectly estimated (c.f. Section 2.2.4), the computation of the transfer function $H_l(f)$ using the Fourier transform is assumed to be an exact representation of the channel. The spectrally encoded magnitudes of the TDCS FSWs are scaled to maintain equal-energy signaling as shown in (A.35) from Appendix A.2. Through the application of the Chebyshev Sum Inequality, the derivation in the appendix shows that TDCS signals with the same spectral shape as the channel transfer function pass more energy through the FSSF multipath channel than flat spectrum TDCS signals containing the same amount of energy. In this section, the quantitative analysis of the TDCS RAKE demodulator test statistic, beginning with (3.20) is presented for spectrally encoded, shaped spectrum TDCS signals. Since the spectral magnitudes A_p of the FSWs for the shaped TDCS signals are not all equal, the analysis takes place in the frequency domain.

To continue the quantitative analysis, the discrete-frequency representation of the received shaped spectrum TDCS signal $R_{l,k}[m]$ referenced from (A.38) follows.

$$R_{l,k}[m] = \begin{cases} KH_m^2 e^{+j(\phi_p+\theta_k)} & \text{if } m = p \quad \forall p \in (0, P-1) \\ KH_m^2 e^{-j(\phi_p+\theta_k)} & \text{if } m = N-1-p \quad \forall p \in (0, P-1) \\ 0 & \text{otherwise} \end{cases} \tag{3.56}$$

where:

$$K = \sqrt{\frac{E_{sym}N}{\sum_{p=-P}^{P-1} H_p^2}} \tag{3.57}$$

Using (3.11) and the results above, the energy in the received, shaped spectrum TDCS signals V_{shaped} is derived next.

$$V_{shaped} = \frac{1}{N}\sum_{p=-P}^{P-1} A_p^2 \tag{3.58}$$

$$= \frac{1}{N}\sum_{p=-P}^{P-1} (KH_m^2)^2 \tag{3.59}$$

$$= \frac{1}{N}\left(\sqrt{\frac{E_{sym}N}{\sum_{k=-P}^{P-1} H_k^2}}\right)^2 \sum_{p=-P}^{P-1} H_p^4 \tag{3.60}$$

$$= E_{sym}\frac{\sum_{p=-P}^{P-1} H_p^4}{\sum_{k=-P}^{P-1} H_k^2} \tag{3.61}$$

The expression for V_{shaped} from (3.61) is now substituted for V in the test statistic equation referenced from (3.20) as shown in 3.62.

$$Z_i = \text{Re}\left\{E_{sym}\frac{\sum_{p=-P}^{P-1} H_p^4}{\sum_{k=-P}^{P-1} H_k^2} + \int_0^{T_{sym}} v_{l,i}^*(t)z(t)\,dt\right\} \tag{3.62}$$

$$\tag{3.63}$$

While the individual pdfs for H_p^2 and H_p^4 can be derived (See Appendix A.7), each of the N H_p random variables are scaled sums of the same impulse response coefficients

$c_1, ..., c_L$. Therefore, these are not sums of independent random variables, and cannot be simplified without the joint density functions of all N H_p^2 and H_p^4.

3.5.1 Estimation of Spectrally Encoded, Shaped Spectrum Signal Energy Distribution. Since the joint densities of the sequences H_p^2 and H_p^4 are unknown, further development of the closed form analytical solution is not possible. Instead, Monte Carlo simulations and distribution parameter estimation methods are used to estimate the distribution of the ratio in (3.64).

$$\frac{\sum_{p=-P}^{P-1} H_p^4}{\sum_{p=-P}^{P-1} H_p^2} \tag{3.64}$$

Monte Carlo simulations of the random sequence c_n are the basis for the computations. From each L-length sequence of c_n, the resultant frequency domain terms H_p^2 and H_p^4 are computed using a zero-padded, N-point DFT ($N = 2P$). The summations of H_p^4 and H_p^2 are then computed and divided as in (3.64). The simulation terminates when the 95% confidence interval on the sample mean of the division converges to within 0.1% of the computed value (see Appendix A.8 for calculations). After the simulation converges, the data is run through `Matlab`® parameter estimation routines for several distributions. Based on visual inspection of the histograms, the Monte Carlo data is tested against the Gamma, Rayleigh, Log-Normal and Weibull distributions. Once the parameters for each of these four distributions are estimated by the `Matlab`® routines, they are compared to determine the distribution that most closely matches the simulation data. Quantile-quantile plots with linear regression models determine which distribution best fits the simulation data.

The quantile-quantile plot is a standard method for testing the distribution of data [3, 196]. The plot provides a visual comparison of the simulated data quantiles and the known quantiles of a given distribution. If the distributions are identical, the plot should yield a straight line. Therefore a linear regression model of the quantile-quantile plot and analysis of variance on the linear model provide a quantifiable

measure of the quality of the distribution match. Appendix A.9 contains a detailed description of the process used to develop the quantile-quantile plots, linear regression model and the coefficient of determination. The coefficient of determination R^2 is the ultimate measure of merit, with $R^2 = 1$ indicating a perfect distribution match.

3.5.2 Spectrally Encoded, Shaped Spectrum TDCS Signal Summary. Recall that finding the distribution of the division in (3.64) is only an interim step toward determining the performance of the spectrally encoded, shaped spectrum TDCS signals. Once the distribution is determined, the predicted P_b is estimated using the same technique illustrated in Chapter II. First, the pdf selected after the parameter matching process is scaled by the transmitted SNR E_{sym}/N_o to determine the pdf of the received SNR of the spectrally encoded, shaped spectrum TDCS signals γ_s. Then the probability of bit error for the shaped spectrum signals $P_{b,shaped}$ is the expected value of the P_b equation computed over the pdf of the shaped spectrum signals as shown in (3.66).

$$\gamma_s = \frac{E_{sym}}{N_o} \frac{\sum_{p=0}^{N-1} H_p^4}{\sum_{p=0}^{N-1} H_p^2} \tag{3.65}$$

$$P_{b,shaped} = \int_0^\infty Q\left(\sqrt{2\gamma_s}\right) p(\gamma_s) d\gamma_s \tag{3.66}$$

The probability of bit error is computed numerically since a closed form solution has not been found.

3.5.3 Spectrally Encoded, Shaped Spectrum TDCS Signal PDF Estimation Results. Parameter estimations, quantile-quantile plots, linear regression models and coefficients of determination are determined for $L = 2$, 4, 20 and 50 given $P = 1024$. In this section, the distribution test results are presented by order of increasing L. The results for each L contain quantile-quantile plots and R^2 values for each distribution comparison. The parameter values for the matched distribution are provided along with the 95% confidence intervals on each parameter.

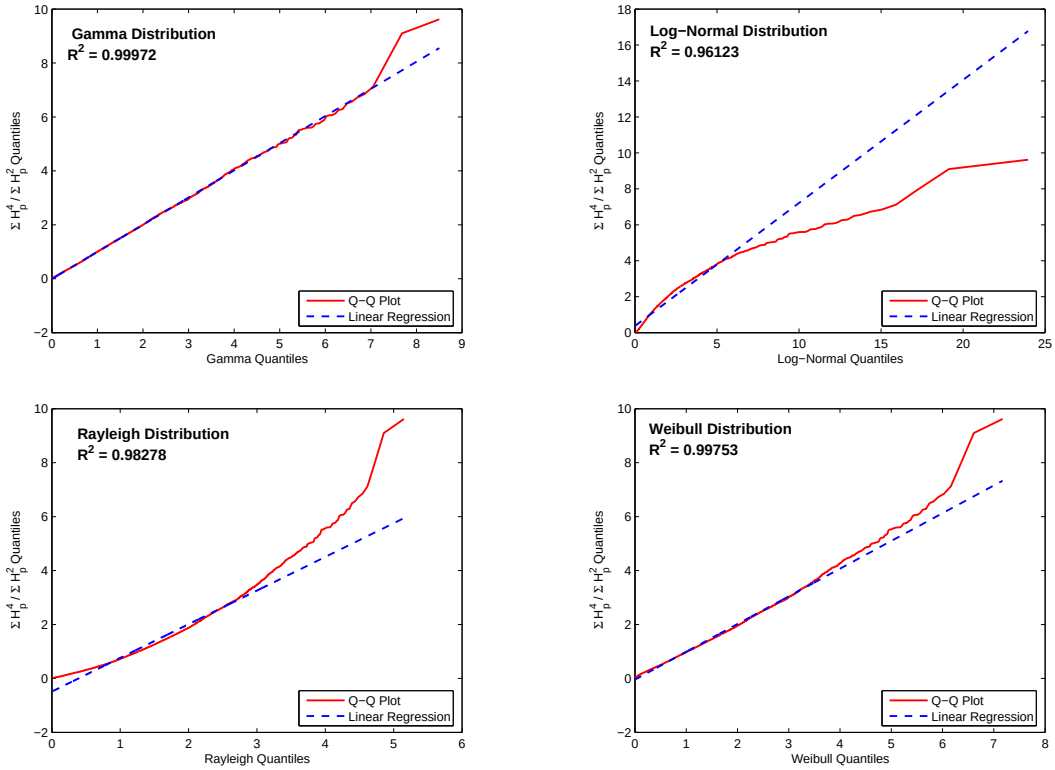

Figure 3.3: **Estimation of Distributions for $L = 2$.** These quantile-quantile plots and their associated R^2 values demonstrate that the Gamma distribution most closely matches the received energy for $L = 2$.

3.5.3.1 Spectrally Encoded Distribution Results: $L = 2$. In Figure 3.3, quantile-quantile plots are displayed for the four distributions mentioned in Section 3.5.1. The quantile-quantile plots and the coefficient of determination indicate that the Gamma distribution most closely matches the Monte Carlo simulation data. Table 3.1 contains the estimated parameters for the distribution with 95% confidence intervals and the coefficient of determination.

Table 3.1: Parameter Estimation for $L = 2$

Distribution	α **(95% CI)**	β **(95% CI)**	R^2
Gamma	1.9156 (1.867 - 1.9654)	0.6797 (0.67084 - 0.71135)	0.99972

3.5.3.2 Spectrally Encoded Distribution Results: $L = 4$. Figure 3.4 contains the comparison of the four proposed distributions to the Monte Carlo sim-

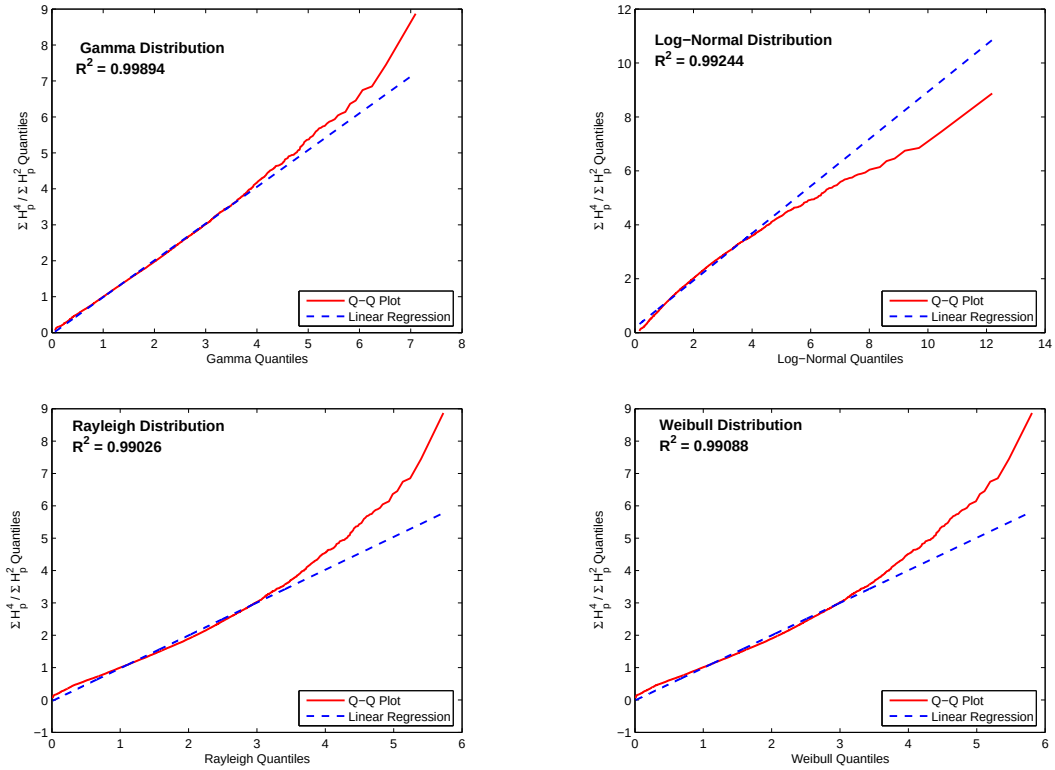

Figure 3.4: **Estimation of Distributions for $L = 4$.** These graphics illustrate the parameter matching quantile-quantile plots and R^2 values for $L = 4$. The Gamma distribution most closely matches the simulation data for $L = 4$.

ulations of the shaped spectrum energy for $L = 4$. For $L = 4$, the distribution estimation process indicates that the Gamma Distribution is closest to the simulated data distribution. Table 3.2 contains the estimated distribution parameters with 95% confidence intervals and the coefficient of determination.

Table 3.2: Parameter Estimation for $L = 4$

Distribution	α **(95% CI)**	β **(95% CI)**	R^2
Gamma	3.6046 (3.5102 - 3.7015)	0.44444 (0.43196 - 0.45728)	0.99894

3.5.3.3 Spectrally Encoded Distribution Results: $L = 20$. Figure 3.5 contains the comparison of the four proposed distributions to the simulations of the shaped spectrum energy for $L = 20$. The quantile-quantile plots and coefficients of determination indicate that the best matched distribution for $L = 20$ is the Log-

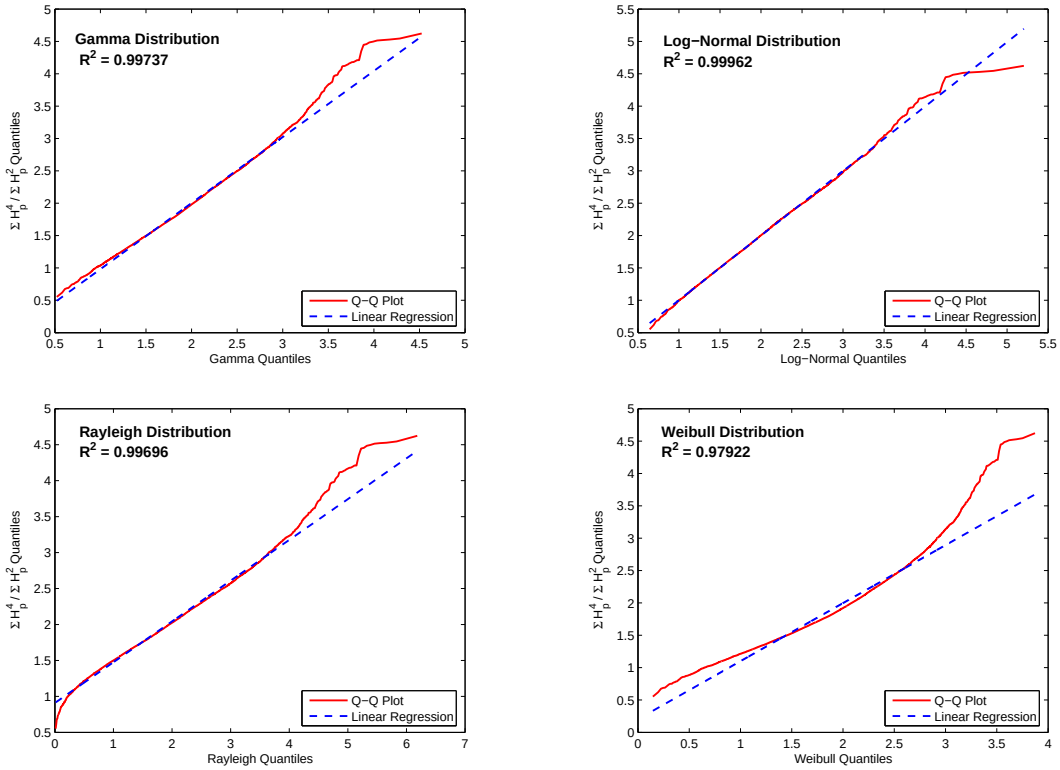

Figure 3.5: **Estimation of Distributions for $L = 20$.** These quantile-quantile plots illustrate the parameter matching process. The R^2 value indicates the Log-Normal distribution is closest to the simulated data distribution.

Normal Distribution. Table 3.3 contains the estimated mean and standard deviation with 95% confidence intervals and the coefficient of determination.

Table 3.3: Parameter Estimation for $L = 20$

Distribution	μ **(95% CI)**	σ **(95% CI)**	R^2
Log-Normal	0.60384 (0.59857 - 0.60911)	0.26877 (0.26509 - 0.27254)	0.99962

3.5.3.4 Spectrally Encoded Distribution Results: $L = 50$. The prediction of the signal energy distribution for $L = 50$ is shown in Figure 3.6. From the quantile-quantile plots and coefficients of determination, the best matched distribution for the $L = 50$ simulations is clearly the Log-Normal Distribution. Table 3.4 contains the estimated mean and standard deviation with 95% confidence intervals and the coefficient of determination.

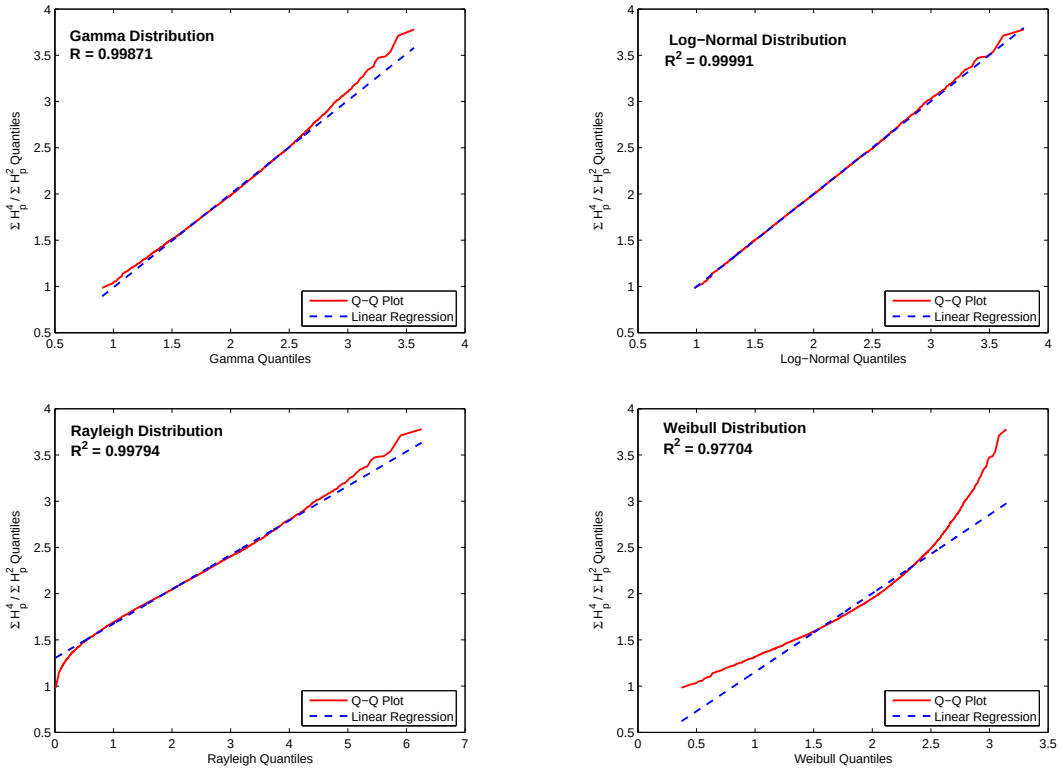

Figure 3.6: **Estimation of Distributions for $L = 50$.** The quantile-quantile plots and R^2 values indicate that Log-Normal distribution is closest to the simulated data.

Table 3.4: Parameter Estimation for $L = 50$

Distribution	μ **(95% CI)**	σ **(95% CI)**	R^2
Log-Normal	0.6572 (0.6538 - 0.66061)	0.17372 (0.17134 - 0.17616)	0.99991

3.5.4 Spectrally Encoded, Shaped Spectrum Analysis P_b Results. Using the estimated distributions for each level of L, the predicted P_b for the spectrally encoded, shaped spectrum signals is computed numerically. The overall results are shown in Figure 3.7. Recall that these predictions are based on estimated signal energy distributions. The R^2 values from the parameter estimation results indicate that the distributions are very closely matched, therefore it is expected that these results should closely match the simulation results.

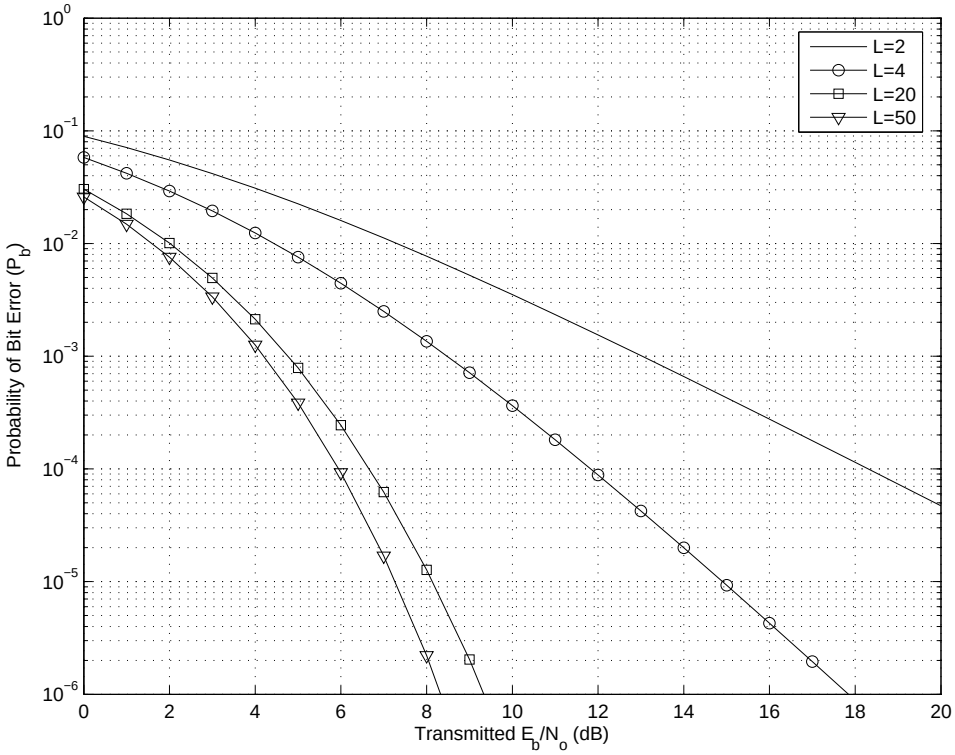

Figure 3.7: **Spectrally Encoded, Shaped Spectrum TDCS Signal Analytical Results.** This figure depicts the analytical predictions of P_b for spectrally encoded TDCS signals demodulated with an L-diversity TDCS RAKE receiver. These results also show a clear improvement in P_b as the amount diversity in the receiver increases from $L = 2$ through $L = 50$.

3.6 Comparison of Un-encoded and Spectrally Encoded Analytical Results

Observing the analytical P_b curves independently for the un-encoded, flat spectrum and spectrally encoded, shaped spectrum TDCS signals clearly demonstrates the benefit of increasing diversity. However, to see the benefits of spectral encoding, the results are compared for each level of L. In Figures 3.8 and 3.9, each curve compares the analytically predicted P_b for both the spectrally encoded, shaped spectrum signals and the un-encoded, flat spectrum signals for each level of L independently. In each case, the P_b for the spectrally encoded signals is lower (better) than the un-encoded P_b. These curves provide the basis for the comparison of the analytical and simulation

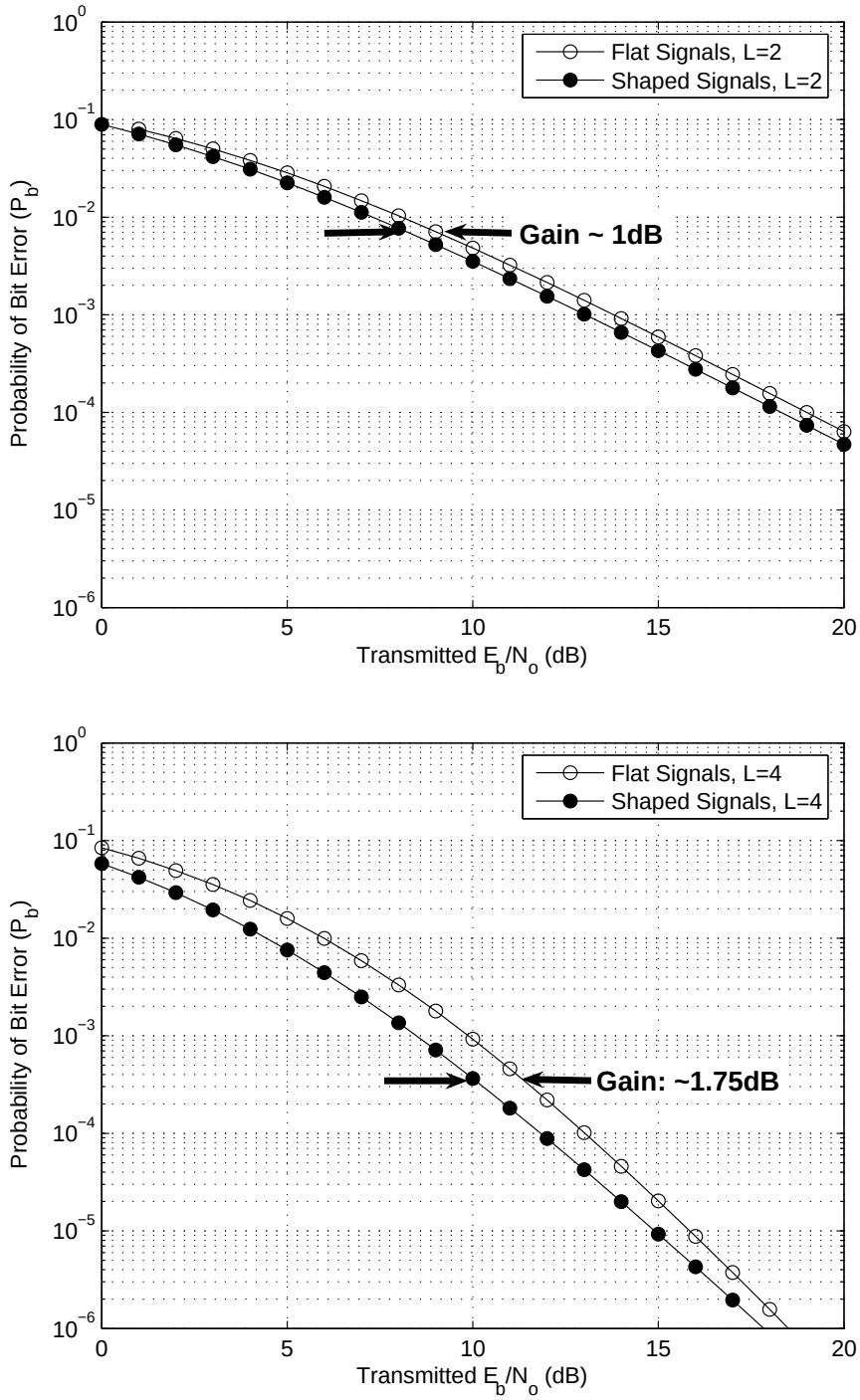

Figure 3.8: **Analytical P_b Comparison for Spectrally Encoded and Unencoded Signals, $L = 2, 4$.** These figures demonstrate the benefit of spectral encoding applied to the RAKE receiver at equivalent diversities L.

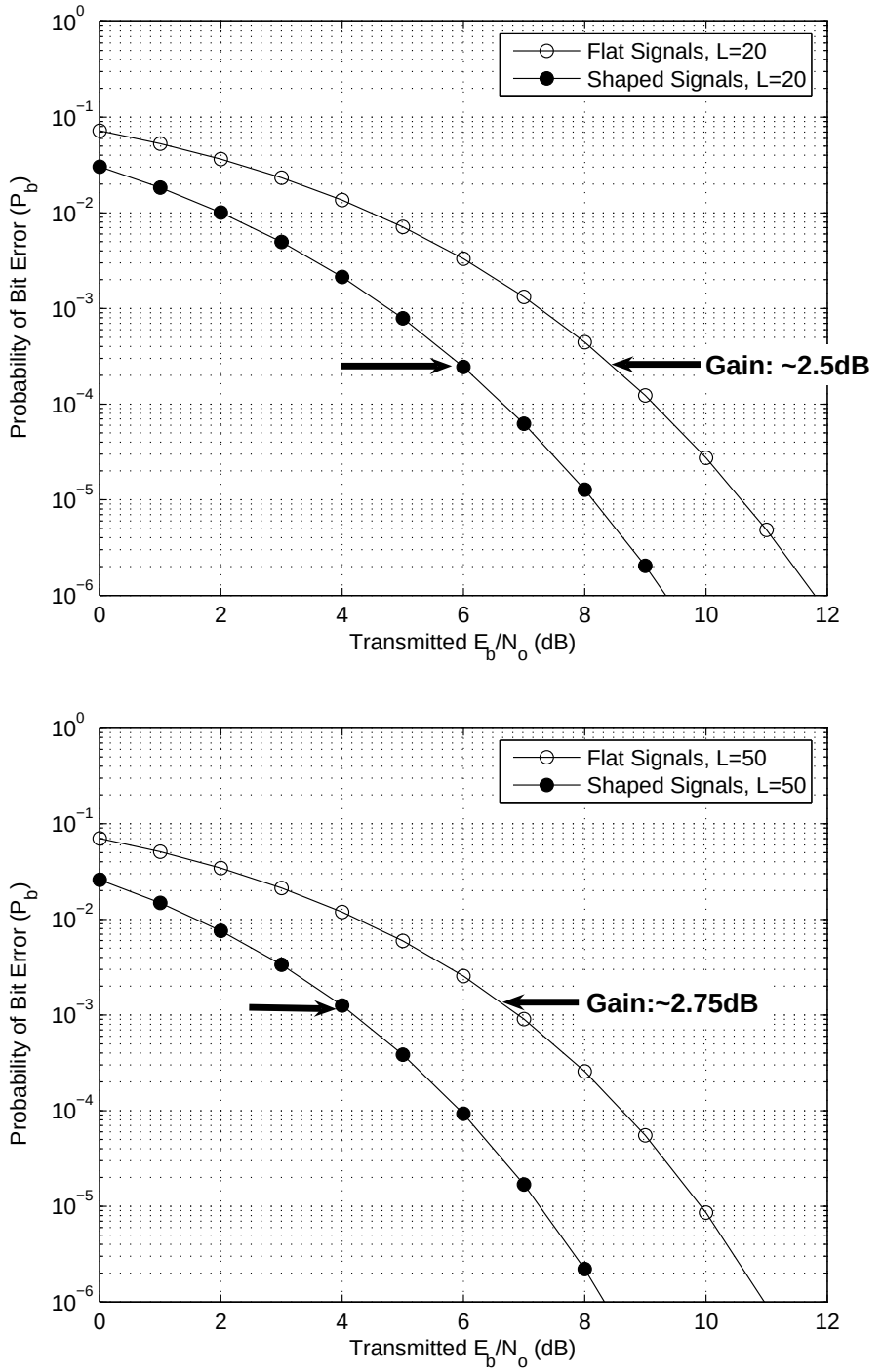

Figure 3.9: **Analytical P_b Comparison for Spectrally Encoded and Unencoded Signals, $L = 20, 50$.** These figures demonstrate the benefit of spectral encoding applied to the RAKE receiver at equivalent diversities L.

results. It is useful at this point to define the term gain G to provide a comparison of the transmitted E_b/N_o required to achieve a given probability of bit error, λ. If E_f/N_o is required to achieve a P_b of λ for the un-encoded, flat spectrum signals, and E_{sh}/N_o is required to achieve the same P_b of λ for the spectrally encoded, shaped spectrum signals, then gain G is defined in (3.67). The gain G is only determined for signals with equivalent diversities L. In Figures 3.8 and 3.9, the gains are estimated by graphically measuring the plot.

$$G(\text{dB}) = \frac{E_f}{N_o}(\text{dB}) - \frac{E_{sh}}{N_o}(\text{dB}) \tag{3.67}$$

This concludes the analysis of the spectrally encoded and un-encoded TDCS signals through the FSSF multipath channel. Next the analysis to determine the P_b of spectrally encoded, shaped spectrum signals is determined in the presence of an interferer.

3.7 Interference Avoidance

The second goal of this research is to evaluate the interference avoidance capability of spectrally encoded signals. Chapter II introduced the interference avoidance capability of the TDCS with the basic result that the spectral notching algorithm can remove interference energy from the test statistic by shifting the spectral distribution of energy in the TDCS FSWs. Additionally, the literature search revealed a method for predicting the P_b for notched and un-notched TDCS signals. Un-notched signals consider the average power in the interference signal P_i', compute the full interference PSD N_i' and add it to the noise PSD N_o to compute $P_{b,un-notched}$ as in (3.68).

$$P_{b,un-notched} = Q\left(\sqrt{\frac{2E_b}{N_o + N_i'}}\right) \tag{3.68}$$

where:

$$N_i' = \frac{P_i'}{2W_{BB}} = \frac{J_i'}{T_{sym}} \frac{1}{2Pf_{sb}} \tag{3.69}$$

$$= \frac{J_i'}{2P} \tag{3.70}$$

The total energy in the interferer J_i' is calculated using (2.9). Notched signal P_b is predicted using the interferer's power outside of the spectral notch P_i to compute the notched interferer's PSD N_i.

$$P_{b,notched} = Q\left(\sqrt{\frac{2E_b}{N_o + N_i}}\right) \tag{3.71}$$

where:

$$N_i = \frac{P_i}{2W_{BB}} = \frac{J_i}{T_{sym}} \frac{1}{2Pf_{sb}} \tag{3.72}$$

$$= \frac{J_i}{2P} \tag{3.73}$$

The expression for the energy in the notched interference spectrum J_i is given by (2.10).

Because the FSSF multipath channel affects both the shape of the spectrally encoded signals and the effect of the notching algorithm, this section considers two cases of interference avoidance. In the first situation, the interferer is close enough to the TDCS receiver that the interferer does not experience multipath fading. This scenario demonstrates the effects of spectral encoding on interference avoidance. The second situation distances the interference source from the TDCS receiver such that the interfering signal experiences multipath fading. This situation demonstrates the effect of the channel on the notching algorithm.

3.7.1 Interference Avoidance I: No Multipath on Interference Channel. This section presents an analysis of the situation in which the TDCS transmitter/receiver

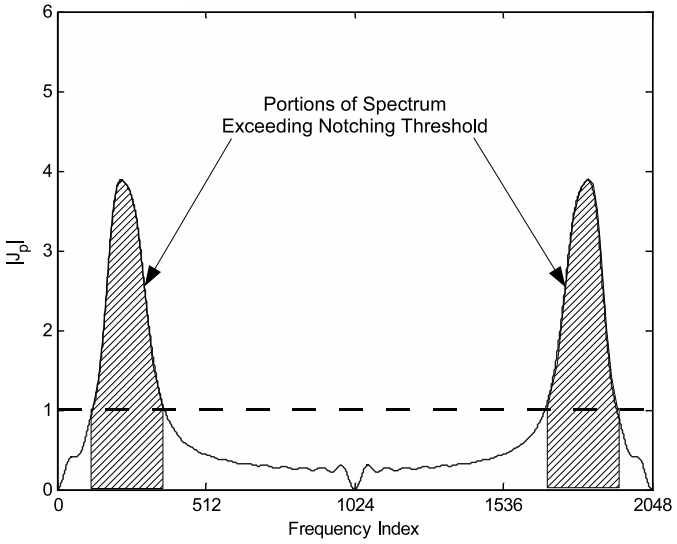

Figure 3.10: **Conceptual Transmitted Interference Spectrum.** This figure demonstrates the effect of the notching algorithm when no multipath fading occurs on the interference channel.

pair traverses a FSSF multipath channel, but the interferer passes through an AWGN only channel. This situation represents the scenario in which the interference source is located in close proximity to the TDCS receiver. This case is more likely for high interferer power to signal power ratios J/S, since the interferer may have to be much closer to the receiver to achieve the higher power ratio. Since the spectral shape of the interferer is not changed by the interference channel, the notching algorithm performs as discussed in the previous section.

However, recall that the TDCS signals traverse a multipath fading channel and are spectrally encoded with the shape of the channel transfer function. The spectral shaping should "filter" the interference source at the receiver. The precise analytical prediction of this effect and the resulting P_b are unknown at this point, so graphical illustrations are presented to provide intuitive analysis. Figure 3.10 depicts the transmitted magnitude spectrum of a narrow band interference source. The shaded area is the portion of the spectrum notched out by the interference avoidance algorithm. The figure demonstrates that the notching algorithm performs as predicted

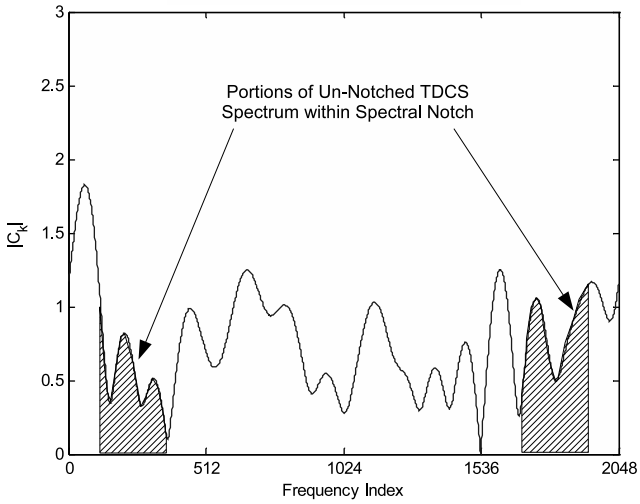

Figure 3.11: **Un-notched, Spectrally Encoded, Shaped Spectrum Signal, Scenario I.** This demonstrates the "filtering" effect created by the spectrally encoded, shaped spectrum TDCS signal. The shaded areas indicate areas of peak power for the interference source, that would be notched by the interference avoidance algorithm.

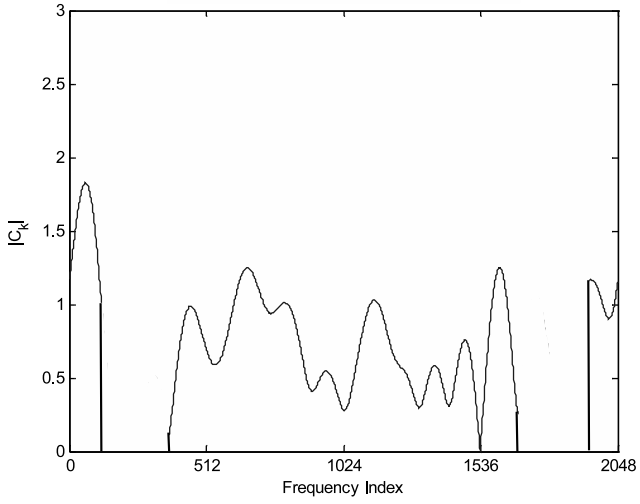

Figure 3.12: **Notched, Spectrally Encoded, Shaped Spectrum Signal, Scenario I.** This figure demonstrates that in addition to notching, the spectral shape of the spectrally encoded TDCS signal has a "filtering" effect on the interference source.

when the interference channel is AWGN only, attenuating the interferer's energy in the receiver test statistic according to the relationship in (2.10). However this is not the only effect to be considered. The spectral shape of the encoded TDCS signals also affects the amount of interference energy in the test statistic.

To illustrate this effect, Figure 3.11 represents the magnitude spectrum of a spectrally encoded TDCS signal after being shaped by a typical FSSF multipath channel transfer function. In this example, the diversity in the channel $L = 20$. Even when un-notched by the interference avoidance algorithm, the spectrally shaped TDCS signals have a "filtering" effect. The spectral notches in the TDCS signal spectrum should decrease the interferer's energy present in the test statistic although no notching is applied. Therefore, the simulated P_b for the un-notched, spectrally encoded, shaped spectrum TDCS signals is predicted to be slightly less (better) than the analytical results.

The corresponding magnitude spectrum of a spectrally encoded TDCS signal after notching, is shown in Figure 3.12. As stated above, the notching algorithm removes the analytically predicted amount of interference energy. However, the figure also demonstrates that the shape of the TDCS spectrum is also likely to remove additional interference energy. Therefore, the simulated P_b for the notched, spectrally encoded, shaped spectrum TDCS signals is predicted to be slightly less (better) than the analytical results.

To sum up the first scenario, the analytically predicted results using (3.71) and (3.68) are predicted to be upper bounds for the simulated results for the notched and un-notched spectrally encoded signals respectively.

3.7.2 Interference Avoidance II: Independent Multipath Channels. This case represents the scenario in which the interference source is not located in the same proximity as the transmitter. In this situation, the multipath fading channel impulse response from the interferer appears different from the impulse response coming from the TDCS transmitter when received at the TDCS receiver. Therefore, it is assumed

that the interferer and the TDCS transmitter traverse independent channels before arriving at the TDCS receiver.

As stated in the previous description of the TDCS interference avoidance capability, the TDCS samples the received spectrum and notches out frequency components exceeding the threshold. In this scenario, the TDCS receiver is estimating the spectrum of the interference source after it has passed through the FSSF multipath channel. The interference channel will distort the spectral magnitudes of the interferer, therefore the TDCS notching algorithm will not perform as previously predicted. Since the FSSF multipath channel is not deterministic, the channel may present either a "filter" or "amplification" in the location of the jammer's spectral magnitude peaks. If the same narrow band interferer shown in Figure 3.10 is transmitted through an independent channel with the transfer function in Figure 3.13, the resulting received interference spectrum is shown in Figure 3.14. From this example, it is apparent that the number of notched components will change due to the distortion of the interference spectrum. This example illustrates that the number of notched components may be either increased and/or decreased due to either the amplification or filtering effects of the multipath channel. Additionally, it is apparent that the interferer magnitudes change. However, these graphics are one representation of a stochastic channel. Since it is assumed that on average, the channel passes through 100% of the energy transmitted, it is predicted that on average the notching will perform as previously described.

The combined effect of the notching algorithm and spectral shaping when the communications and interference channels are independent is shown in Figures 3.16 and 3.15. Since the communications channel is independent, the TDCS signal shape is distinct from the interference distortion. Using the previously discussed received interference spectrum shown in Figure 3.14, the frequency components identified for notching (the interferer's peak power spectra) are shaded in Figure 3.15. In this example, the shaded areas within Figure 3.15 happen to fall within areas that have been "filtered" by the spectral shaping. However, depending on the instantiation of

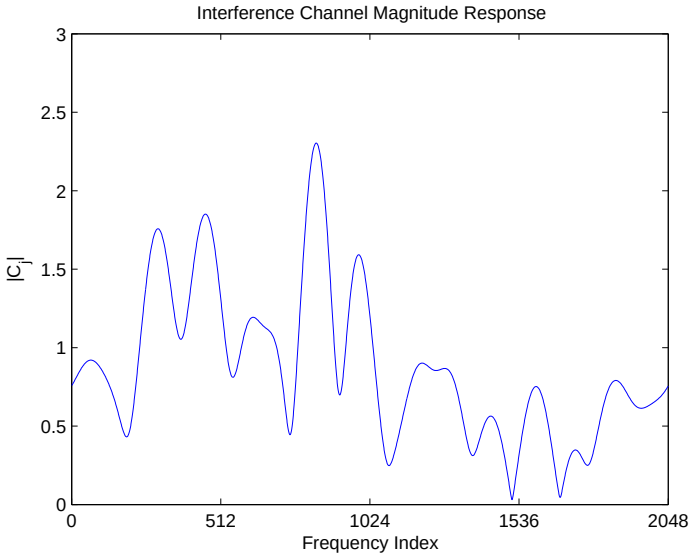

Figure 3.13: **Conceptual Interferer Channel Response.** This is the magnitude spectrum of a typical FSSF multipath channel transfer function with $L = 20$.

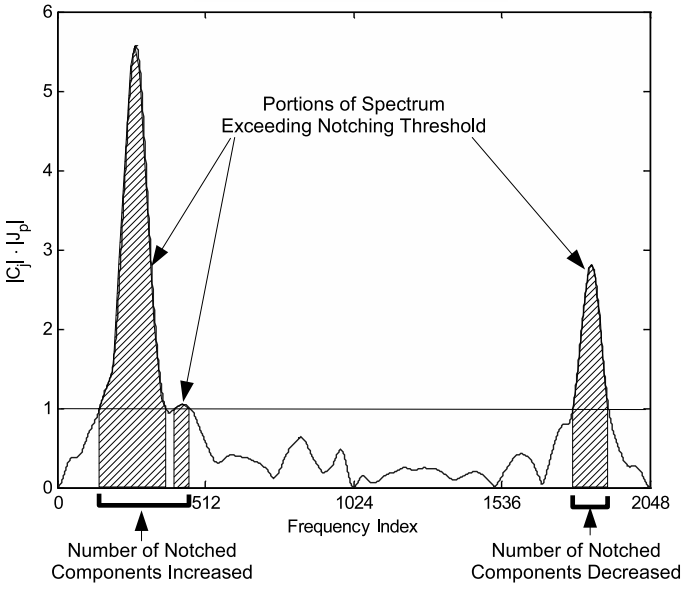

Figure 3.14: **Conceptual Received Interference Spectrum.** After being transmitted through the FSSF multipath fading channel, the interference spectrum is distorted. The shaded areas indicate the portions identified for notching by the interference avoidance algorithm.

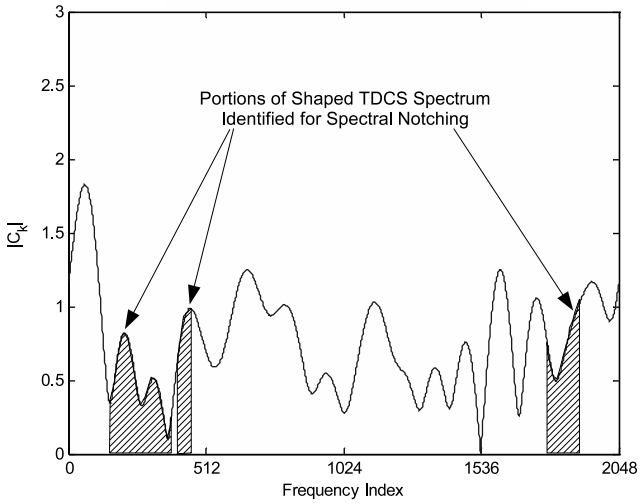

Figure 3.15: **Un-Notched, Spectrally Encoded, Shaped Spectrum Signal, Scenario II.** The shape of this spectrally encoded TDCS signal is shaped by a FSSF multipath channel that is independent of the interference channel. The shaded areas indicate the frequencies identified for notching after receiving the distorted interference spectrum. This figure demonstrates the "filtering" and "amplifying" effects of spectral encoding that is independent of the interference distortion.

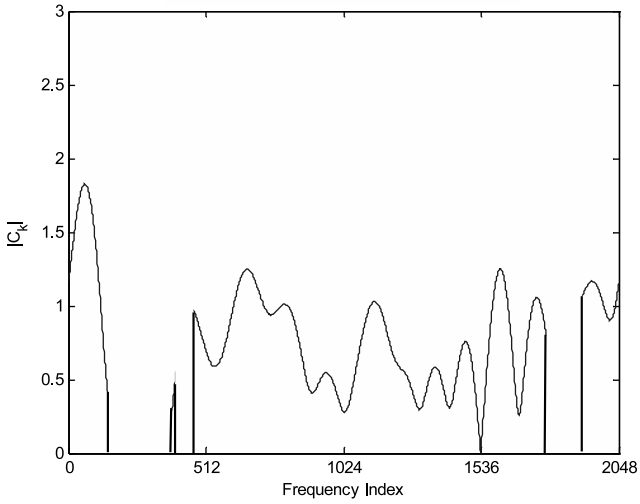

Figure 3.16: **Notched, Spectrally Encoded, Shaped Spectrum Signal, Scenario II.** The magnitude spectrum of this notched, spectrally encoded TDCS signal displays the frequency components remaining after notching the independently distorted interference spectrum.

the interference and communication channels, it is equally likely that the interferer's peak power spectra occur in bands that are "amplified" due to the spectral shaping. Again, since it is assumed that on average, the channel passes through 100% of the energy transmitted, and since the majority of frequency spectrum falls below a magnitude of 1, it is predicted that the un-notched, spectrally encoded, shaped spectrum TDCS signals will have an overall "filtering" effect. Therefore the simulated P_b for the un-notched, spectrally encoded TDCS signals is predicted to be better (lower) than the analytical prediction.

The TDCS magnitude spectrum in Figure 3.16 demonstrates that even after notching, the spectrally encoded TDCS signals will likely yield an additional "filtering" effect on the remaining interference energy. Therefore the simulated P_b for the notched, spectrally encoded TDCS signals is predicted to be better (lower) than the analytical prediction.

To sum up the second scenario, the analytical results are predicted to be upper and lower bounds of the simulation results. Specifically, the un-notched analytical results are predicted to be an upper bound, and the notched analytical results are predicted to be a lower bound.

3.7.3 Interference Avoidance: Interferer Description. For both interference avoidance cases, the magnitude spectrum presented in [6, pg4-4] is used to simulate a narrow band interferer. The shape of the interference source's magnitude spectrum is shown in Figure 3.17. For reference, the spectral magnitudes are included in Section A.10. This shape is interpolated to match the number of frequency components used in this research using the `Matlab`® `interpft` function. Additionally, the same notching algorithm discussed in Section 2.1.1 is used to compare the un-notched and notched signals. Where the interferer spectral magnitudes exceed the manually set threshold of 1, the spectral components A_p in the spectrally encoded, shaped spectrum TDCS signals are notched. This results in a theoretical reduction of 11.8dB in the interferer's energy in the TDCS receiver [6, 4-4].

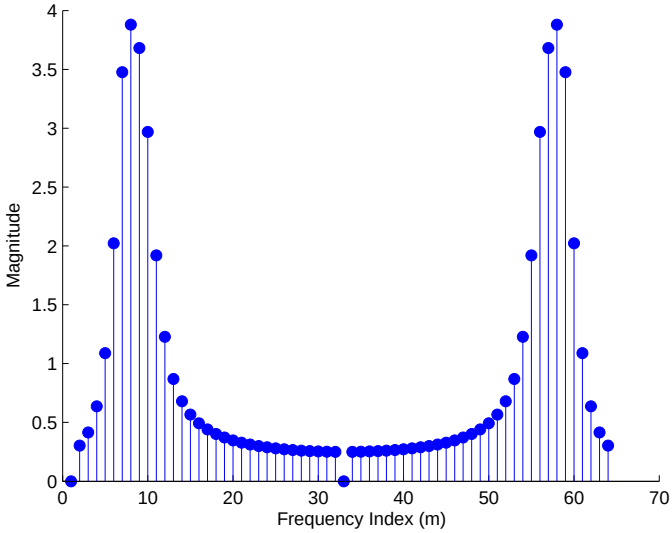

Figure 3.17: Magnitude Spectrum of Conceptual Interference Source

3.7.4 Interference Avoidance: Analytical Results. Figures 3.18 and 3.19 contain the analytical predictions of the interference avoidance capability for the spectrally encoded, shaped spectrum TDCS signals against the narrow band interferer described in Section 3.7.3. The un-notched interference PSD N_i' is computed using an average power that is 64 times the TDCS transmitter average power. The notched interference PSD N_i is computed using an average power that is 11.8dB lower than the un-notched power based on the effect of the manually set notching threshold. The P_b for the notched and un-notched signals is numerically computed by solving for the expected value of (3.71) and (3.68) over the shaped spectrum TDCS signal energy pdfs described in Section 3.5.3. Each curve compares the analytically predicted P_b for both the notched and un-notched signals for each level of L independently. As mentioned in the sections above, these curves are not exact predictors of performance since the effects of multipath fading on the interferer and the interference avoidance algorithm have not been quantified. Therefore, these curves are the predicted bounding cases for the simulation results.

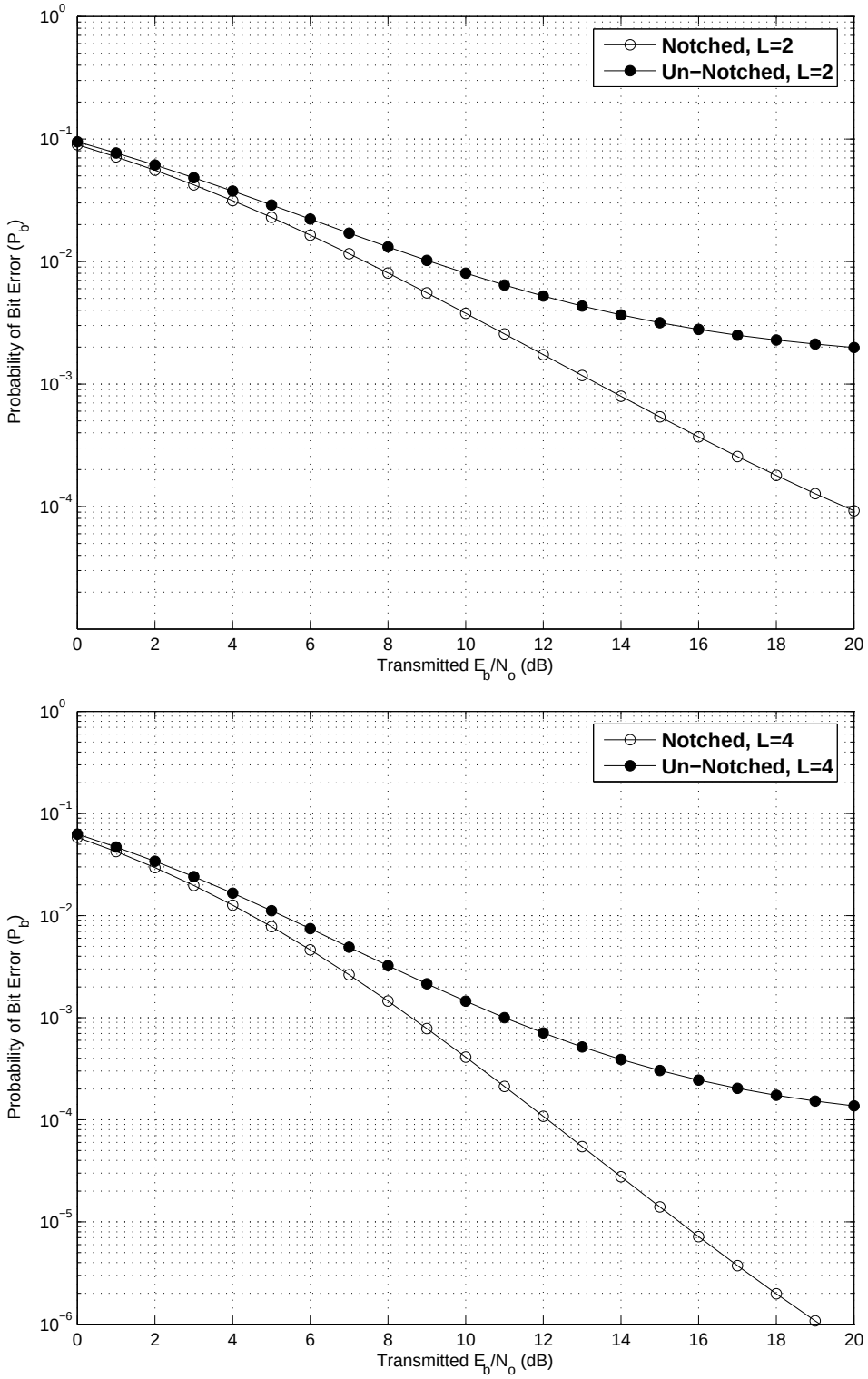

Figure 3.18: **Notched vs Un-notched Analytical Results, $L = 2, 4$.** These figures demonstrate the predicted interference avoidance capability of the notching algorithm applied to spectrally encoded, shaped spectrum TDCS signals using an L-diversity RAKE receiver. For these plots, $J/S = 64$ and the notching algorithm attenuates average interferer power by 11.8dB

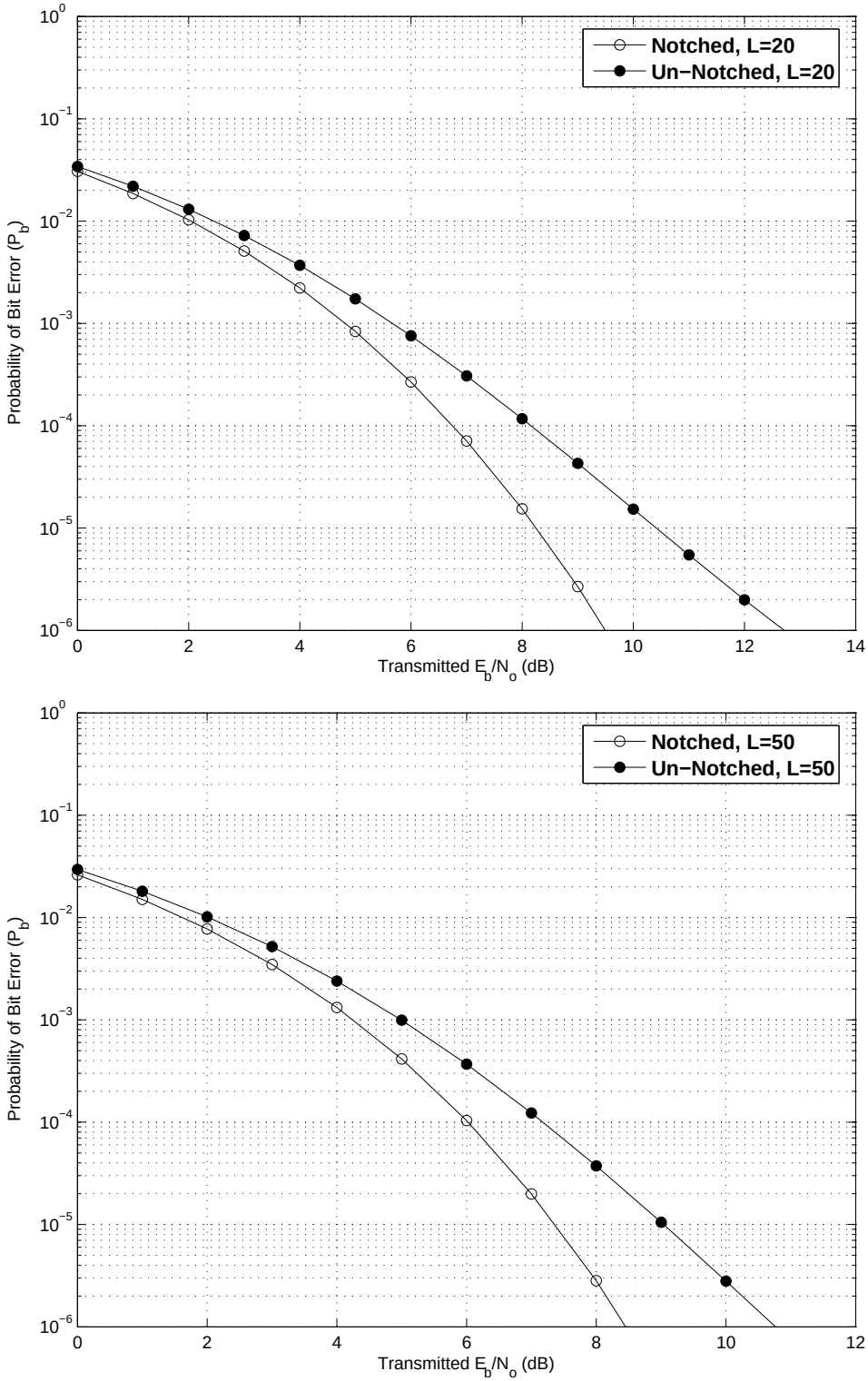

Figure 3.19: **Notched vs Un-notched Analytical Results, $L = 20, 50$.** These figures demonstrate the predicted interference avoidance capability of the notching algorithm applied to spectrally encoded, shaped spectrum TDCS signals using an L-diversity RAKE receiver. For these plots, $J/S = 64$ and the notching algorithm attenuates average interferer power by 11.8dB

3.8 Summary

In this chapter, the analysis of the TDCS in a FSSF multipath channel was presented. The results of the first portion of the analysis are the predicted P_b for spectrally encoded, shaped spectrum and un-encoded, flat spectrum TDCS signals in the FSSF channel. The second section of the analysis qualitatively predicts the interference avoidance capabilities of the spectrally encoded, shaped spectrum TDCS signals with and without notching. Two scenarios for interference avoidance were presented: the case in which the interferer traverses an independent FSSF multipath channel, and the case in which the interferer traverses an AWGN only channel.

IV. Simulation Methodology

Chapter III provides the mathematical analysis and associated results supporting the two goals of this research. This chapter describes the simulation methodology used to gather the results that verify the analysis. The system design is discussed first, followed by the design of experiments.

4.1 System Definition

This research simulates the system under test shown in Figure 4.1. The TDCS transmitter, L-diversity TDCS RAKE receiver, interference source, independent communications and interference channels, and AWGN source are all within the system boundary. The TDCS transmitter/RAKE receiver pair are modeled as described in Figures 2.1 and 3.1. The communications channel is modeled as a FSSF multipath channel as depicted in Figure 2.5. The interference channel is either characterized as a FSSF multipath channel or a straight pass through. The interference source has the spectral shape given by Figure 3.17. The AWGN source has a one-sided power spectral density of N_o.

4.1.1 System Services. Quite simply, the service provided by the system under test is symbol detection and estimation. The two possible outcomes of the service are either:

1. Symbol correctly detected and estimated

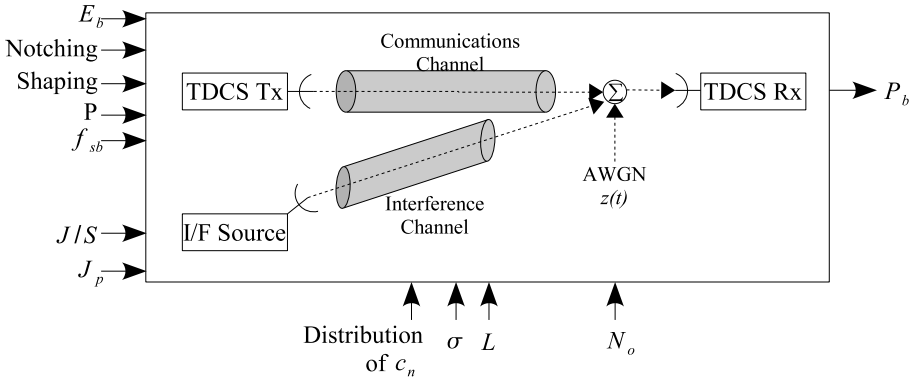

Figure 4.1: System Under Test

2. Symbol incorrectly detected and estimated

Since the system uses BPSK modulation, symbols are mapped directly to bits. Therefore, the quality of the system's symbol detection and estimation is measured by the probability of bit error, P_b given by (4.1).

$$P_b = \frac{\text{Number of bit errors}}{\text{Total bits transmitted}} \tag{4.1}$$

4.1.2 Workload. The workload for the system is the ratio E_b/N_o. The workload levels are discussed below.

4.1.3 System Parameters. In this research, parameters are the aspects of the system that could induce variation in the system services. Each of the system parameters for this research are defined and discussed with any assumptions in the sections below. Parameters that are varied in the experiments are named factors and are discussed in detail in a later section.

4.1.3.1 TDCS Transmitter/Receiver Subsystem Parameters.

Modulation Type Cyclic shift keying and phase shift keying are two primary modulation schemes historically applied to the TDCS [6] [9]. Since both have the same "noise-like" characteristics, yielding a low autocorrelation, this parameter should have little effect on the performance of the system. Binary phase shift keying (BPSK) is used exclusively in the simulations since the analytical performance of the TDCS is accurately predictable using traditional analysis techniques.

Data Symbols The data modulated using the TDCS affects the actual signals transmitted. Since this research assumes equal energy antipodal signaling, the data should not effect the energy being transmitted or probability of bit error performance. Therefore, uniformly random symbols are generated and transmitted.

Bit rate, R_b This represents the bit rate into the TDCS modulator. This parameter along with the modulation scheme determines the symbol rate and duration. Since BPSK modulation is used in the experiments, $R_b = f_{sb}$. To meet the criteria outlined in Section 2.2.2 required for the channel to be modeled as a FSSF, R_b is set at 10kbps.

Fundamental frequency, f_{sb} This is the lowest frequency component in the TDCS waveform as well as the tone spacing between the spectral components of the waveform. Since it is also equal to the symbol/bit rate as described above, f_{sb} is equal to 10kHz.

Number of spectral components, P The number of spectral components in the TDCS waveform affects the bandwidth of the transmitted signal W_{BB}. As stated in Chapter II, it also affects the channel model. To meet the criteria for the channel to be assumed a FSSF, P is set to 1024. This yields a baseband bandwidth of greater than 10MHz, which meets the criteria discussed in Section 2.2.2 for both urban and suburban environments in all cases.

Spectral amplitude vector A_p The spectral amplitudes of the TDCS signals are a system factor and are discussed later.

Notching Algorithm This parameter effects the amount of energy from the interferer that is present in the demodulator test statistic. The notching algorithm is a system factor.

Data phase encoding, θ_k . Since the modulation scheme is BPSK, the data phase maps data bits to phase shifts according to the following scheme: data '0' to 0 radians or a data '1' to π radians.

Random phase encoding, ϕ_p A number of different phase encoding schemes are mentioned in the literature. To minimize the autocorrelation of the TDCS signals, a $P-1$ length Gold Code $\{g_k\}$ is used to randomize the phase. The phase mapping of ϕ_p to either 0 or π radians occurs in the same manner as the

data bits are mapped to the phase of θ_k.

$$\phi_p = \begin{cases} 0 & \text{if } g_p = 0 \quad \forall p \neq 0 \\ \pi & \text{if } g_p = 1 \quad \forall p \neq 0 \\ 0 & \text{if } p = 0 \end{cases} \tag{4.2}$$

No multiple access phase coding is used. Since the autocorrelation of Gold codes is three-valued regardless of the code, the selection of generator polynomials and initial states is not expected to affect the results of the simulations. During pilot simulations, many generator polynomials and initial states were used without effect on P_b performance. For repeatability, generator polynomials 2011 and 2415 with initial states 1 and 71 respectively are used to generate the Gold Code in all simulations.

Digital-to-analog converter speed, f_{samp} This is the speed the TDCS transmitter converts digital samples to generate the analog waveform for transmission and demodulation. It is also the receiver's sampling rate of the downconverted (if used) waveform. For this research, f_{samp} is set at the Nyquist sampling rate $2Pf_{sb}$.

Normalized bit energy to noise power spectral density ratio, E_b/N_o This ratio is measured with reference to the transmitted E_b and is distinct from the SNR in the demodulator. The received SNR in the demodulator γ_b, is calculated after passing through the channel model. As mentioned above, this parameter is the system workload.

Shaping The algorithm used to provide the spectral shape of the TDCS signals. This parameter is a factor.

4.1.3.2 Interference Source Parameters.

Interferer Spectrum, J_p The spectral shape of an interference source effects the number of frequency components that are notched out of the TDCS spectrum.

To ensure consistency with results previously published, and to limit the scope of this research, the interference source used in these simulations is identical to the narrow-band interferer spectrum used in [6, 4-3,4].

Interferer Power to Signal Power Ratio, J/S This ratio determines the power spectral density of the interference source in the test statistic. To compare the results in this research with those in the literature, J/S is set to make the interferer power spectral density identical to that used by [6]. Using (2.12), and the parameters from [6, 4-3,4], $N_{i,Nunez}$ is calculated in (4.3).

$$N_{i,Nunez} = \frac{J_o}{P} = \frac{J/S \times E_{sym}}{P} = \frac{2E_{sym}}{32} \tag{4.3}$$

To solve for the appropriate J/S in these experiments, the parameter $P = 1024$ as stated above is used.

$$N_{i,Gaona} = \frac{J/S \times E_{sym}}{1024} = N_{i,Nunez} \tag{4.4}$$

$$\frac{J/S \times E_{sym}}{1024} = \frac{2E_{sym}}{32} \tag{4.5}$$

$$J/S = 64 \tag{4.6}$$

4.1.3.3 Channel Model Parameters.

Distribution of c_n Due to the assumption that the channel model is Rayleigh faded for this research, the c_n are complex Gaussian processes with a standard deviation of σ.

Given the distribution of c_n, the parameter σ must now be determined based on the assumption that the channel returns on average 100% of the energy transmitted through it. Recalling that the magnitudes of the c_n are Rayleigh random variables, the first and second moments of the Rayleigh distributed α_n can now be determined [7, 148]. The expression $\mathbf{V}[\cdot]$ denotes the variance

operator.

$$\begin{aligned} \mathbf{E}[\alpha] &= \sqrt{\frac{\pi}{2}}\sigma && (4.7) \\ \mathbf{V}[\alpha] &= (2-\pi/2)\sigma^2, \quad \text{therefore:} && (4.8) \\ \mathbf{E}[\alpha^2] &= \mathbf{V}[\alpha] + (\mathbf{E}[\alpha])^2 = 2\sigma^2 && (4.9) \end{aligned}$$

The previously stated assumption that on average, the channel returns 100% of the energy input by the transmitter, and the statistics above, yield the expectation in (4.10) when the α_n are independent and identically distributed.

$$\begin{aligned} \mathbf{E}\left[\int_0^{T_{sym}} |h_l(t)|^2\, dt\right] = \quad 1 &= \mathbf{E}\left[\int_0^{T_{sym}} \left|\sum_{n=1}^{L} \alpha_n e^{j\Theta_n}\delta(t-nT_{samp})\right|^2 dt\right] \\ 1 &= \mathbf{E}\left[\sum_{n=1}^{L}\alpha_n^2\right] = \mathbf{E}\left[L\alpha_n^2\right] \\ 1 &= L2\sigma^2, \quad \text{therefore:} \\ \sigma &= \sqrt{\frac{1}{2L}} \end{aligned} \tag{4.10}$$

AWGN Model This parameter affects the environment in which the TDCS receiver is trying to detect and estimate symbols within. Because complex low-pass equivalent analytical models are used in the analysis, the noise model uses a complex Gaussian noise distribution with a one-sided power spectral density of N_o.

Number of Taps in Multipath Model, L This parameter is related to T_m, and f_{samp} by (2.28). The ranges of values for T_m and L are determined to model a suburban environment [10, 162]. The specific values for T_m and their associated L are discussed in the factor section.

4.2 Experimental Design

Given the analysis above, the system workload and the factors selected for variation in the experiments, the design of experiments are presented next. Table 4.1 enumerates all of the proposed experiments. In each experimental batch, two types of TDCS signals are simulated through the identical conditions. The two alternatives compared are either spectrally encoded, shaped spectrum TDCS signals vs. un-encoded, flat spectrum TDCS signals; or notched vs un-notched spectrally encoded, shaped spectrum TDCS signals.

Table 4.1: Table of Experiments

Batch	E_b/N_o	L	**Spectral Encoding**	**Notching**	**Int.**	**Interference Channel**
1	0-20dB, 2dB steps	2	Flat/Shaped	None	N/A	N/A
2	0-18dB, 2dB steps	4	Flat/Shaped	None	N/A	N/A
3	0-12dB, 2dB steps	20	Flat/Shaped	None	N/A	N/A
4	0-12dB, 2dB steps	50	Flat/Shaped	None	N/A	N/A
5	0-20dB, 2dB steps	2	Shaped	Notched/None	NB[1]	AWGN
6	0-18dB, 2dB steps	4	Shaped	Notched/None	NB	AWGN
7	0-12dB, 2dB steps	20	Shaped	Notched/None	NB	AWGN
8	0-10dB, 2dB steps	50	Shaped	Notched/None	NB	AWGN
9	0-20dB, 2dB steps	2	Shaped	Notched/None	NB	FSSF
10	0-20dB, 2dB steps	4	Shaped	Notched/None	NB	FSSF
11	0-12dB, 2dB steps	20	Shaped	Notched/None	NB	FSSF
12	0-10dB, 2dB steps	50	Shaped	Notched/None	NB	FSSF

[1]Narrow Band

4.2.1 Factors.

E_b/N_o Depending on the level number of taps in the channel model, this ratio is varied from either 0-12.0dB or 0-8.0dB in 2.0dB steps. These ranges cover predicted P_b levels from 0.1 through 10^{-5}. The step size provides sufficient resolution to resolve trends and distinguish performance between the TDCS signals being compared in the various experiments.

L, T_m The length of the delay spread, and accordingly the number of delay taps in the model, are varied to cover the range of typical and worst-case suburban environments [10, 162]. Given the f_{samp} ($2P \cdot 10\text{kHz} = 20.48\text{MHz}$) established above, Table 4.2 contains the modeled delay spread values and the corresponding number of delay taps.

Table 4.2: Delay Spread vs Number of Delay Taps

Delay Spread μs	**No. Delay Taps (L)**
0.1	2
0.2	4
1	20
2.5	50

Spectral Shaping Two different spectral shaping methods are compared. Flat spectrum TDCS signals use equal amplitude frequency components (except the DC and Nyquist frequencies) as discussed in Section 3.4. Shaped spectrum TDCS signals use the FSSF multipath channel transfer function magnitude response to establish the TDCS spectral shape as discussed in Section 3.5. In both cases, the basic spectral shape is scaled to maintain constant energy signaling.

Interference Avoidance To limit the scope of this research, and compare to previously published results from [6], the interference avoidance algorithm notches spectral components above a manually set threshold of 1, as discussed in Section 3.7.3. The experiments either use the algorithm or disable it. In an environment without multipath fading, this algorithm attenuates the interferer's energy in the test statistic by 11.8dB.

Interferer Channel To compare the performance of the of the TDCS interference avoidance capability as discussed above, the interference channel is modeled in two ways. To simulate an environment where the TDCS receiver and the interferer are geographically separated, the channel is independent but modeled identically to the communications channel. When simulating the close proximity

interference avoidance situation, the interference channel passes the interferer through unchanged.

Now that the listing of experiments and the levels of the factors to be varied have been presented, each class of experiment is discussed in the context of the overall goals of this research.

4.2.2 Spectral Encoding Experiments. The first four batches of experiments are designed to verify the first hypothesis: that spectral shaping should achieve a better probability of bit error performance through a FSSF multipath fading channel. These experiments simulate the transmission, detection and estimation of both flat spectrum and shaped spectrum TDCS signals through identical channels. No interferer is simulated in these experiments. For each level of L, E_b/N_o is varied across the entire range of values specified for Batches 1 through 4 in Table 4.1. The probability of bit error for flat and shaped spectrum signals is compared over the entire range of E_b/N_o independently for each level of L. The simulated results are also verified against the analytical predictions using numerical computations of the formulas from Sections 3.4.1 and 3.5.2.

4.2.3 Interference Avoidance Experiments. The last eight batches of experiments are designed to verify the second hypothesis: that the TDCS retains an interference avoidance capability in a FSSF multipath environment. These experiments simulate the transmission, detection and estimation of shaped spectrum TDCS signals in the presence of an interferer both with and without the notching algorithm. Again, for each level of L, E_b/N_o is varied across the entire range of values specified for Batches 5 through 12 in Table 4.1. In Batches 5 through 8, the interferer is passed through an independent FSSF multipath channel. In Batches 9 through 12, the interferer is passed through directly to the AWGN source in the channel.

The probability of bit error for the notched and un-notched signals is compared over the entire range of E_b/N_o independently for each level of L. The two cases

of simulation results are considered independently and compared to the analytical predictions using numerical computations of the formulas from Equations 2.11.

4.2.4 Confidence Intervals and Iterations Per Experiment. Confidence intervals on the simulation results provide an assurance that the simulated results are within a quantifiable statistical range of accuracy. Equation (4.11) is the confidence interval on any ratio p [3, 217].

$$100(1-\alpha)\% \text{ Confidence Interval} \quad = \quad p \pm z_{1-\alpha/2}\sqrt{\frac{p(1-p)}{n}} \tag{4.11}$$

In (4.11), z_t is the t^{th}-quantile of the standard normal distribution and n is the number of iterations in the experiment. It is desired that the confidence interval reach a certain precision to quantify the confidence interval. The relationship between the confidence interval and the precision ψ, in terms of the ratio p is (4.12).

$$p \pm \psi p \quad = \quad p \pm z_{1-\alpha/2}\sqrt{\frac{p(1-p)}{n}} \tag{4.12}$$

Therefore, the number of iterations required for an experiment to achieve a 100(1-α)% confidence interval that is within ψ of the analytically predicted probability of bit error P_b, is found by manipulating (4.11) into the following form.

$$n \quad = \quad P_b(1-P_b)\left(\frac{2z_{1-\alpha/2}}{P_b\psi}\right)^2 \tag{4.13}$$

Using (4.13), the number of iterations required per experiment is calculated using the confidence intervals shown in Table 4.3 and the analytical predictions discussed for each experiment in Sections 4.2.2 and 4.2.3. The differences between the batches are

Table 4.3: Confidence Intervals by Experimental Batch

Batch	**Precision ψ**	**Confidence Interval (1-α)100%**
1, 2, 5, 6, 9, 10	10% P_b	95%
3, 4, 7, 8, 11 12	10% P_b	90%

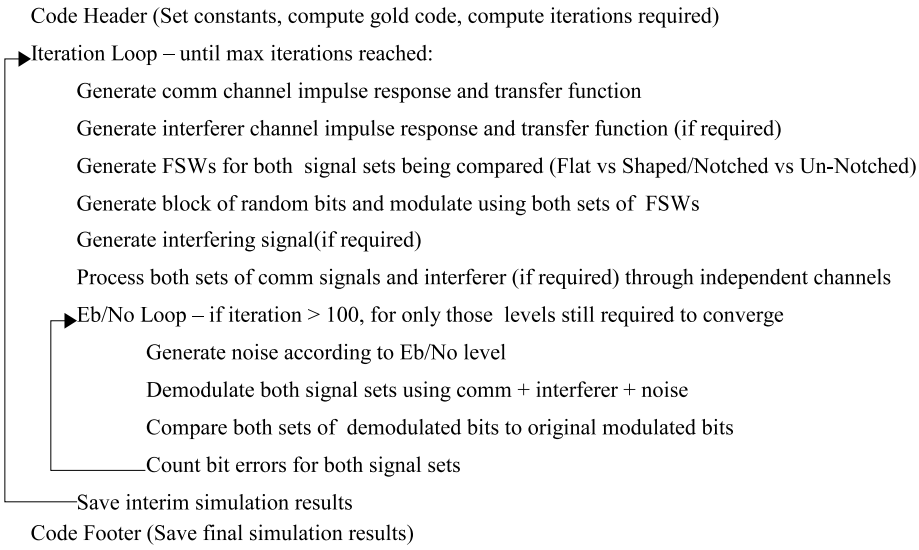

Figure 4.2: Structure of Monte Carlo Simulation

to compensate for the longer simulation times required for experiments when $L = 20$, 50. Since these simulations run longer, a lower confidence interval is designed to decrease the simulation run time, yet still provide a high degree of confidence that the simulated results are within the specified precision.

4.2.5 Simulation Structure. All experiments are simulated using Monte Carlo methods to average out the impacts of the random processes on the results. The components in the system under test are simulated using complex low-pass equivalent models. The simulation is structured to evaluate several experiments at one time. As shown in Figure 4.2, within a given batch, all experiments required for a single level of L (full range of E_b/N_o, both TDCS signal types) are simulated in the same simulation code.

Blocks of random bits modulated inside the iteration loop are 100 bits long. Therefore the number of iterations is the maximum required according to the confidence interval calculations divided by the block size. For a single channel instantiation, both shaping or interference avoidance techniques are simulated. Both signal sets are processed through identical channel instantiations, interferers and noise in-

stantiations. This consistency ensures that the effect being measured is due only to the difference in the FSW structure. The logic check in the E_b/N_o loop requires that all experiments are simulated through at least 100 channel instantiations. At lower E_b/N_o levels, the number of bits required for the simulations to converge to the required confidence intervals is on the order of 100s of bits. Without the logic check, the simulation would terminate this experiment after only a few instantiations of the FSSF multipath channel, which would not average out transient effects in the channel.

4.3 Summary

This chapter contains the foundation for the simulation portion of this research. The system under test is described along with the parameters that could affect the results of the simulation. The experimental design, including the system workload and the factors to be varied during the simulation experiments are also described. Finally, the methods for verifying the analysis through simulation were described and tied to the goals and hypothesis of this research.

V. Simulation Results

Earlier chapters review the literature survey, analysis and design of experiments. This chapter contains the results of the simulation experiments. The first section compares the simulation results of spectrally encoded, shaped spectrum TDCS signals to un-encoded, flat spectrum TDCS signals. The second section compares the simulation results of notched and un-notched, spectrally encoded, shaped spectrum TDCS signals in the two interference avoidance scenarios described in Section 3.7. Both sections compare the results of two types of simulations to the analytical predictions contained in Chapter III. Each section contains independent plots for each value L (2, 4, 20, 50).

5.1 Spectral Encoding Results

As discussed in Chapter IV, the first set of experiments are designed to answer the first goal of the research, namely: to compare the performance of spectrally encoded, shaped spectrum TDCS signals to un-encoded, flat spectrum TDCS signals in a FSSF multipath channel using an L-diversity TDCS RAKE receiver. This section presents P_b curves for each level of L containing the simulation results and analytical predictions. As a reminder, in each figure, probability of bit error is plotted against the *transmitted* E_b/N_o. Each P_b curve contains two reference lines, two analytical P_b prediction lines and two simulation P_b lines. The first reference line represents a BPSK matched filter demodulator through a FSSF multipath channel with no diversity (i.e., worst-case). The second reference is the BPSK matched filter demodulator through an AWGN channel, representing the theoretical best-case. The analytical P_b predictions are identical to those plotted in Chapter III.

5.1.1 Spectral Encoding: $L = 2$. The first two sections of the results discuss the simulations of typical suburban environments [10, 162]. Figure 5.1 shows the simulated results in comparison to the two reference lines and the two predictions. By visual inspection, it is clear that each P_b prediction is consistent with the simulated results. Qualitatively, the simulated spectrally encoded, shaped spectrum TDCS sig-

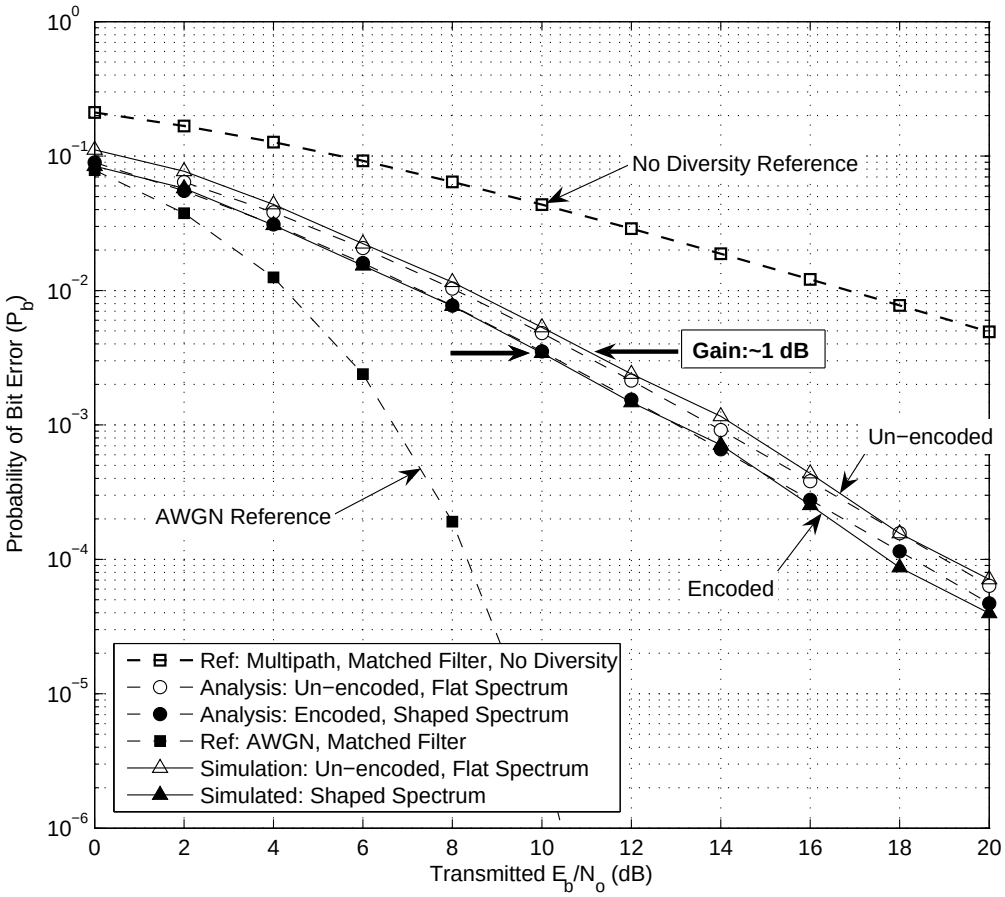

Figure 5.1: **Spectral Encoding Results, $L = 2$.** The simulations are consistent with the analysis. The results show approximately 1.0dB gain realized by spectral encoding.

nal has a better P_b than the un-encoded, flat spectrum TDCS signal at each E_b/N_o as predicted. Using (3.67), and by graphically estimating gain G in Figure 5.1, the spectrally encoded TDCS signals provide an approximate 1dB gain over the un-encoded TDCS signals as seen in the analytical results.

After simulating 3.2×10^7 bits, it is notable that the analytical results are not within 10% of the simulation results as predicted by the 95% confidence interval. The difference between the analytical and simulation results may be explained by inexact P_b predictions. The spectrally encoded signal energy pdf estimation may cause inaccuracies in the numerical P_b calculations. Errors in the analytical P_b prediction approximations may be the source of differences for the un-encoded TDCS signals.

5.1.2 Spectral Encoding: $L = 4$. The P_b curve for $L = 4$ in Figure 5.2 reveals several qualitative results. However, since the simulation did not complete, some general comments are in order. The simulation generated 4.0×10^7 bits which is sufficient for the confidence interval to converge as designed (c.f. Section 4.2.4) for spectrally encoded, shaped spectrum TDCS signal E_b/N_o between 0.0dB and 12.0dB, and for un-encoded, flat spectrum TDCS signal E_b/N_o between 0.0dB and 16.0dB. Additional iterations may have caused the simulated results to converge to the analytical predictions; however, time was not available to complete the simulations. In light of this information, it is not clear whether the divergence in the shaped signal analytical and simulation results seen in Figure 5.2 is due to inaccuracies in the analysis or whether running the simulation longer would cause the two curves to converge.

Overall, the spectrally encoded TDCS signals perform at a lower P_b than the un-encoded signals as predicted. For the $L = 4$ simulation results, the graphically estimated gain for spectrally encoded vs un-encoded signals is approximately 2dB across the range of P_b plotted. There is one other trend worth noting in these results. At lower levels of E_b/N_o, notice that the spectrally encoded, shaped spectrum TDCS signal P_b is better (less) than the reference line for the BPSK matched fil-

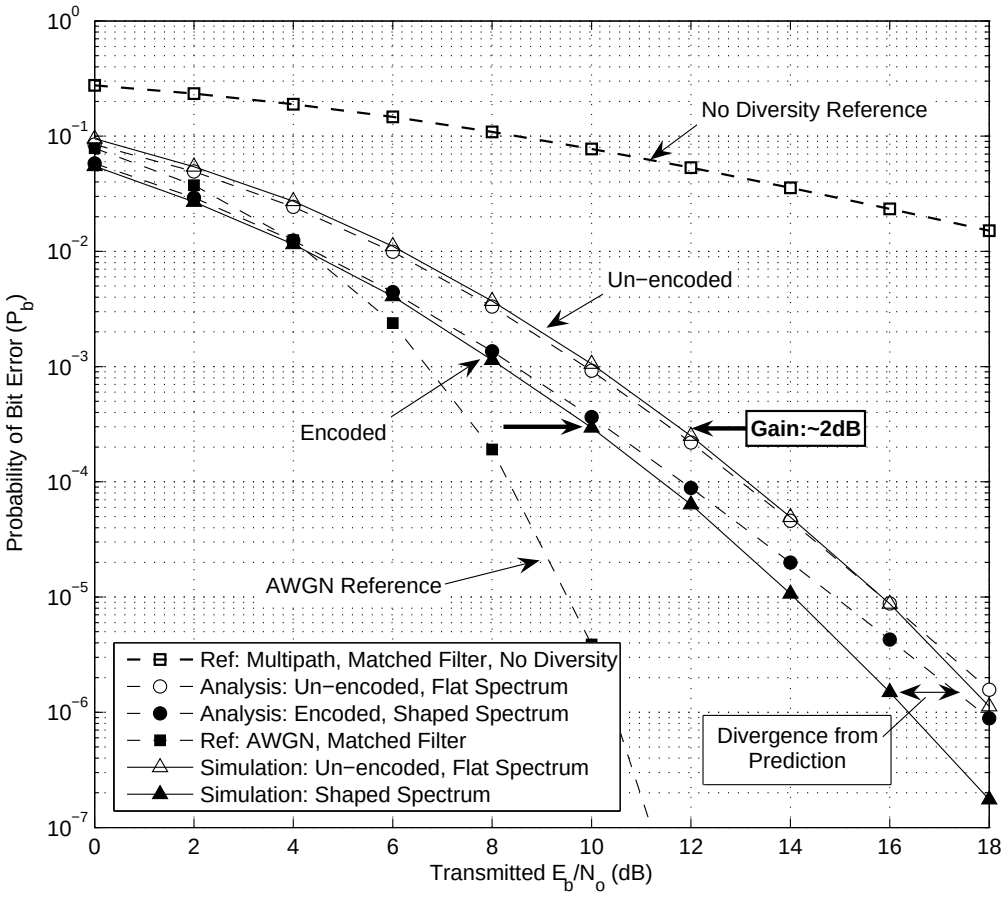

Figure 5.2: **Spectral Encoding Results,** $L = 4$**.** Analytical and simulated results are consistent again, demonstrating approximately 2.0dB gain for spectral encoding. Divergence between spectrally encoded simulation and analysis results for $E_b/N_o > 12.0$dB caused by either 1) incomplete simulation, or 2) inaccurate analytical prediction. Note that spectral encoding P_b is better than the "best-case" AWGN reference for $E_b/N_o < 4.0$dB.

ter in AWGN only. This effect is caused by the spectral encoding algorithm. The algorithm maximizes "amplification" and minimizes "filtering" across the different frequency bands in the channel transfer function spectrum. Therefore the received SNR in the demodulator γ_b is greater than the transmitted SNR E_b/N_o. This phenomenon combined with the diversity from the RAKE receiver is what enables the spectrally encoded, shaped spectrum TDCS signal to have a better (lower) P_b than the "best-case" reference line.

5.1.3 Spectral Encoding: $L = 20$. As a reminder, the results for $L = 20$, and 50 are representative of the worst-case suburban environment described in [10, 162]. For $L = 20$, the simulation results are displayed in Figure 5.3.

The analytical results are qualitatively consistent with the simulation results for both the spectrally encoded, shaped spectrum TDCS signals and un-encoded, flat spectrum TDCS signals. The spectrally encoded signals also perform at a lower P_b than the un-encoded signals as predicted. In the $L = 20$ simulations, the spectrally encoded vs un-encoded graphical estimation of gain is approximately 2.5dB across the range of P_b plotted. Note that across the range of transmitted E_b/N_o in these results, the spectrally encoded, shaped spectrum TDCS signal P_b is better (lower) than the BPSK in AWGN reference. As discussed in the $L = 4$ section, this is a result of the combined effects of the spectral encoding algorithm and receiver diversity. The un-encoded P_b curve appears to be converging to the BPSK in AWGN reference line as L increases. Since the research assumptions and simulation design ensure that on average, 100% of the energy transmitted into the channel is returned, then as the diversity increases, it is postulated that the un-encoded, flat spectrum TDCS signals will approach the BPSK in AWGN P_b reference until the intersymbol- and self-interference terms increase and overcome the benefit of the diversity.

5.1.4 Spectral Encoding: $L = 50$. For $L = 50$, Figure 5.4 contains the analysis and simulation results. As in the previous comparisons of the spectrally encoded, shaped spectrum TDCS signals and un-encoded, flat spectrum TDCS signals,

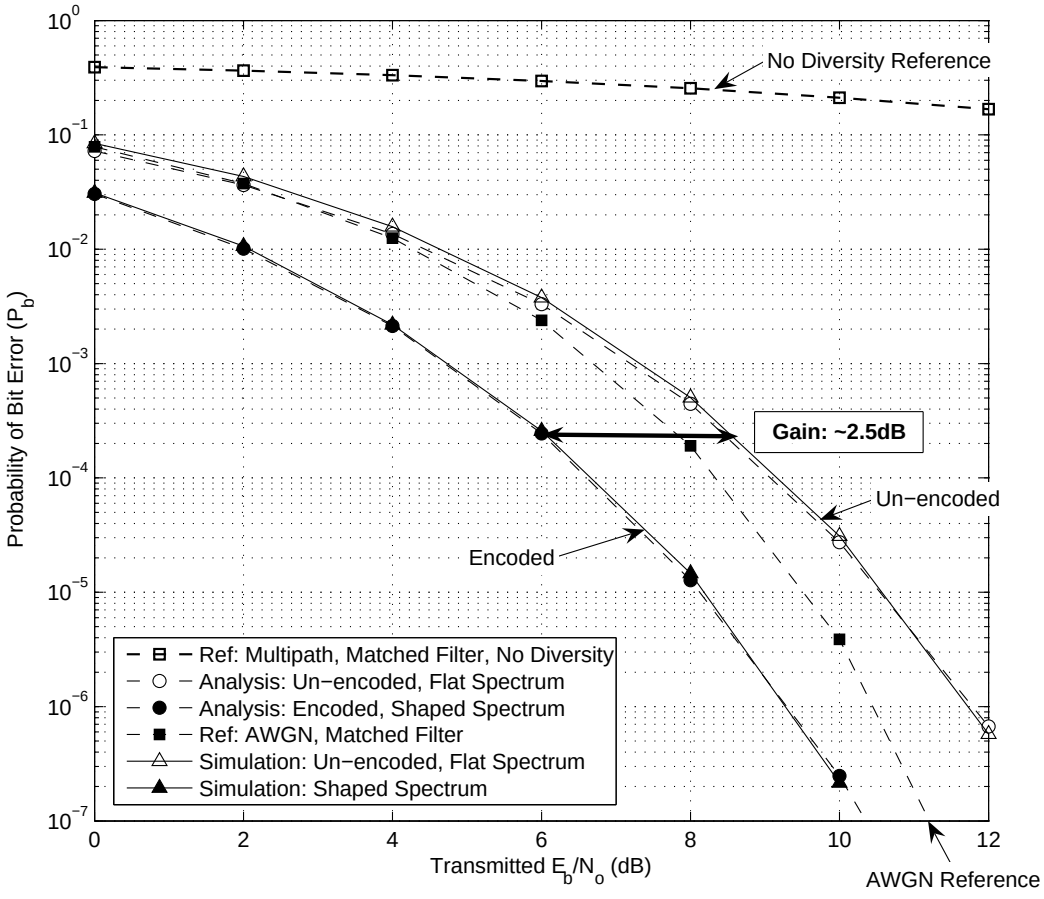

Figure 5.3: **Spectral Encoding Results,** $L = 20$**.** Analytical and simulated results are consistent and demonstrate approximately 2.5dB gain for spectral encoding. Spectral encoding P_b is better than the "best-case" AWGN reference for all E_b/N_o in plot. Un-encoded results start to converge toward AWGN reference.

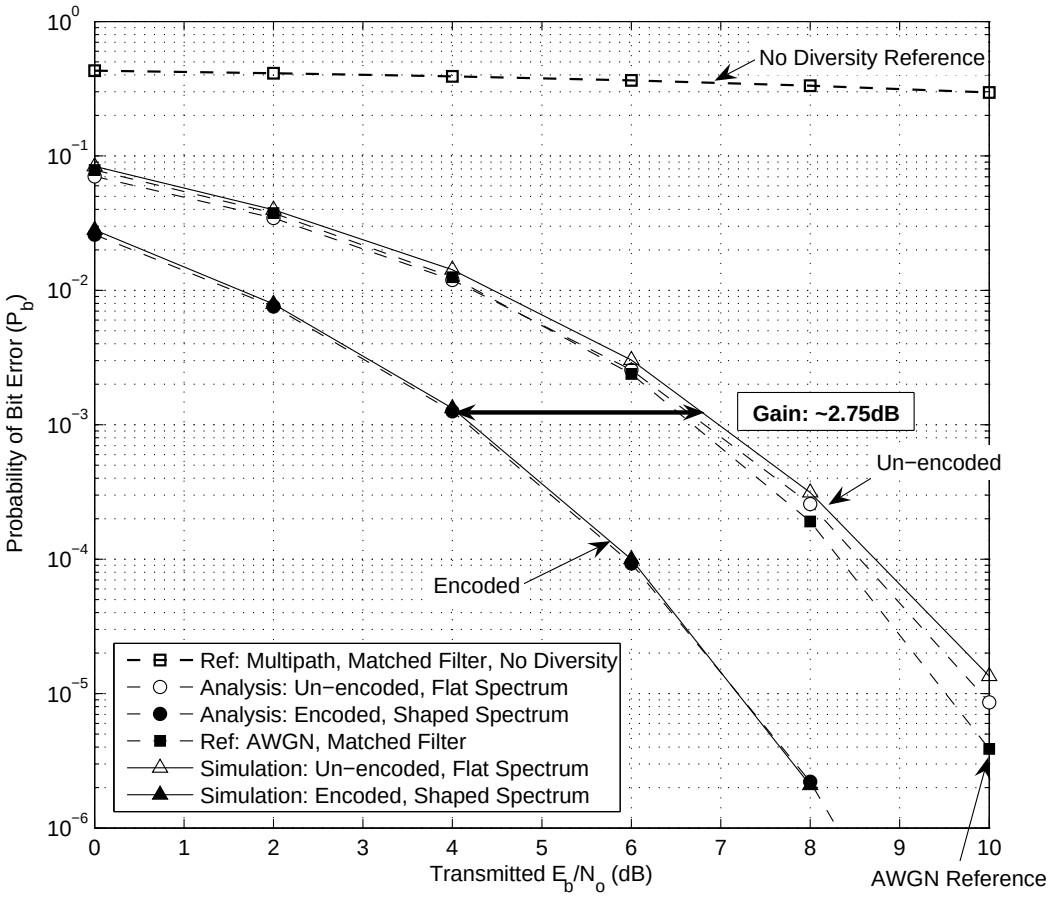

Figure 5.4: **Spectral Encoding Results,** $L = 50$**.** Analytical and simulated results are consistent and demonstrate approximately 2.75dB gain for spectral encoding. Again, spectral encoding P_b is better than the "best-case" AWGN reference for all E_b/N_o in plot. Un-encoded results continue to converge toward AWGN reference.

the analytical results are consistent with the simulation results. The un-encoded P_b curves continue to converge toward the BPSK in AWGN reference and the spectrally encoded P_b curves continue to improve beyond the BPSK in AWGN reference. In the $L = 50$ simulations, the graphically estimated gain for spectrally encoded vs un-encoded signals is slightly above 2.75dB across the range of P_b plotted.

5.1.5 Spectral Encoding Results: Interim Summary. In the sections above, the first goal of the research has been achieved. Spectrally encoded, shaped spectrum TDCS signal P_b has been compared to un-encoded, flat spectrum TDCS signal P_b through a FSSF multipath channel using an L-diversity RAKE Receiver. The hypothesis for this portion of the research was that the spectrally encoded signals would pass more energy through the FSSF multipath channel and therefore have a lower (better) P_b than the un-encoded signals. Chapter III presents the analytical P_b results for both the spectrally encoded and un-encoded signals. Here, the results of the both the analysis and simulations are presented with the overall result that the hypothesis was correct. A range of 1.0dB to 2.75dB gain in transmitted E_b/N_o, depending on the amount of diversity L in the channel and TDCS RAKE receiver, is realized in both the analyses and simulations simply by applying spectrally encoding to the TDCS signals to match the transfer function of the FSSF multipath channel. Additionally, the simulation results verify the analytically predicted P_b for both spectrally encoded and un-encoded TDCS signals using an L-diversity RAKE receiver.

5.2 Interference Avoidance: Spectrally Encoded Signals With and Without Spectral Notching

The results discussed in this section address the second goal of this research: to verify the interference avoidance capability of the spectrally encoded, shaped spectrum TDCS signals in a multipath fading environment by comparing the performance of notched and un-notched TDCS signals. As before, all simulations use the L-diversity

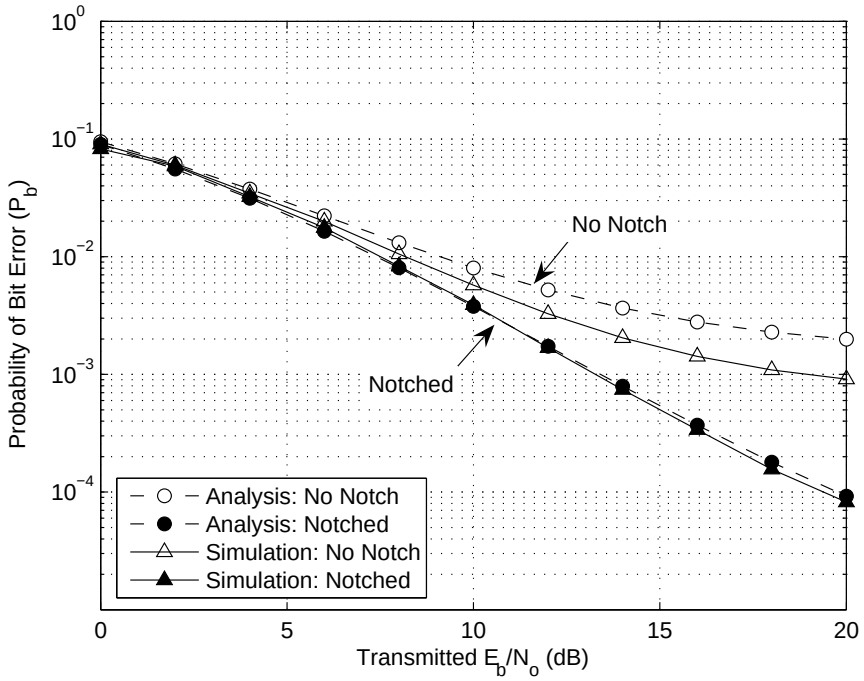

Figure 5.5: **Interference Avoidance I, $L = 2$.** No Multipath on Interferer, Notched vs Un-Notched Results. The notching algorithm shows no degradation in performance. The spectrally encoded TDCS signals even without notching demonstrate a significant amount of unintentional interference avoidance.

TDCS RAKE receiver. In Chapter III, two scenarios are presented and analyzed. The first scenario simulates the case where the interferer and the TDCS receiver are located in close proximity and therefore the interference channel is a pass through only. The second scenario simulates the situation in which the communications channel and interference channel are independent FSSF multipath channels. As in the previous section, the results are discussed in order of increasing diversity ($L = 2$, 4, 20, and 50) beginning with the first scenario. To simplify the plots, only the analytical predictions and simulated results are plotted. The reference curves are omitted.

5.2.1 Interference Avoidance I: No Multipath on Interference Channel.

5.2.1.1 Interference Avoidance I: $L = 2$. For $L = 2$, the simulation results are displayed in Figure 5.5. In this first set of interference avoidance results,

the general trends are as expected. At lower transmitted E_b/N_o ratios, the notched and un-notched P_b performance levels are nearly identical. Recalling the P_b prediction relationship from (2.11), it is clear that when N_o is large compared to N_i, the effect of the interference source is imperceptible on P_b performance. At higher E_b/N_o ratios, the opposite effect is witnessed in the un-notched results and predictions. In this case, the effect of N_i overshadows N_o and the P_b curve begins to flatten out. However, as expected, the notched results in this simulations do not exhibit this flattening effect at lower E_b/N_o, since a large amount of the interferer's energy has been notched out by the TDCS.

In Chapter III, it was predicted that the analytical curves would provide upper bounds for both the notched and un-notched simulations results. This trend is evident in both the notched and un-notched simulations. In the un-notched, spectrally encoded signals, there is a pronounced difference between the analysis and simulation. This demonstrates the un-intentional interference avoidance effect predicted in Chapter III. However, in the case of the notched, spectrally encoded signals, the separation is small between the analytical predictions and simulation results. It is expected that the reason for this limited improvement may lie in the relative flatness of the channel transfer functions when L is small. When $L = 2$, the channel transfer function is relatively flat due to the number of tap delays in the channel model. Therefore, it is likely that the interferer's spectrum is changed very little by the channel. This would cause the notching algorithm to perform nearly as expected.

To summarize, for $L = 2$ the simulation results are slightly better than the analytical predictions, as expected for the case when the interferer does not traverse a multipath fading channel.

5.2.1.2 Interference Avoidance I: $L = 4$. For $L = 4$, the simulation results are displayed in Figure 5.6. The trends in this set of simulations are nearly identical to those observed for the $L = 2$ case. The notched, spectrally encoded, shaped spectrum TDCS signal simulations are slightly less (better) than the analyt-

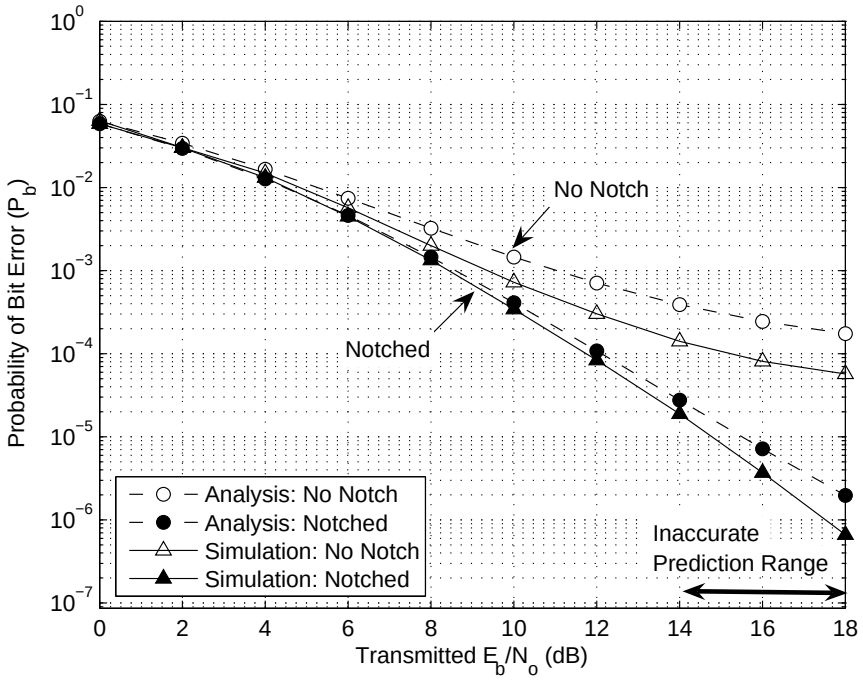

Figure 5.6: **Interference Avoidance I, $L = 4$.** No Multipath on Interferer, Notched vs Un-Notched Results. The notching algorithm shows no degradation in performance. No conclusions are drawn for the notched signals above $E_b/N_o > 12.0$dB due to inaccuracies in the analytical P_b results. The spectrally encoded TDCS signals even without notching continue to demonstrate the unintentional interference avoidance effect.

ical P_b curves as predicted in Chapter III. However at $E_b/N_o > 14.0$dB, as in the spectral encoding results, the analytical predictions may not be accurate. The un-notched, spectrally encoded signals continue to exhibit both the analytically predicted flattening and the un-intentional interference avoidance.

5.2.1.3 Interference Avoidance I: $L = 20$. For $L = 20$ and 50, the simulations model the worst-case suburban delay spread characteristics in the channel. For $L = 20$, the simulation results are displayed in Figure 5.7. This set of results presents some unexpected behaviors. Even though the interference channel is a pass through, and the notching algorithm should remove the full 11.8dB of interference energy, the P_b for the notched simulations is greater (worse) than predicted. It is expected that due to the high number of taps in the channel model, that the "fil-

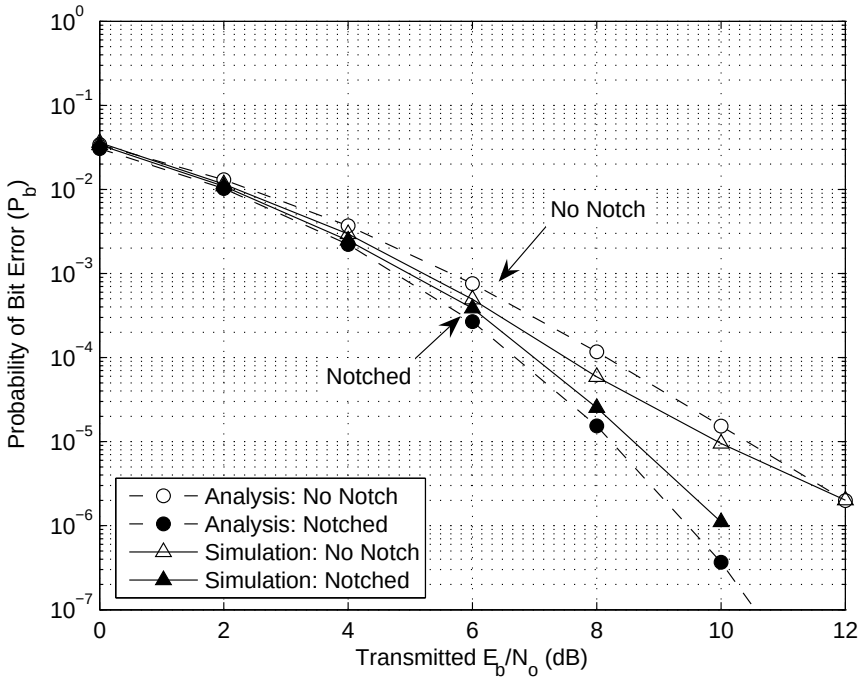

Figure 5.7: Simulated Interference Avoidance, No Multipath on Interferer, Notched vs Un-Notched Results, L=20

tering" in the remaining portions of the TDCS spectrum should remove more than the 11.8dB of interferer power expected. The unexpected results may be due to the equally likely "amplifying" effect in the channel, or the higher PSD caused by the notching algorithm which effectively reduces the bandwidth of the TDCS signal. In contrast, the un-notched, spectrally encoded TDCS signals continue to exhibit the predicted performance. The simulations continue to exhibit the un-intentional interference avoidance and flattening due to the interferer power.

5.2.1.4 Interference Avoidance I: $L = 50$. For $L = 50$, the simulation results are displayed in Figure 5.8. The results for the $L = 50$ case are essentially the same as those seen in the $L = 20$ experiments. The notched signals present the same unpredicted behavior, performing worse than predicted while the un-notched signals perform as expected. The exact analytical explanation of this phenomena is left for further research.

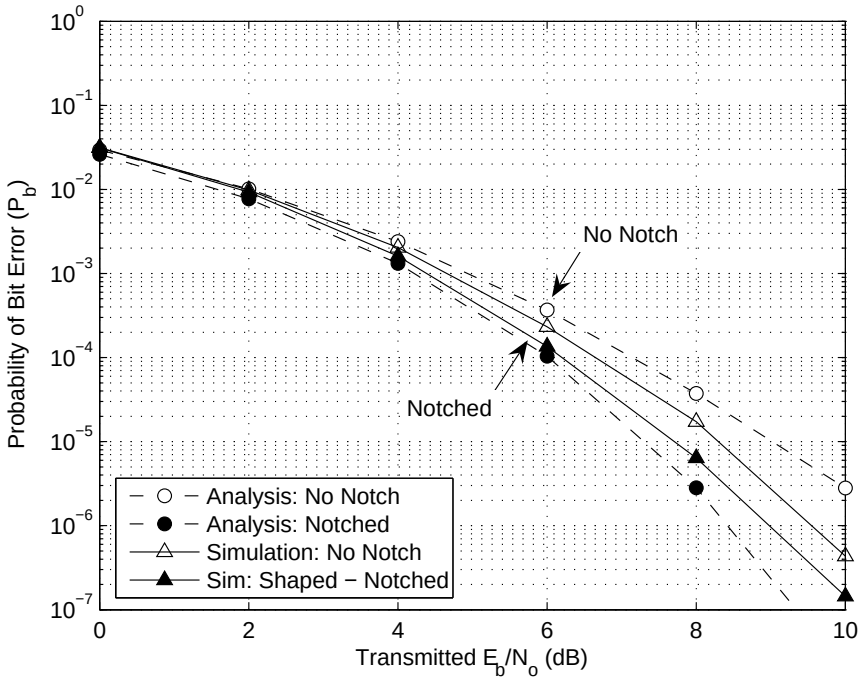

Figure 5.8: Simulated Interference Avoidance, No Multipath on Interferer, Notched vs Un-Notched Results, L=50

5.2.2 Interference Avoidance II: Independent Multipath Channels. In this second set of interference avoidance simulations, the results are also presented in order of increasing diversity (L). As in the previous interference avoidance results, no references are included. The predictions of the spectrally encoded, shaped spectrum TDCS signal P_b are included with and without the notching algorithm to suppress the interferer.

5.2.2.1 Interference Avoidance II: $L = 2$. For $L = 2$, the simulation results are displayed in Figure 5.9. The results for the second interference avoidance scenario for $L = 2$ are nearly identical the first scenario. In this plot, notice that at lower E_b/N_o ratios, the notched and un-notched P_b performance levels are nearly identical. The results also display the predicted flattening effect on the un-notched TDCS signal curves while the notched results in this simulations do not exhibit this flattening effect.

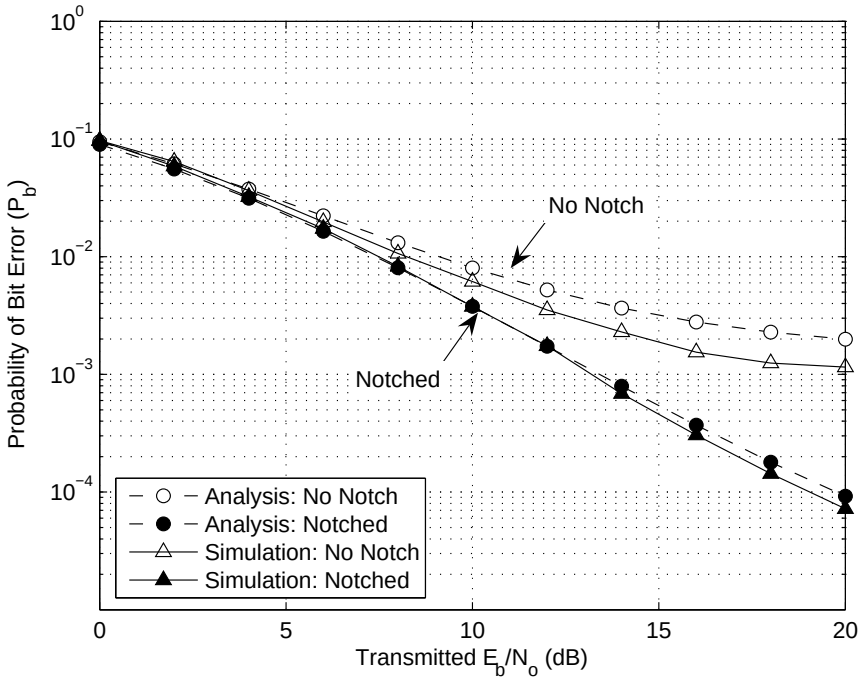

Figure 5.9: Simulated Interference Avoidance, Independent Multipath Channels, Notched vs Un-Notched, L=2

In Chapter III, it was predicted that the analytical predictions would be upper and lower bounds to the simulation results. While the un-notched prediction does provide an upper bound as expected, the notched simulations appear to have P_b equal to or better than the analytical prediction. As before, relying on intuition, it is expected that the reason for this improvement may lie in the relative flatness of the channel transfer functions when L is small. It is likely that the interferer's spectrum is changed very little by the channel, causing the notching algorithm to perform nearly as expected. Therefore, the results for both interference avoidance scenarios are expected to nearly identical.

5.2.2.2 Interference Avoidance II: $L = 4$. For $L = 4$, the simulation results are displayed in Figure 5.10. As seen in the $L = 2$ results, notice that at lower E_b/N_o ratios, the notched and un-notched P_b performance levels are nearly identical as expected. Also, notice the flattening effect on the un-notched TDCS signal curves

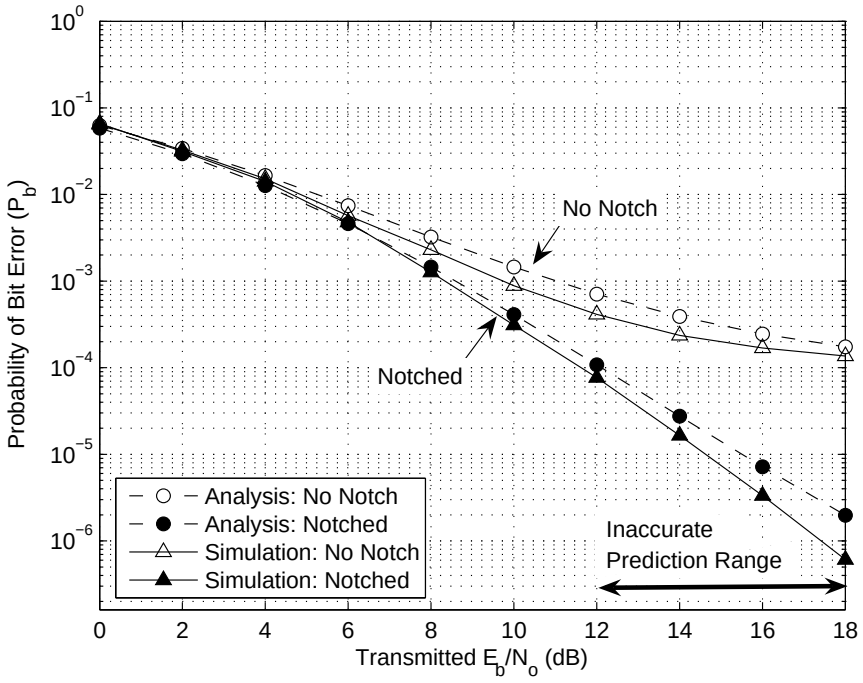

Figure 5.10: Simulated Interference Avoidance, Independent Multipath Channels, Notched vs Un-Notched, L=4

while the notched results in this simulations do not exhibit this flattening effect. Again all of these effects are expected.

Returning to the predictions of Chapter III, the un-notched prediction does provide an upper bound as expected. In contrast to the predictions, these simulations show the notched signals appear to have P_b very close to or just slightly better than the analytical predictions. As in the previous case, this is likely due to the relative flatness of the channel transfer functions for $L = 4$. Recall also that the analytical P_b predictions are unreliable for $E_b/N_o > 14.0$dB. Notice that the un-notched simulations continue to perform better than the analytical P_b results as predicted, but not as well as in the first interference avoidance scenario, as shown in Figure 5.6. The degraded effect on the un-intentional interference avoidance may be caused by the second independent multipath channel. The effects of the shaping from the spectral encoding algorithm may counteract the "filtering" from the independent interference

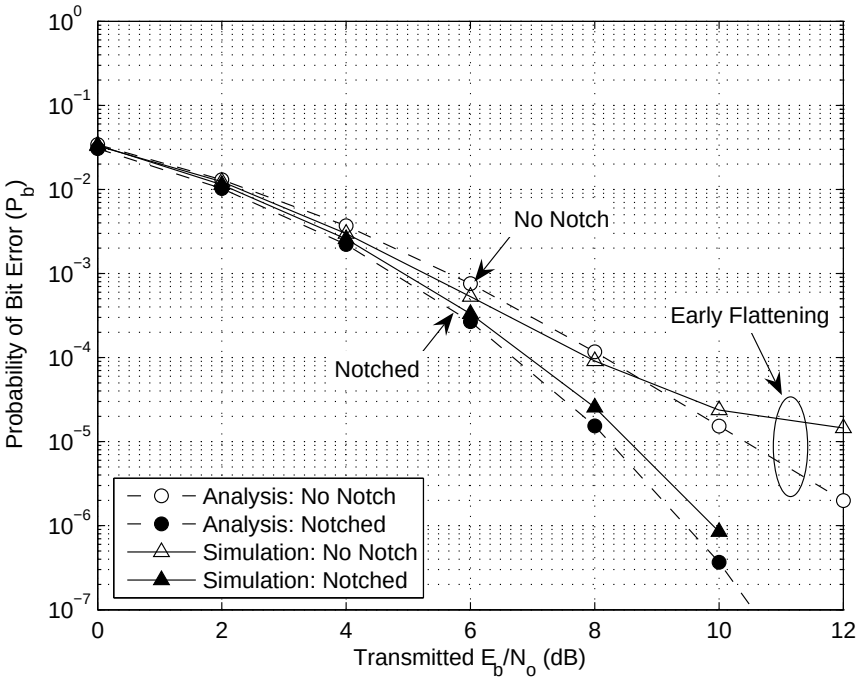

Figure 5.11: Simulated Interference Avoidance, Independent Multipath Channels, Notched vs Un-Notched, L=20

channel. This would cause the simulation results to more closely match the analytical P_b results for the un-notched signals.

5.2.2.3 Interference Avoidance II: $L = 20$. As a reminder, for the simulations in which $L = 20$ and 50, the channels are modelling worst-case suburban environment multi-path delays. For $L = 20$, the simulation results are displayed in Figure 5.11. In this plot, the flattening trend exhibited in the un-notched signal causes the simulated P_b to be greater (worse) than the analytical results. This early flattening may be caused by the combined effects of the independent communication and interference channels as described in the $L = 4$ results above.

The predictions of notched, spectrally encoded P_b from Chapter III appear to be more accurate for this simulation. The notched prediction forms a lower bound as expected, however the degradation appears to be slight. To summarize the results for $L = 20$, the notching algorithm does not appear to affect the full 11.8dB attenuation

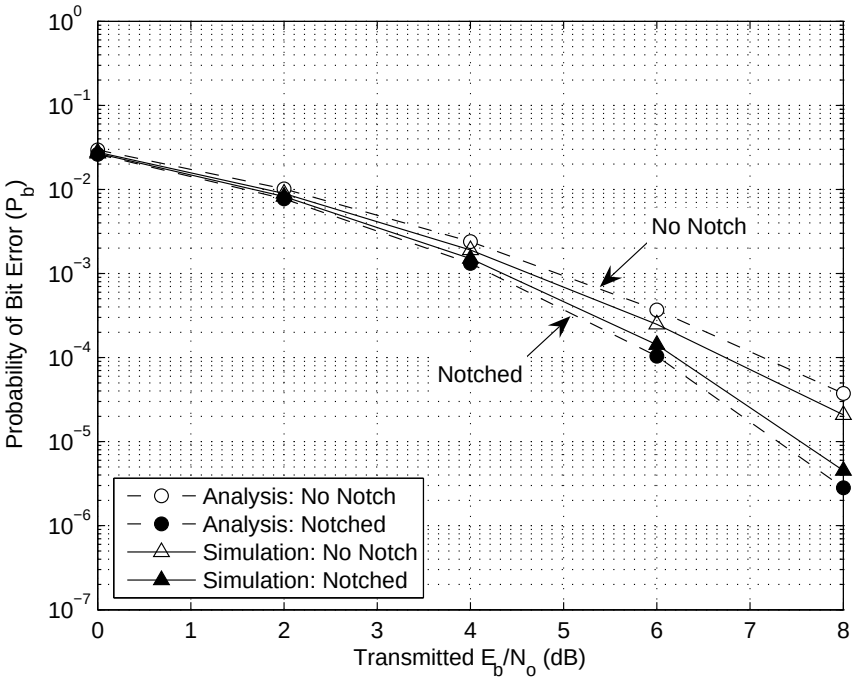

Figure 5.12: Simulated Interference Avoidance, Independent Multipath Channels, Notched vs Un-Notched, L=50

on the interferer when the communications and interference channels are independent multipath channels, and the un-notched results do not exhibit the predicted un-intentional interference avoidance for $E_b/N_o > 8.0$dB.

5.2.2.4 Interference Avoidance II: $L = 50$. For $L = 50$, the simulation results are displayed in Figure 5.12. The results from the $L = 50$ simulations follow similar trends as the $L = 20$ simulations, yielding a similar summary. Since the simulations cover E_b/N_o up to 8.0dB, the flattening effect is not yet realized in the un-notched, spectrally encoded signals. The un-notched signals exhibit the predicted un-intentional interference avoidance predicted. The interference avoidance notching algorithm remains effective at reducing the interferer's energy by slightly less than the predicted 11.8dB.

5.3 Summary

In this chapter, the simulation results verify most of the predicted outcomes developed in the analysis and verify the hypotheses set forth in Chapter II. First of all, the spectral encoding capability of the TDCS improves performance in a FSSF multipath channel over un-encoded signals by as much as 2.75dB in transmitted E_b/N_o. Second, in the interference avoidance experiments, for both the independent multipath case and the case in which the interferer experiences no multipath fading, the notching algorithm yields an improvement in probability of bit error. While the improvement is not as much as predicted for strictly AWGN channels, it is still significant. It was also demonstrated that even without notching to avoid interference, the shaped spectrum TDCS signals provide an distinguishable interference avoidance capability.

VI. Conclusions

Having completed the course of the research, this chapter reviews the thesis, summarizes the research conclusions and discusses areas for future research.

6.1 Summary

Before reviewing the summary of this work, recall the goals of this research are:

1. To compare the performance of spectrally encoded, shaped spectrum TDCS signals to un-encoded, flat spectrum TDCS signals in a FSSF multipath channel using an L-diversity TDCS RAKE receiver.
2. To evaluate the interference rejection capability of an L-diversity TDCS RAKE receiver using spectrally encoded, shaped spectrum TDCS signals in a FSSF, multipath channel.

To this end, beginning in Chapter II, this thesis presents a brief introduction to the M-ary phase shift keyed TDCS communications system, the associated interference avoidance capability, and probability of bit error prediction in AWGN. An introduction to the multipath fading channel describes basic channel parameters and their effect on the channel model. To support the assumptions of the research, the literature search also includes typical 900MHz cellular phone multipath channel characteristics and a brief discussion of channel estimation. The research assumptions specifically focused on the frequency-selective, slowly-fading (FSSF) multipath channel, modeled in this work as a tapped delay line. A discussion of P_b prediction in the multipath environment lends insight into the severe performance degradation caused by multipath fading channels. To overcome this degradation, diversity is incorporated into the communication system using the RAKE receiver. Probability of bit error prediction for the L-diversity RAKE receiver was introduced as well.

Chapter III applies the analysis of the TDCS to the FSSF multipath channel. The L-diversity RAKE receiver design is applied to the design of the TDCS receiver and analytical P_b predictions for both spectrally encoded and un-encoded TDCS sig-

nals are developed. Additionally, the interference avoidance capability of spectrally encoded, shaped spectrum TDCS signals is studied in the context of two different scenarios. The two scenarios help distinguish the effect of the FSSF multipath channel on the notching algorithm from the spectral encoding technique's "filtering" effect on the interferer. Qualitative predictions for the two interference avoidance scenarios use simple analytical P_b predictions for notched and un-notched spectrally encoded TDCS signals as bounding cases for the multipath fading results.

Chapter IV defines the simulation methodology. The system model provides a basis for understanding the parameters effecting the system under test. The design of experiments explains the methodology for verifying the analytical research results by controlling the variation of specific factors in simulation. The end of the chapter lists the specific experiments and derives the iterations required to achieve quantified confidence intervals.

The simulation results are presented in Chapter V along with a comparison to the analytical predictions. The results sections discuss deviations from analytical predictions and overall trends. The summary of the research findings are listed below.

6.2 Conclusions

With the original goals in view, the research conclusions based on the analyses and simulations follow.

6.2.1 Comparison of Spectrally Encoded, Shaped Spectrum TDCS Signals to Un-encoded, Flat Spectrum TDCS Signals. Given the assumptions of this research, it is clear that the application of spectral encoding produces a measurable improvement in P_b. Table 6.1 summarizes the simulation results at each level of diversity L by listing the estimated improvement in E_b/N_o for the spectrally encoded, shaped spectrum TDCS signals when compared to un-encoded, flat spectrum TDCS signals at equivalent P_b.

Table 6.1: Summary of Realized Gain Due to Spectral Encoding

Channel Diversity (L)	**Gain**
2	$\sim$ 1dB
4	$\sim$ 2.0dB
20	$\sim$ 2.5dB
50	$\sim$ 2.75dB

6.2.2 Comparison of Notched and Un-Notched Spectrally Encoded, Shaped Spectrum TDCS Signals in the Presence of a Narrow-Band Interferer. Two sets of simulations were executed to test the interference avoidance capability of the spectrally encoded, shaped spectrum signals demodulated by an L-diversity TDCS RAKE receiver both with and without the notching algorithm. In the first case, when the communications channel and interference channel were independent multipath fading channels, the TDCS notching algorithm exhibits a modest capability, rejecting just less than the predicted 11.8dB of the interferer's power. Notably, the spectrally encoded, shaped spectrum TDCS signals provide a significant measure of interference avoidance capability even without notching.

CHECK THIS PARAGRAPH In the second set of simulations, when the interference channel consisted of AWGN only, the TDCS performed similarly. When $L = 2$ or 4, the notched and un-notched signals performed as expected. The simulated results for both the notched and un-notched signals showed a lower (better) or equal P_b than analytically predicted using the interferer's PSD and the theoretical 11.8dB attenuation. However at the higher diversity levels ($L = 20$, 50), the notched signals failed to achieve the full 12dB attenuation predicted and therefore experienced a degraded P_b compared to the predictions. The notched signals, however, continued to exhibit an unintended interference avoidance effect yielding a lower (better) P_b than predicted.

6.3 Areas for Future Research

In the course of performing this research, additional topics were uncovered as areas for future study.

6.3.1 Application of Coding Techniques to the L-Diversity TDCS RAKE receiver. In addition to the diversity that is created by the FSSF channel and exploited by the RAKE receiver design, the TDCS employs another means of diversity in the P frequency components that are used to construct the FSWs. The application of orthogonal coding techniques similar to the multiple access coding scheme introduced by Nunez could be applied to flat spectrum TDCS signals in an orthogonal Q-ary PSK RAKE receiver [6]. In this case $Q = \log_2 P$. The probability of bit error for the BPSK spectrally shaped TDCS signals could be compared to that of the flat spectrum orthogonal Q-ary PSK phase encoded TDCS signals.

6.3.2 Application of Different Fading Models. This research assumed a Rayleigh fading model which characterizes communications channels in which there is no direct LOS path between the transmitter and receiver. This situation is more common in urban areas. The Ricean Fading model accounts for a direct signal path in addition to reflections and may more accurately model an air-to-ground communications scenario. Other models such as Nakagami fading channels could be applied as well.

An additional assumption was that the channel was frequency-selective and slowly-fading. The application of the diversity in the TDCS frequency components may yield a benefit in the frequency-nonselective multipath fading channel.

6.3.3 Continued Analysis of Interference Avoidance in the Multipath Environment. In this work, a very simplistic interferer and interference avoidance algorithm were simulated. Additionally, the analysis was primarily based on the AWGN channel model, with only intuitive insights offered on the performance of the algorithm against the interferer in the multipath channel. Future research could further the an-

alytical treatment of the interference source through the multipath channel. Different interference sources could be analyzed (e.g., partial and wideband) and alternative interference avoidance algorithms could be applied and analyzed.

6.3.4 Imperfect Channel Estimation. This research assumed that the channel estimate was perfect for a given number of symbols. However, knowing that fading channels are time-variant in nature, and that the changes occur continuously over time, consideration must be given to the effectiveness of spectral shaping when the channel estimate is imperfect. Research into the relationship between the channel estimation error and the effect on bit error performance could be conducted.

6.3.5 Multi-Access Communication Performance in a Multipath Environment. Nunez' research provided an elegant solution for orthogonal multiple access communication in a synchronous communication system, but requires flat spectrum TDCS signals. The effect of a fading channel environment on the multi-access communication network is an area of research could be pursued in light of the desired for networked communications. Additionally, an alternative means of multi-access coding could be developed that would allow that benefits of spectral shaping realized in this research.

6.3.6 Comparison to Traditional Spread Spectrum Techniques. Direct sequence spread spectrum (DSSS) and frequency hopped spread spectrum (FHSS) also make use of diversity techniques by either spreading the signal with a pseudo-random code word or repeating data in different frequency bands. A comparison of performance between TDCS shaping and DSSS and/or FHSS systems in a multi-path environment may reveal that at comparable spreading factors, there is a improvement in performance when using spectral encoding techniques.

Appendix A.

A.1 Distribution of the FSSF Multipath Channel Transfer Function Magnitude

To characterize the channel transfer function stochastically, start with (2.31), and substitute $\alpha_n e^{j\Theta_n} = c_n$.

$$H_l[m] = \sum_{n=1}^{L} \alpha_n e^{j\Theta_n} e^{j2\pi nm/N} \qquad m \in (0, N-1) \tag{A.1}$$

Recalling the distributions of α_n and Θ_n from (2.16) and (2.17), and combining the phase terms, such that $\Phi_n = \Theta_n + 2\pi nm/N$, $H_l[m]$ can be expressed as a sum of complex random variables shown below.

$$H_l[m] = \sum_{n=1}^{L} \alpha_n e^{j\Phi_n} \quad = \quad \sum_{n=1}^{L} u_n + jv_n \tag{A.2}$$

where:

$$u_n = \mathrm{Re}\left\{\alpha_n e^{j\Phi_n}\right\} = \alpha_n \cos\Phi_n \tag{A.3}$$

$$v_n = \mathrm{Im}\left\{\alpha_n e^{j\Phi_n}\right\} = \alpha_n \sin\Phi_n \tag{A.4}$$

$$\alpha_n = \sqrt{u_n^2 + v_n^2} \tag{A.5}$$

$$\tag{A.6}$$

The distribution of Φ_n is identical to Θ_n (it is still uniformly distributed between $-\pi$ and π) and the distribution for α_n has not changed. Since a random variable with Rayleigh distributed magnitude and uniformly distributed phase is a complex Gaussian random variable, $H_l[m] = C_m$ is a sum of L complex, zero-mean Gaussian random variables. That implies that u_n, v_n are zero-mean Gaussian random variables with variance of σ^2. The magnitude of the transfer function coefficients, H_m is now

given by the following equation.

$$
\begin{aligned}
H_m &= |\alpha_1 e^{j\Phi_1} + \alpha_2 e^{j\Phi_2} + ... + \alpha_L e^{j\Phi_L}| && \text{(A.7)} \\
&= |u_1 + jv_1 + u_2 + jv_2 + ... + u_L + jv_L| && \text{(A.8)} \\
&= \sqrt{(u_1 + u_2 + ... + u_L)^2 + (v_1 + v_2 + ... + v_L)^2} && \text{(A.9)} \\
H_m^2 &= (\sum_{n=1}^{L} u_n)^2 + (\sum_{n=1}^{L} v_n)^2 = w^2 + z^2 && \text{(A.10)}
\end{aligned}
$$

where,

$$
\begin{aligned}
w &= \sum_{n=1}^{L} u_n && \text{(A.11)} \\
z &= \sum_{n=1}^{L} v_n && \text{(A.12)}
\end{aligned}
$$

If it is assumed that the u_n and v_n are i.i.d. Gaussian, zero-mean random variables with variance σ^2, the distributions of w and z can be determined using the following property [7, 202].

$$
\begin{aligned}
X &= \sum_{i=1}^{n} a_i x_i \qquad \text{where } x_i \text{ are i.i.d} \sim N(0, \sigma^2) \\
A^2 &= \sum_{i=1}^{n} a_i^2 \\
X &\sim N(0, A^2\sigma^2) && \text{(A.13)}
\end{aligned}
$$

From the equation above, it is easily shown the distributions for w and z are as follows:

$$
\begin{aligned}
w &= \sum_{n=1}^{L} 1u_n && \text{(A.14)} \\
U^2 &= \sum_{n=1}^{L} 1^2 = L && \text{(A.15)} \\
w &\sim N(0, U^2\sigma^2) = N(0, L\sigma^2) && \text{(A.16)}
\end{aligned}
$$

By similarity, z is also a zero-mean Gaussian random variable with a variance of $L\sigma^2$. Substituting these distributions into (A.10), the normalized distribution of H_m^2 can be determined using the following relationship [7, jacket cover]:

$$\begin{aligned} x_i &\sim i.i.d.N(0,\sigma^2),\ i=1,2,...,n && \text{(A.17)} \\ X &= \sum_{i=1}^{n} x_i^2/\sigma^2 && \text{(A.18)} \\ X &\sim \chi^2(n), \quad \text{Chi-squared, n DOF} && \text{(A.19)} \end{aligned}$$

It follows from Equations A.10 and A.19 that the normalized distribution of H_m^2 is:

$$\begin{aligned} \frac{H_m^2}{L\sigma^2} &= \frac{w^2+z^2}{L\sigma^2} && \text{(A.20)} \\ x &= \frac{H_m^2}{L\sigma^2} \sim \chi^2(2) \qquad \text{Chi-squared, 2 DOF} && \text{(A.21)} \end{aligned}$$

with density function:

$$f_X(x) = \frac{e^{-x/2}}{2} \qquad \text{(A.22)}$$

Using the scaling property for random variables, the density function for H_m^2 is given by [7, 131]:

$$\begin{aligned} y &= L\sigma^2 x = H_m^2 && \text{(A.23)} \\ f_y(y) &= \frac{1}{|L\sigma^2|} f_x(\frac{y}{L\sigma^2}), \quad \text{therefore:} && \text{(A.24)} \\ f_y(y) &= \frac{1}{L\sigma^2}\left[\frac{e^{-y/2L\sigma^2}}{2}\right] && \text{(A.25)} \\ &= \frac{e^{-H_m^2/2L\sigma^2}}{2L\sigma^2} && \text{(A.26)} \end{aligned}$$

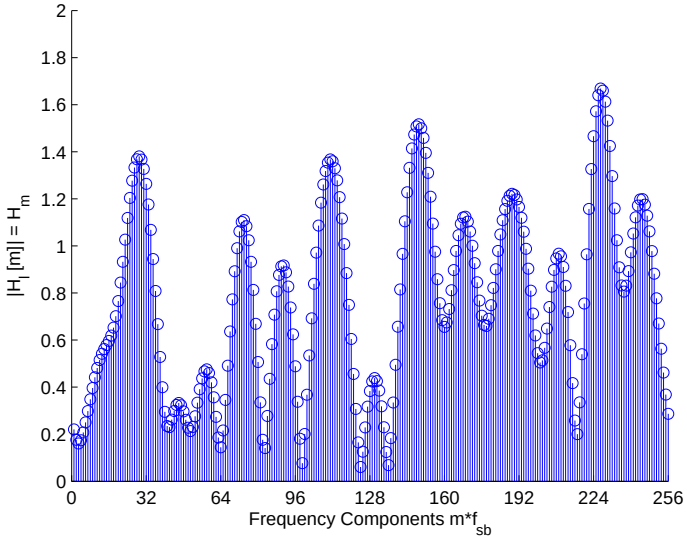

Figure A.1: Typical Multipath Fading Channel Transfer Function

A.2 Proof from Hypothesis 1: Spectrally Encoded, Shaped Signal Received Energy Exceeds Un-encoded, Flat Signal Received Energy

Consider the discrete-frequency representation of a typical FSSF multipath channel transfer function shown in Figure A.1 and the associated analytical representation in (A.27).

$$H_l[m] \quad = \quad H_m e^{j\Theta_m} \qquad m \in (0, N-1) \tag{A.27}$$

An un-encoded, flat spectrum TDCS signal shown in Figure A.2 and (A.28) is transmitted through the channel.

$$S_{flat}[m] = \begin{cases} A_p e^{+j(\phi_p+\theta_k)} & \text{if } p = m \quad \forall m \in (1, P-1) \\ A_p e^{-j(\phi_p+\theta_k)} & \text{if } p = m-N+1 \quad \forall m \in (P+1, N-1) \\ 0 & \text{otherwise} \end{cases} \tag{A.28}$$

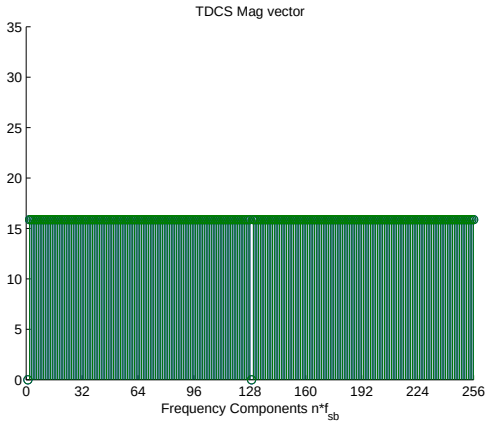

Figure A.2: Transmitted Flat Spectrum TDCS Signal

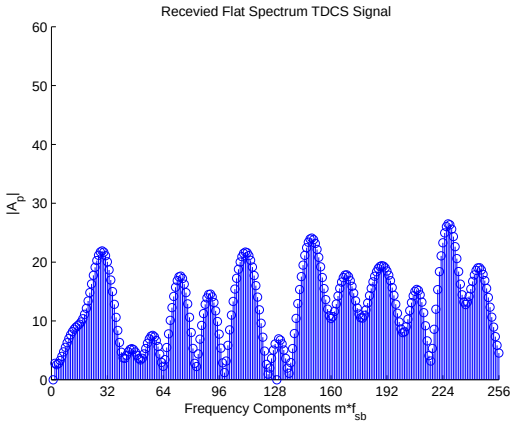

Figure A.3: Received Flat Spectrum TDCS Signal

From [6, 3-3], the energy in the discrete representation of the TDCS signal is given by:

$$E_{sym} = \frac{1}{N}\sum_{p=0}^{N-1}|A_p|^2 \tag{A.29}$$

If we assume that there are no DC or Nyquist frequency components, then $A_p = A_q \forall\ p, q \neq 0, N$, as is the case for the flat spectrum signal, then A_p can be solved for in terms of E_{sym} and N.

$$E_{sym} = \frac{1}{N}\sum_{p=0}^{N-1}A_p^2 \tag{A.30}$$

$$A_p = \sqrt{\frac{E_{sym}N}{N-2}} \tag{A.31}$$

The received, un-encoded, flat spectrum TDCS signal is found using the relationship $R_{flat} = S_{flat}H_m$ in the frequency domain, represented by Figure A.3 and (A.32).

$$R_{flat}[m] = \begin{cases} A_pH_me^{+j(\phi_p+\theta_k+\Theta_m)} & \text{if } p = m \quad \forall m \in (1, P-1) \\ A_pH_me^{-j(\phi_p+\theta_k+\Theta_m)} & \text{if } p = m-N+1 \quad \forall m \in (P+1, N-1) \\ 0 & \text{otherwise} \end{cases} \tag{A.32}$$

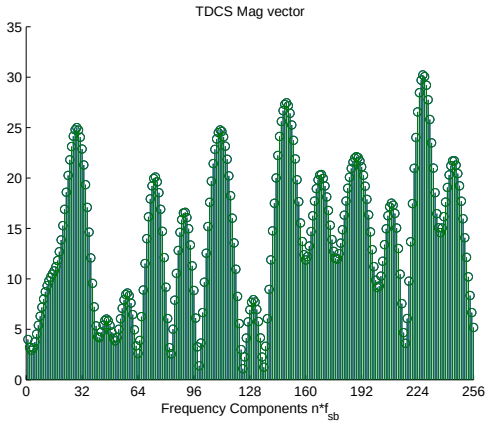

Figure A.4: Transmitted Shaped Spectrum TDCS Signal

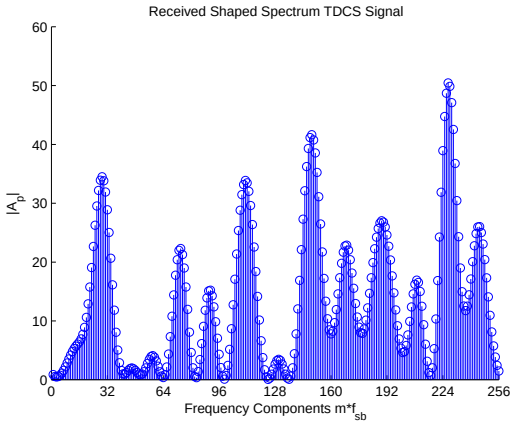

Figure A.5: Received Shaped Spectrum TDCS Signal

Therefore, it can be shown the energy in the received, un-encoded, flat spectrum TDCS signal γ_{flat} is given by:

$$\gamma_{flat} = \frac{1}{N}\sum_{p=0}^{N-1} A_p^2 H_p^2 \tag{A.33}$$

$$= \frac{E_{sym}}{N-2}\sum_{p=0}^{N-1} |H_p|^2 \tag{A.34}$$

Now consider the spectrally encoded, shaped spectrum TDCS signals formed using the magnitudes of the channel transfer function, and scaled to have energy equal to the un-coded, flat spectrum TDCS signals. An example of the transmitted shaped spectrum TDCS signal is shown in Figure A.4 and (A.35).

$$S_{shaped}[m] = \begin{cases} KH_m e^{+j(\phi_p+\theta_k)} & \text{if } p = m \quad \forall m \in (1, P-1) \\ KH_m e^{-j(\phi_p+\theta_k)} & \text{if } p = m-N+1 \quad \forall m \in (P+1, N-1) \\ 0 & \text{otherwise} \end{cases} \tag{A.35}$$

To ensure the transmitted energy of the shaped signal is identical to the flat spectrum signal, we solve for K. Where

$$E_{sym} = \frac{1}{N}\sum_{p=0}^{N-1}(KH_p)^2 \tag{A.36}$$

$$K = \sqrt{\frac{E_{sym}N}{\sum_{p=0}^{N-1}H_p^2}} \tag{A.37}$$

The shaped signal received after passing through the channel is represented by Figure A.5 and (A.38).

$$R_{shaped}[m] = \begin{cases} KH_m^2 e^{+j(\phi_p+\theta_k+\Theta_m)} & \text{if } p = m \quad \forall m \in (1, P-1) \\ KH_m^2 e^{-j(\phi_p+\theta_k+\Theta_m)} & \text{if } p = m-N+1 \quad \forall m \in (P+1, N-1) \\ 0 & \text{otherwise} \end{cases} \tag{A.38}$$

Therefore, it can be shown the energy in the received spectrally encoded, shaped spectrum TDCS signal γ_{shaped} is given by:

$$\gamma_{shaped} = \frac{1}{N}\sum_{k=0}^{N-1}(KH_m^2)^2 \tag{A.39}$$

$$= \frac{K^2}{N}\sum_{p=0}^{N-1}H_p^4 \tag{A.40}$$

$$= \frac{E_{sym}}{\sum_{p=0}^{N-1}H_p^2}\sum_{p=0}^{N-1}H_p^4 \tag{A.41}$$

Now the energy in the received signals can be compared:

$$\gamma_{flat} \overset{?}{>}_{<} \gamma_{shaped} \tag{A.42}$$

$$\frac{E_{sym}}{N-2}\sum_{\substack{p=0 \\ p\neq 0,P}}^{N-1}H_p^2 \overset{?}{>}_{<} \frac{E_{sym}}{\sum_{p=0}^{N-1}H_p^2}\sum_{p=0}^{N-1}H_p^4 \tag{A.43}$$

$$\frac{1}{N-2}\left(\sum_{p=0}^{N-1}H_p^2\right)^2 \overset{?}{>}_{<} \sum_{p=0}^{N-1}H_p^4 \tag{A.44}$$

The Chebyshev Sum inequality states that if $x_1 \geq x_2 \geq ... \geq x_n$ and $y_1 \geq y_2 \geq ... \geq y_n$ [14] then:

$$(x_1 + x_2 + ... + x_n)(y_1 + y_2 + ... + y_n) \leq n(x_1y_1 + x_2y_2 + ... + x_ny_n) \tag{A.45}$$

This inequality can easily be applied to the comparison of γ_{flat} and γ_{shaped} above in (A.44). Since addition is commutative, assume that the H_p are ordered from largest to smallest and set:

$$x_1 = y_1 = H_1^2 \geq x_2 = y_2 = H_2^2 \geq ... \geq x_{N-1} = y_{N-1} = H_{N-1}^2 \tag{A.46}$$

From here, (A.44) can be manipulated to match the form of (A.45) as shown below:

$$\begin{aligned}(H_1^2 + H_2^2 + ... + H_{N-1}^2)(H_1^2 + H_2^2 + ... + H_{N-1}^2) \leq \\ (N-2)(H_1^2H_1^2 + H_2^2H_2^2 + ... + H_{N-1}^2H_{N-1}^2)\end{aligned} \tag{A.47}$$

Therefore:

$$\gamma_{flat} \leq \gamma_{shaped} \qquad \square \tag{A.48}$$

A.3 Derivation of Complex Low-Pass Equivalent Representation of TDCS Signals

The purpose of the section is to derive the complex low-pass equivalent of the TDCS signal to enable analysis of the system through the multipath fading channel. Assume first, that the baseband signal is bandlimited such that $W_{BB} < 2Pf_{sb}$. Recall from (2.3) the expression for a baseband time-domain representation of the TDCS signal labelled $s_{BB}(t)$ here.

$$s_{BB}(t) = 2\sum_{p=0}^{P-1} A_p \cos(2\pi f_{sb}pt + \phi_p + \theta_k) \tag{A.49}$$

Assuming that a bandpass signal is generated by multiplying by a sinusoidal carrier, the bandpass representation $s_{BP}(t)$ is:

$$\begin{aligned} s_{BP}(t) &= s_{BB}(t)\cos(2\pi f_c t) && \text{(A.50)} \\ &= 2\sum_{p=0}^{P-1} A_p \cos\left(2\pi f_{sb} p t + \phi_p + \theta_k\right)\cos(2\pi f_c t) && \text{(A.51)} \end{aligned}$$

where f_c is the carrier frequency. Using the following property for a product of cosines:

$$\cos A \cos B = \frac{1}{2}\cos(A+B) + \frac{1}{2}\cos(A-B) \tag{A.52}$$

Equation (A.51) is converted into a sum of sums instead of sum of products.

$$s_{BP}(t) = \sum_{p=0}^{P-1} A_p \left[\cos\left(2\pi f_c t + 2\pi f_{sb} p t + \phi_p + \theta_k\right) + \cos\left(2\pi f_c t - [2\pi f_{sb} p t + \phi_p + \theta_k]\right)\right] \tag{A.53}$$

An analytical representation of the signal $s_+(t)$ has only positive frequency components and is formed using the following relationship [8, 149]:

$$s_+(t) = s_{BP}(t) + j\hat{s}_{BP}(t) \tag{A.54}$$

where $\hat{s}_{BP}(t)$ is the Hilbert transform of $s_{BP}(t)$. Since, the Hilbert transform of a cosine is the sine, the Hilbert transform of the bandpass signal $\hat{s}_{BP}(t)$ is:

$$\hat{s}_{BP}(t) = \sum_{p=0}^{P-1} A_p \left[\sin\left(2\pi f_c t + 2\pi f_{sb} p t + \phi_p + \theta_k\right) + \sin\left(2\pi f_c t - [2\pi f_{sb} p t + \phi_p + \theta_k]\right)\right] \tag{A.55}$$

Now the analytic representation of the signal $s_+(t)$ for the TDCS signal is formed.

$$s_+(t) = \sum_{p=0}^{P-1} A_p \left[\cos\left(2\pi f_c t + \Omega_{sb}\right) + \cos\left(2\pi f_c t - \Omega_{sb}\right) \right] + ... \\ j \sum_{p=0}^{P-1} A_p \left[\sin\left(2\pi f_c t + \Omega_{sb}\right) + \sin\left(2\pi f_c t - \Omega_{sb}\right) \right] \quad (A.56)$$

where

$$\Omega_{sb} = 2\pi f_{sb} p t + \phi_p + \theta_k \quad (A.57)$$

Rearranging terms to group like arguments of cosine and sine, the next step follows.

$$s_+(t) = \sum_{p=0}^{P-1} A_p \left[\cos\left(2\pi f_c t + \Omega_{sb}\right) + j \sin\left(2\pi f_c t + \Omega_{sb}\right) \right] + ... \\ \sum_{p=0}^{P-1} A_p \left[\cos\left(2\pi f_c t - \Omega_{sb}\right) + j \sin\left(2\pi f_c t - \Omega_{sb}\right) \right] \quad (A.58)$$

Now recall the relationship between a complex exponential and the sine and cosine of the same angle.

$$e^{j\phi} = cos\phi + j \sin\phi \quad (A.59)$$

Using this relationship, the analytic signal can be expressed as a two sums of complex exponentials.

$$s_+(t) = \sum_{p=0}^{P-1} A_p \exp\left[j(2\pi f_c t + \Omega_{sb}) \right] + \sum_{p=0}^{P-1} A_p \exp\left[j(2\pi f_c t - \Omega_{sb}) \right] \quad (A.60)$$

By factoring out the carrier the next step follows.

$$s_+(t) = \left[\sum_{p=0}^{P-1} A_p \exp\Big(j\Omega_{sb}\Big) + \sum_{p=0}^{P-1} A_p \exp\Big(-j\Omega_{sb}\Big)\right] \exp(j2\pi f_c t) \quad \text{(A.61)}$$

Now the relationship between the analytic signal and the complex low-pass equivalent signal $s_l(t)$ is shown.

$$s_l(t) = s_+(t)\exp(-j2\pi f_c t) \quad \text{(A.62)}$$

By multiplying the positive frequency only analytic signal by a negative complex exponential, the spectrum of the analytical signal is translated down to the baseband region of the spectrum. Therefore, (A.64) is the complex low-pass representation of the TDCS signal.

$$\begin{aligned} s_l(t) &= \left[\sum_{p=0}^{P-1} A_p \exp\Big(j\Omega_{sb}\Big) + \sum_{p=0}^{P-1} A_p \exp\Big(-j\Omega_{sb}\Big)\right] \cdot \\ &\qquad \exp(j2\pi f_c t)\exp(-j2\pi f_c t) \quad \text{(A.63)} \\ &= \sum_{p=0}^{P-1} A_p \exp\Big(j\Omega_{sb}\Big) + \sum_{p=0}^{P-1} A_p \exp\Big(-j\Omega_{sb}\Big) \quad \text{(A.64)} \end{aligned}$$

The last step in the derivation requires two additional assumptions. First, assume that the spectrum can be asymmetric, therefore the A_p on the positive and negative sides of the spectrum are allowed to become unequal. Now the two summations in (A.64) can be rewritten as:

$$s_l(t) = \sum_{\substack{p=-P+1 \\ p\neq 0}}^{P-1} A_p \exp\Big(j\Omega_{sb}\Big) + 2A_0 \quad \text{(A.65)}$$

The second assumption is based on the earlier bandwidth constraint on the baseband signal, i.e. $W_{BB} < 2Pf_{sb}$. For convenience, rather than carrying the $2A_0$ term in the summation, recall that the discrete version of the signal has $N = 2P$ frequency components, and that the $P = \frac{1}{2}N$ term is the Nyquist term which aliases to the DC term. Therefore, to simplify the expression, the 2nd A_0 is carried at the Nyquist frequency $2\pi f_{sb}P = -2\pi f_{sb}P$ therefore the final expression for the complex lowpass signal TDCS signal is given by (A.67)

$$s_l(t) = \sum_{p=-P}^{P-1} A_p \exp\Big(j\Omega_{sb}\Big) \tag{A.66}$$

$$s_l(t) = \sum_{p=-P}^{P-1} A_p \exp\Big[j(2\pi f_{sb}pt + \phi_p + \theta_k)\Big] \qquad 0 \le t \le T_{sb} \tag{A.67}$$

It is easily seen that by using the following relationship

$$\cos\phi = \frac{1}{2}\left[e^{j\phi} + e^{-j\phi}\right] \tag{A.68}$$

that the complex low-pass representation in (A.67) is equivalent to the original representation in (A.49). However, note that the spectral magnitudes (A_p) are independent, therefore the potential to form complex valued signals is enabled.

A.4 Energy in a Continuous-Time TDCS Complex, Low-Pass Equivalent Signal

The derivation begins by converting the time-domain complex lowpass representation in (A.67) into a frequency-domain representation using the identity:

$$\mathcal{F}\left[\exp(j2\pi kt) \quad \forall \quad 0 \le t \le T_{sb}\right] = \operatorname{sinc}\left[T_{sb}(f - kf_{sb})\right] \tag{A.69}$$

where $\mathcal{F}[\cdot]$ denotes the Fourier transform. Now the frequency domain representation of the complex lowpass TDCS signal $S_l(f)$ is:

$$S_l(f) = \sum_{p=-P}^{P-1} A_p \Big\{ \text{sinc}\big[T_{sb}(f - pf_{sb})\big] e^{j\text{sgn}(p)(\phi_p + \theta_k)} \Big\} \tag{A.70}$$

where:

$$\text{sgn}(p) = \begin{cases} 1 & \forall p > 0 \\ 0 & p = 0 \\ -1 & \forall p < 0 \end{cases} \tag{A.71}$$

Applying the continuous-frequency definition of energy from (3.7), the expression for the energy in the complex lowpass equivalent signal follows.

$$\begin{aligned}
E_b &= \int_{-\infty}^{\infty} |S_l(f)|^2 dt && \text{(A.72)} \\
&= \int_{-\infty}^{\infty} S(f) S^*(f) dt && \text{(A.73)} \\
&= \int_{-\infty}^{\infty} \left(\sum_{p=-P}^{P-1} A_p \Big\{ \text{sinc}\big[T_{sb}(f - pf_{sb})\big] e^{j\text{sgn}(p)(\phi_p + \theta_k)} \Big\} \right) \cdot \\
&\qquad \left(\sum_{p=-P}^{P-1} A_p \Big\{ \text{sinc}\big[T_{sb}(f - pf_{sb})\big] e^{-j\text{sgn}(p)(\phi_p + \theta_k)} \Big\} \right) dt && \text{(A.74)} \\
&= \int_{-\infty}^{\infty} \sum_{p=-P}^{P-1} A_p^2 \Big\{ \text{sinc}^2\big[T_{sb}(f - pf_{sb})\big] \Big\} dt && \text{(A.75)} \\
&= \sum_{p=-P}^{P-1} A_p^2 \int_{-\infty}^{\infty} \Big\{ \text{sinc}^2\big[T_{sb}(f - pf_{sb})\big] \Big\} dt && \text{(A.76)} \\
& && \text{(A.77)}
\end{aligned}$$

Using the following identity,

$$\int_{-\infty}^{\infty} \text{sinc}^2(f - \phi)\, dt = 1 \tag{A.78}$$

by a change of variable, it is easily shown that

$$\int_{-\infty}^{\infty} \mathrm{sinc}^2\Big[T_{sb}(f-\phi)\Big]\,dt \;=\; T_{sb} \tag{A.79}$$

Therefore, the energy expression simplifies quickly to

$$E_b \;=\; T_{sb}\sum_{p=-P}^{P-1} A_p^2 \tag{A.80}$$

$$\tag{A.81}$$

A.5 Simplification of Triple Sum Over Exponential

Beginning with the triple summation of the exponential from (A.82), the relationship between positive and negative exponentials and cosine from (A.68) is applied.

$$\sum_{\substack{p=-P+1\\p\neq 0}}^{P-1}\sum_{n=1}^{L}\sum_{\substack{m=1\\m\neq n}}^{L} e^{\frac{jp\pi}{P}(m-n)} \;=\; \sum_{p=1}^{P-1}\sum_{n=1}^{L}\sum_{\substack{m=1\\m\neq n}}^{L} 2\cos\Big[\frac{p\pi}{P}(m-n)\Big] \tag{A.82}$$

First, the interior double summation over m and n is simplified. The relationship in (A.83) is proved inductively.

$$\sum_{n=1}^{L}\sum_{\substack{m=1\\m\neq n}}^{L} 2\cos\Big[\frac{p\pi}{P}(m-n)\Big] \;=\; \sum_{k=1}^{L-1} 4(L-k)\cos\left(\frac{kp\pi}{P}\right) \quad \forall \quad L\geq 2 \tag{A.83}$$

The equations below show that the relationship is true for $L=2$.

$$\sum_{n=1}^{2}\sum_{\substack{m=1\\m\neq n}}^{2} 2\cos\left[\phi(m-n)\right] \;=\; \sum_{k=1}^{1} 4(2-k)\cos(\phi) \tag{A.84}$$

$$2\cos(-\phi)+2\cos\phi \;=\; 4(2-1)\cos 1\phi \tag{A.85}$$

$$4\cos\phi \;=\; 4\cos\phi \tag{A.86}$$

Assuming the relationship holds for L, the next step is to prove it holds for $L+1$. Calculating the left side of the equation first for $L+1$:

$$\sum_{n=1}^{L+1}\sum_{\substack{m=1\\m\neq n}}^{L+1} 2\cos(\phi[m-n]) \;=\; \sum_{n=1}^{L}\sum_{\substack{m=1\\m\neq n}}^{L} 2\cos(\phi[m-n]) + ...$$

for $n = 1..L,\ m = L+1$:

$$2\cos(L\phi) + 2\cos[(L-1)\phi] + ... + 2\cos\phi + ...$$

for $n = 1..L+1, \neq L,\ m = L$:

$$\begin{aligned} &2\cos[(L-1)\phi] + 2cos[(L-2)\phi]... + 2\cos\phi + 2\cos(-\phi) + ... \\ &\vdots \end{aligned}$$

for $n = L,\ m = 1..L+1 \neq L$:

$$2\cos[(-L+1)\phi] + 2\cos[(-L+2)\phi] + ... + 2\cos(-\phi) + 2\cos(\phi)$$

for $n = L+1,\ m = 1..L$:

$$2\cos(-L\phi) + 2\cos[(-L+1)\phi] + ... + 2\cos(-\phi) \tag{A.87}$$

Now consolidating like terms:

$$\begin{aligned} = \;& \sum_{n=1}^{L}\sum_{\substack{m=1\\m\neq n}}^{L} \cos(\phi[m-n]) + ... \\ & 4\cos(L\phi) + 4(2)\cos((L-1)\phi) + ... + 4(L)\cos(\phi) \end{aligned} \tag{A.88}$$

Now the right side for $L+1$:

$$\sum_{k=1}^{L} 4(L+1-k)\cos(k\phi) =$$

$$= \sum_{k=1}^{L-1} 4(L-k)\cos(k\phi) + ...$$

$$4(L)\cos 1\phi + 4(L-1)\cos(2\phi) + ... + 4(1)\cos(L\phi) \qquad \text{(A.89)}$$

Since (A.88) is identical to (A.89) using the assumption that the identity is true for L, the relationship has been proven inductively for all L.

This relationship is now applied to the original triple summation.

$$\sum_{\substack{p=-P+1 \\ p\neq 0}}^{P-1} \sum_{n=1}^{L} \sum_{\substack{m=1 \\ m\neq n}}^{L} e^{\frac{jp\pi}{P}(m-n)} = \sum_{p=1}^{P-1}\sum_{k=1}^{L-1} 4(L-k)\cos(\frac{kp\pi}{P}) \qquad \text{(A.90)}$$

$$= \sum_{k=1}^{L-1} 4(L-k)\sum_{p=1}^{P-1}\cos(\frac{kp\pi}{P}) \qquad \text{(A.91)}$$

Now the simplification of the sum of the cosine term over p is examined. Noting that p, k, P are integers, the cosine term can also be expressed as:

$$\sum_{p=1}^{P-1}\cos\left(\frac{kp\pi}{P}\right) = \sum_{p=1}^{P-1}\cos\left(k\pi\frac{p}{P}\right) \qquad \text{(A.92)}$$

The sum is now considered in two cases: k even and k odd. In the first case, if k is even, then the summation over p covers nearly an integer number of full cycles of the cosine. It can be shown that for a P length sequence of a cosine with a frequency that is an integer multiple of 2π that: [5, 132]

$$\sum_{p=0}^{P-1}\cos\left(k\pi\frac{p}{P}\right) = 0, \quad \forall \quad k \in \text{even}, \quad k, P \in \text{Integer} \qquad \text{(A.93)}$$

Returning to the sum of interest, (A.92) can be rewritten as

$$\cos(k\pi(0)) + \sum_{p=1}^{P-1} \cos\left(k\pi\frac{p}{P}\right) = 0, \forall \quad k \in \text{ even} \tag{A.94}$$

$$1 + \sum_{p=1}^{P-1} \cos(k\pi\frac{p}{P}) = 0 \tag{A.95}$$

$$\sum_{p=1}^{P-1} \cos(k\pi\frac{p}{P}) = -1 \quad \forall k \in \text{even} \tag{A.96}$$

Therefore, for even k, each sum over p for the cosine terms is -1.

For k odd, it can be shown that given the same restrictions on p, k, and P:

$$\sum_{p=0}^{P-1} \cos\left[k\pi\left(\frac{p}{P}\right)\right] = 1, \forall \quad k \in \text{odd}, \quad k, P \in \text{Integer} \tag{A.97}$$

Using the same progression as above, the sum over p from (1,P-1) for the k odd terms is 0.

Therefore, the summation over the cosine term can be simplified to -1 for all k that are even integers and the summation is 0 for all k that are odd integers. Now, (A.91) can now be simplified in two cases, L even, and L odd:

I: L Even. When L is even, (A.91) can be written:

$$\sum_{\substack{k=2 \\ \text{even}}}^{L-2} -4(L-k) = -4[L-2+L-4+...+4+2] \tag{A.98}$$

$$= -4\left(\frac{L-2}{4}\right)L \tag{A.99}$$

$$= -L(L-2) \tag{A.100}$$

It can be seen that the bracketed sum contains $(L-2)/2$ terms, which when paired sum to L. Therefore the bracketed sum is equivalent to $(L-2)/4$ terms of L.

II: L Odd. When L is odd, (A.91) can be written:

$$\sum_{\substack{k=2 \\ \text{even}}}^{L-1} -4(L-k) = -4[L-2+L-4+...+3+1] \quad (A.101)$$

$$= -4\left(\frac{L-1}{4}\right)(L-1) \quad (A.102)$$

$$= -(L-1)^2 \quad (A.103)$$

It can be seen that the bracketed sum contains $(L-1)/2$ terms, which when paired sum to $L-1$. Therefore the bracketed sum is equivalent to $(L-1)/4$ terms of $L-1$.

In summary, the triple summation from (A.82) is equivalent to the following expression:

$$\sum_{\substack{p=-P+1 \\ p\neq 0}}^{P-1} \sum_{n=1}^{L} \sum_{\substack{m=1 \\ m\neq n}}^{L} e^{\frac{jp\pi}{P}(m-n)} = \begin{cases} -L(L-1) & L \in \text{even} \\ -(L-1)^2 & L \in \text{odd} \end{cases} \quad (A.104)$$

A.6 Distribution of V_2

In (2.16), it was shown that each α is a Rayleigh distributed random variable with parameter σ. Since α_n and α_m are independent and identically distributed, it can be shown that the individual and joint densities are as listed in Equations A.105 A.106, and A.107.

$$f_{\alpha_n}(\alpha_n) = \frac{\alpha_n}{\sigma^2} e^{-\alpha_n^2/2\sigma^2} \quad (A.105)$$

$$f_{\alpha_m}(\alpha_m) = \frac{\alpha_m}{\sigma^2} e^{-\alpha_m^2/2\sigma^2} \quad (A.106)$$

$$f_{\alpha_n,\alpha_m}(\alpha_n,\alpha_m) = f_{\alpha_n}(\alpha_n) \cdot f_{\alpha_m}(\alpha_m) = \frac{\alpha_n \alpha_m}{\sigma^4} exp\left\{\frac{-1}{2\sigma^2}(\alpha_n^2+\alpha_m^2)\right\} \quad (A.107)$$

The relationship in (A.109) shows the transformation to determine the distribution of a product of two random variables [7, 205].

$$z = xy \quad (A.108)$$

$$f_z(z) = \int_{-\infty}^{\infty} \frac{1}{|w|} f_{xy}(w, \frac{z}{w})\, dw \quad (A.109)$$

Now applying the definition of $f_{x,y}$ from (A.109), the distribution of the product $\alpha_n\alpha_m$ can be determined as shown below.

$$
\begin{aligned}
z &= \alpha_n\alpha_m && \text{(A.110)}\\
f_z(z) &= \int_{-\infty}^{\infty} \frac{1}{|w|}\left[\frac{w}{\sigma^2}e^{-w^2/2\sigma^2}\right]\left[\frac{z}{w\sigma^2}e^{-z^2/w^2 2\sigma^2}\right] dw && \text{(A.111)}\\
&= \int_{-\infty}^{\infty} \frac{z}{\sigma^4|w|}\exp\left\{w^2+\left(\frac{z}{w}\right)^2\right\} dw && \text{(A.112)}
\end{aligned}
$$

Application of the scaling relationship for random variables yields the following expression for the distribution of V_2 [7, 131].

$$
\begin{aligned}
V_2 &= Az \qquad \text{where:} && \text{(A.113)}\\
A &= -E_{sym}\left(\frac{L(L-2)}{N-2}\right) && \text{(A.114)}\\
f_{V_2}(V_2) &= \frac{1}{|A|}f_z\left(\frac{V_2}{A}\right) && \text{(A.115)}\\
&= \int_{-\infty}^{\infty} \frac{1}{|A||w|\sigma^4}\exp\left\{w^2+\left(\frac{V_2}{Aw}\right)^2\right\} dw && \text{(A.116)}
\end{aligned}
$$

A.7 Derivation of the Distributions of H_p^2 and H_p^4

In (2.34) it was shown that the density of H_p^2 is a scaled Chi-square random variable with two degrees of freedom (DOF). The transformation in (A.117) is used to determine the distribution of the fourth power of H_p [7, 132].

$$
\begin{aligned}
\text{if} \quad y &= ax^2 \qquad \text{then given } f_x(x), && \text{(A.117)}\\
f_y(y) &= \frac{1}{2a\sqrt{y/a}}\left[f_x\left(\sqrt{\frac{y}{a}}\right)+f_x\left(-\sqrt{\frac{y}{a}}\right)\right] && \text{(A.118)}
\end{aligned}
$$

Substituting the distribution for H_p^2 from (2.34) into (A.117), the derivation of the distribution of H_p^4 is shown below.

$$y = H_p^4 = x^2 = (H_p^2)^2 \tag{A.119}$$

$$f_x(x) = f_{H_p^2}(H_p^2) = \frac{e^{-H_p^2/2L\sigma^2}}{2L\sigma^2} \tag{A.120}$$

$$f_y(y) = f_{H_p^4}(H_p^4) = \frac{1}{2\sqrt{H_p^4}}\left[f_{H_p^2}\left(\sqrt{H_p^4}\right) + f_{H_p^2}\left(-\sqrt{H_p^4}\right)\right] \tag{A.121}$$

$$\tag{A.122}$$

Since $f_{H_p^2}(H_p^2)$ is valid only for $H_p^2 \geq 0$, the distribution for H_p^4 can be simplified to (A.123).

$$f_{H_p^4}(H_p^4) = \frac{1}{2\sqrt{H_p^4}}\left[\frac{e^{-\sqrt{H_p^4}/2L\sigma^2}}{2L\sigma^2}\right] \tag{A.123}$$

Note that (A.123) is described by a Weibull distribution with parameters $\alpha = \beta = 1/2$ [7, 89].

A.8 Confidence Intervals on a Sample Mean

To compute the confidence interval on the mean of a Monte Carlo simulation, the simulation is structured into I replications each with n samples. The following equations are referenced from [3, 431]. Begin by computing the mean for each replication.

$$\bar{x}_i = \frac{1}{n}\sum_{j=1}^{n} x_{i,j}, \qquad i = 1, 2, ..., I \tag{A.124}$$

Next, compute the grand mean ($\bar{\bar{x}}$).

$$\bar{\bar{x}} = \frac{1}{I}\sum_{i=1}^{I} \bar{x}_i \tag{A.125}$$

The grand mean is then used to compute the variance on the replication means.

$$\mathrm{Var}(\bar{x}) = \frac{1}{I-1}\sum_{i=1}^{I}(\bar{x}_i - \bar{\bar{x}})^2 \tag{A.126}$$

The grand mean and $\mathrm{Var}(\bar{x})$ are then used to compute the confidence interval on the mean of the Monte Carlo simulation.

$$\bar{\bar{x}} \pm z_{1-\alpha/2}\mathrm{Var}(\bar{x}) \tag{A.127}$$

where $z_{1-\alpha/2}$ is the $1-\alpha/2$ quantile of the standard Normal distribution.

A.9 Methodology for Estimating Distributions Using Quantile-Quantile Plots and Linear Regression Modeling

A quantile maps a given probability to the inverse cumulative distribution function CDF of that probability for a given distribution. For example, since the 50^{th} quantile of the standard Normal distribution is 0, the CDF of 0 is 0.50 indicating that 50% of samples from the standard Normal distribution curve are less than 0. The quantiles for n-points of measured data are computed by first ordering the measured data, y_i, from smallest to largest. Then the quantile associated with the y_i is q_i, and computed using (A.128) [3, 199].

$$q_i = \frac{i-0.5}{n} \qquad i = 1, 2, ..., n \tag{A.128}$$

Equation (A.129) shows the quantiles for the distribution being tested, x_i, are simply the inverse CDF of q_i [3, 198].

$$x_i = F^{-1}(q_i) \qquad i = 1, 2, ..., n \tag{A.129}$$

To plot the data, the q_i^{th} quantile for the distribution being tested is plotted on the x-axis against the matching q_i^{th} quantile of the measured data on the y-axis.

Once the quantile-quantile plot is completed, the linear regression model between the x_i and y_i can be computed. If the linear estimate of the measured data quantiles is $\hat{y}_i$, (A.130) shows the relationship between x_i and the estimate.

$$\hat{y}_i = b_0 + b_1 x_i \tag{A.130}$$

The parameters of the linear regression model are given by Equations A.131 and A.132 [3, 223].

$$b_1 = \frac{\sum_{i=1}^{n} x_i y_i - n\bar{x}\bar{y}}{\sum_{i=1}^{n} x_i^2 - n(\bar{x})^2} \tag{A.131}$$

$$b_0 = \bar{y} - b_1 \bar{x} \tag{A.132}$$

where

$$\bar{x} = \frac{1}{n}\sum_{i=1}^{n} x_i \tag{A.133}$$

$$\bar{y} = \frac{1}{n}\sum_{i=1}^{n} y_i \tag{A.134}$$

Once the linear regression model is computed, the quality of the model is evaluated using analysis of variation techniques. Specifically, the coefficient of determination R^2 evaluates the fit of the regression models against the actual data in the quantile-quantile plot. In short, the coefficient of determination is a measure of how much variation is explained by the model. A perfect model has an R^2 equal to 1 [3, 227]. Since identically distributed data yields a perfectly linear quantile-quantile plot, the linear regression model should fit the quantile-quantile plot of a perfectly matched distribution with an R^2 of 1. Data that is not distributed identically yields a non-linear quantile-quantile plot and the linear regression model imperfectly fits the data, yielding an R^2 of less than 1. The coefficient of determination is computed using (A.135) [3, 227].

$$R^2 = \frac{\text{SST} - \text{SSE}}{\text{SST}} \tag{A.135}$$

where

$$\text{SST} = \left(\sum_{i=1}^{n} y_i^2\right) - n\bar{y}^2 \tag{A.136}$$

$$\text{SSE} = \sum_{i=1}^{n} (y_i - \hat{y}_i)^2 \tag{A.137}$$

A.10 Interferer Spectral Amplitudes

Cited from [6, 4-4], the spectral amplitudes of the narrow band jammer are:

Table A.1: Table of Narrow Band Interferer Spectral Magnitudes

Index	1	2	3	4	5	6
Magnitude	0.0000	0.3034	0.4142	0.6362	1.0888	2.0215
Index	7	8	9	10	11	12
Magnitude	3.4755	3.8799	3.6811	2.9683	1.9194	1.2279
Index	13	14	15	16	17	18
Magnitude	0.8696	0.6794	0.5667	0.4928	0.4406	0.4017
Index	19	20	21	22	23	24
Magnitude	0.3716	0.3477	0.3284	0.3125	0.2994	0.2884
Index	25	26	27	28	29	30
Magnitude	0.2793	0.2718	0.2656	0.2605	0.2566	0.2535
Index	31	32	33	34	35	36
Magnitude	0.2514	0.2502	0.0000	0.2502	0.2514	0.2535
Index	37	38	39	40	41	42
Magnitude	0.2566	0.2605	0.2656	0.2718	0.2793	0.2884
Index	43	44	45	46	47	48
Magnitude	0.2994	0.3125	0.3284	0.3477	0.3716	0.4017
Index	49	50	51	52	53	54
Magnitude	0.4406	0.4928	0.5667	0.6794	0.8696	1.2279
Index	55	56	57	58	59	60
Magnitude	1.9194	2.9683	3.6811	3.8799	3.4755	2.0215
Index	61	62	63	64		
Magnitude	1.0888	0.6362	0.4142	0.3034		

Bibliography

1. Department of the Army. "Combined Arms Operations in Urban Terrain". *US Army Field Manual 3-06.11*. Headquarters, Department of the Army, HQ USA, Washington, 28 Febrary 2002.

2. Giles, Lionel M.A. "SUN TZU ON THE ART OF WAR, THE OLDEST MILITARY TREATISE IN THE WORLD, Translated from the Chinese. (1910)". http://www.au.af.mil/au/awc/awcgate/artofwar.htm, Accessed Online, 8 September 04 2005.

3. Jain, Raj. *The Art of Computer Systems Performance Analysis, Techniques for Experimental Design, Measurement, Simulation, and Modeling*. John Wiley and Sons, Inc., New York, New York, 1991.

4. McKinstry, David R. and R. Michael Buehrer. "Issues in the performance and covertness of UWB communications systems". *The 2002 45th Midwest Symposium on Circuits and Systems, 2002. MWSCAS-2002.*, volume 3, 601–4. 4-7 August.

5. Mitra, Sanjit K. *Digital Signal Processing, A Computer-Based Approach, Second Edition*. McGraw-Hill Irwin, New York, New York, 10020, 2001.

6. Nunez, Abel. *Interference Suppression in Multiple Access Communications Using M-ary Phase Shift Keying Generated Using Spectral Encoding*. Master's thesis, Graduate School of Engineering, Air Force Institute of Technology (AETC), Wright-Patterson AFB OH, March 2004. AFIT/GE/ENG/04-20.

7. Papoulis, Athanasios and S. Unnikrishna Pillai. *Probability, Random Variables, and Stochastic Processes, Fourth Edition*. Mc Graw Hill, New York, New York, 2002.

8. Proakis, John G. *Digital Communications, Fourth Edition*. Mc Graw Hill, New York, New York, 2001.

9. Radcliffe, Rodney. *Design and Simulation of a Transform Domain Communication System*. Master's thesis, Graduate School of Engineering, Air Force Institute of Technology (AETC), Wright-Patterson AFB OH, December 1996. AFIT/GE/ENG/96D-16.

10. Rappaport, Theodore S. *Wireless Communications, Principles and Practice*. Prentice Hall PTR, Upper Saddle River, New Jersey 07458, 1996.

11. Roberts, Marcus L. *Synchronization of a Transform Domain Communication System*. Master's thesis, Graduate School of Engineering, Air Force Institute of Technology (AETC), Wright-Patterson AFB OH, March 2000. AFIT/GE/ENG/00M-15.

12. Sklar, Bernard. *Digital Communications, Fundamentals and Applications, Second Edition*. Prentice Hall PTR, Upper Saddle River, New Jersey 07458, 2001.

13. Swackhammer, Patrick J. *Design and Simulation of a Multiple Access Transform Domain Communication System.* Master's thesis, Graduate School of Engineering, Air Force Institute of Technology (AETC), Wright-Patterson AFB OH, March 1999. AFIT/GE/ENG/99M-28.

14. Weisstein, Eric W. "Chebyshev Sum Inequality". From MathWorld–A Wolfram Web Resource. http://mathworld.wolfram.com/ChebyshevSumInequality.html, Accessed Online, February 05 2005.

15. Weisstein, Eric W. "Delta Function". From MathWorld–A Wolfram Web Resource. http://mathworld.wolfram.com/DeltaFunction.html, Accessed Online, February 05 2005.

REPORT DOCUMENTATION PAGE

Form Approved
OMB No. 0704-0188

PLEASE DO NOT RETURN YOUR FORM TO THE ABOVE ORGANIZATION.

1. REPORT DATE *(DD-MM-YYYY)*	2. REPORT TYPE	3. DATES COVERED *(From - To)*
21-03-2005	Master's Thesis	Sep 2004 - Mar 2005

4. TITLE AND SUBTITLE

PERFORMANCE OF A SPECTRALLY ENCODED MULTI-CARRIER PHASE SHIFT KEYING COMMUNICATIONS SYSTEM IN A FREQUENCY-SELECTIVE, SLOWLY-FADING MULTIPATH CHANNEL

5a. CONTRACT NUMBER

5b. GRANT NUMBER

5c. PROGRAM ELEMENT NUMBER

6. AUTHOR(S)

Gaona, Charles M., Major, USAF

5d. PROJECT NUMBER

5e. TASK NUMBER

5f. WORK UNIT NUMBER

7. PERFORMING ORGANIZATION NAME(S) AND ADDRESS(ES)

Air Force Institute of Technology
Graduate School of Engineering and Management (AFIT/EN)
2950 Hobson Way, Wright-Patterson AFB OH 45433-7765

8. PERFORMING ORGANIZATION REPORT NUMBER

AFIT/GE/ENG/05-03

9. SPONSORING/MONITORING AGENCY NAME(S) AND ADDRESS(ES)

James P. Stephens, Sr.,
AFRL/SNRW Bldg 620
2241 Avionics Circle Room N3-F10
Wright-Patterson AFB, OH 45433-7333 Comm(937) 255-5579, DSN 785-5579

10. SPONSOR/MONITOR'S ACRONYM(S)

11. SPONSOR/MONITOR'S REPORT NUMBER(S)

12. DISTRIBUTION/AVAILABILITY STATEMENT

APPROVED FOR PUBLIC RELEASE; DISTRIBUTION UNLIMITED.

13. SUPPLEMENTARY NOTES

14. ABSTRACT This research examines the performance of a spectrally encoded, multi-carrier, phase shift keying communications system in a frequency-selective, slowly-fading multipath channel. The specific communications system modeled is the transform domain communication system (TDCS) originally researched as an interference avoidance technique. Previous TDCS research assumed an additive white gaussian noise channel, which is not representative of a realistic environment. This thesis presents overviews of previous TDCS research, the multipath fading channel, and the RAKE receiver. Analysis and Matlab simulations compare the performance of spectrally encoded and un-encoded signals through a multipath fading channel using an L-diversity TDCS RAKE receiver. Encoded signals take on the spectral shape of the multipath fading channel transfer function. Un-encoded signals have a flat magnitude spectrum. The research also evaluates the interference rejection capability of spectrally encoded signals in a multipath channel. Research results indicate for diversities ranging between 2 and 50, spectrally encoded signals need 1.0 to 2.75dB less transmitted normalized bit energy to noise power spectral density ratios to achieve the same probability of bit error as un-encoded signals. Results also demonstrate that spectrally encoded TDCS signals retain the interference rejection capability.

15. SUBJECT TERMS

MULTIPATH TRANSMISSION, MULTICHANNEL COMMUNICATIONS, SPECTRAL ENERGY DISTRIBUTION, PHASE MODULATION, RADIOFREQUENCY INTERFERENCE, SUPPRESSION, SPREAD SPECTRUM

16. SECURITY CLASSIFICATION OF:			17. LIMITATION OF ABSTRACT	18. NUMBER OF PAGES	19a. NAME OF RESPONSIBLE PERSON
a. REPORT	b. ABSTRACT	c. THIS PAGE			Robert F. Mills, PhD
U	U	U	UU	148	19b. TELEPHONE NUMBER *(Include area code)* 937-255-3636x4527; email: robert.mills@afit.edu

Reset

Standard Form 298 (Rev. 8/98)
Prescribed by ANSI Std. Z39.18